

CHAPTER 5

THE EXPERIMENTAL VERIFICATION

INTRODUCTION

In Chapter 5 the distributed parameters model is validated applying it to the study of current distribution in different experimental situations. In Section 5.1 the simple case of current distribution in a 2-strand cable is analysed, studying current distribution in the presence of ramps or cycles of the external field applied to a loop formed between the two cable strands. The influence of different choices of the boundary conditions on the final results is shown.

In Section 5.2 an extensive measurement of the magnetic field in the bore of a short LHC dipole magnet is presented and analysed. A very similar behaviour is found between the amplitude of the modulation of the magnetic field along the magnet axis and the amplitude of supercurrents in the much simpler situation found in the two strand cable reported in Section 5.1. Moreover, the dependence of the amplitude of the magnetic field oscillations on the parameters of the current cycle is found to be qualitatively identical to that shown by the average value of the field. This correlation confirms the present understanding of the interaction between current distribution, filament magnetization and field decay in superconducting accelerator magnets.

The current distribution in the Rutherford cable of the magnet is finally simulated by means of the distributed parameters model. The use of appropriate meshing strategies leads to a very high reduction of the number of unknowns of the problem, up to a factor of about 60-70 with respect to the lumped parameters network model, when equivalent superstrands are considered.

A qualitative agreement between the behaviour of the calculated current distribution in the magnet cable and the amplitude of the measured field oscillations in the magnet bore has been found.

5.1 THE 2-STRAND CABLE EXPERIMENT

The experiment described in Section 2.4.1 and in detail in [12] was aimed to an experimental verification of the theory of “supercurrents”. The strand diameter of the NbTi/Cu multifilamentary conductor is equal to 0.3 mm, the cabling pitch and the transverse conductance are respectively equal to 10 mm and $0.5 \cdot 10^8 \Omega^{-1} \text{m}^{-1}$. Current loops are induced by an external field in a test loop in the middle of the cable, when no transport current is present.

We have applied the electromagnetic model described in Chapter 3 to the evaluation of the amplitude of the supercurrents in the presence of field ramps. We have calculated magnetic parameters as explained in Appendix B with reference to a cable pitch length sector and helicoidal trajectories of the strand axis.

In our model the parameter L_I reported by Krempasky and Schmidt is equivalent to $l_{11}+l_{22}-2l_{12}$. In order to take into account the mutual induction coupling of strand sectors which are in different coil layers, the distance/radius ratio of the two strands is used as a fitting parameter. In our model this corresponds to an arbitrary variation of the mutual inductance l_{12} , while l_{11} and l_{22} are nearly constant.

A value of d/r equal to 3.1, with $g_{12} = 0.52 \cdot 10^8 \Omega^{-1}m^{-1}$ has been taken. In this case we obtain $l_{11} = l_{22} = 8.36 \cdot 10^{-7}$ H/m, $l_{12} = 5.57 \cdot 10^{-7}$ H/m and $L_I = 5.58 \cdot 10^{-7}$ H/m.

Following our calculations the inductance of the test loop is not large enough to explain the difference of this ratio from the cabling theoretical one ($d/r=2$, with which we obtain $l_{11} = l_{22} = 8.33 \cdot 10^{-7}$ H/m, $l_{12} = 6.44 \cdot 10^{-7}$ H/m, $L_I=3.78 \cdot 10^{-7}$ H/m).

The additional contribution to the effective inductance L_I should be due to geometric imperfections increasing this distance and to the inductance of the coil formed by the two strands. We have evaluated the influence of this last term by means of a calculation of magnetic parameters made taking into account the coil geometry, which gives for L_I the value of $3.94 \cdot 10^{-7}$ H/m.

In Fig. 5.1 we report the comparison between the experimental and numerical results, during a magnetic field ramp, with reference to the current in the middle of the cable. A good agreement is obtained.

The numerical results reported in Fig. 5.1 were obtained by imposing the boundary conditions (3.16), with strand currents equal to zero at the cable ends. This condition reproduces exactly the experimental conditions. In fact the cable ends were cut before the experiments impeding the current circulation between the two strands at the cable ends.

Figure 5.2 reports a comparison with the results obtained if the equipotential condition (cable ends in short circuit) is used. The two solutions coincide till current diffusion reaches the end surfaces of the cable, then significantly differ because, in the equipotential surface case, a supercurrent loop is formed and current can flow continuously from one strand to the other through the end surfaces.

Figure 5.3 reports a comparison between the experimental results and the numerical results obtained when exciting the cable with a different field cycle, made of a ramp up, a flat top with constant current, and a ramp down. The agreement with experimental results is satisfactory.

CONCLUSIONS

A current distribution imbalance in multistrand superconducting cables can decrease the cable performances in transient conditions, with a remarkable limitation of the maximum current carried by the cable. Moreover, a non uniform current distribution can affect the field quality in accelerator magnets. A correct modeling of these phenomena can be useful for their understanding, for the improvement of the cable design, and for the compensation of their effects.

An electromagnetic model for the analysis of current distribution in multistrand superconducting cables has been developed.

The model is suitable for the analysis of large systems and is flexible enough to be applied to different geometric configurations of multistrand cables. This can be achieved by means of an appropriate evaluation of the model parameters.

The model is based on a set of partial differential equations, which makes it suitable for the coupling to a thermal-hydraulic description of the refrigerating system.

This work starts from the theoretical and experimental results on current distribution obtained by several researchers. In particular, the model extends the theory of “supercurrents” developed by Kremasky and Schmidt [10] for a 2-strand model to a more complete study of the time dependent coupling currents in a generic N strand cable. Another basic fundament of the work are the network models for current distribution in flat Rutherford cables developed by Akhmetov and Verweij [19-27]. This approach overcomes the main limitation of network models for the application to long cables, which is the very large number of unknowns.

This has been demonstrated comparing the two models in the evaluation of long range coupling currents, and obtaining a good quantitative agreement with a very remarkable reduction of the number of unknowns, ranging from ratios of ten to one hundred in different situations.

The model also overcomes the strong dependence on cable configuration implicit in network models. In order to show this we have compared it with a lumped parameters network model of cable in conduit conductors, obtaining a good agreement in the study of current redistribution after quench of one strand in a short triplex cable.

An important advantage of this formulation is the possibility to determine the analytical solution of the model equations in particular conditions of symmetry of the electrical parameters of the cable. A very good agreement has been obtained between the numerical and analytical solutions.

A validation of the model has been also performed against experimental results on the development of long range “supercurrents” in a two-strand cable, obtaining a good quantitative agreement.

Moreover, an extensive measurement of the magnetic field periodic modulation along the length of a LHC dipole has been presented and analysed. It has been shown that the amplitude of the modulation is strongly dependent

on the powering history of the magnet and that the features of this dependence are very similar to those found in a 2 strand cable in a much simpler situation. The scaling of the amplitude of the field modulation with powering history is essentially the same as the decay observed on average harmonics. This result confirms the idea that current distribution and field decay are intimately correlated.

The possibility to apply the distributed parameters model to the study of a real long cable has been finally demonstrated, obtaining a good qualitative agreement with the experimental data on the measured periodic pattern.

A deeper insight in help understanding its and the correct meaning

The superconducting having a circular cross section geometry of each strand is

consider a segment of cable of length Δx and let $i_h(x, t)$ be the current carried by strand h at time t at the first extreme of the segment. Let $J_{h,k}(x, t)$ be the current flowing from strand h to strand k , in correspondence to coordinate x , per unit length of cable. The following equation is derived from conservation of charge:

APPENDIX A
FROM FIELD THEORY TO THE
DISTRIBUTED PARAMETERS
CIRCUIT MODEL

the model equations can underlying hypotheses of the parameters.

cable is made of N strands and curvilinear axis. The supposed to be known. Let's

$$\frac{\partial i_h}{\partial x}(x,t) = \sum_{k=1}^N J_{k,h}(x,t) \quad (\text{A.1})$$

The electromagnetic field is described by means of the Maxwell equations in the magneto quasi-static formulation, in the absence of magnetization:

$$\begin{aligned} \nabla \times \mathbf{B} &= \mu_0 \mathbf{J} \\ \nabla \cdot \mathbf{B} &= 0 \\ \nabla \times \mathbf{E} &= - \frac{\partial \mathbf{B}}{\partial t} \end{aligned} \quad (\text{A.2})$$

From equations (A.2), the following expression of the electric field by means of the scalar electric potential V and the magnetic vector potential \mathbf{A} is derived:

$$\mathbf{E} = - \nabla V - \frac{\partial \mathbf{A}}{\partial t} \quad (\text{A.3})$$

Let's suppose that the magnetic vector potential \mathbf{A} has no component parallel to the cross section of the cable:

$$\mathbf{A}(\xi, \eta, x) \times \mathbf{t}_c(x) = 0 \quad (\text{A.4})$$

where \mathbf{t}_c is the unit vector tangent to the cable axis at position x and ξ and η are the local coordinates in the cross section of the cable.

The following equation is then derived from eq. (A.3):

$$\int_{R_h(x)}^{R_k(x)} \mathbf{E}(P) \cdot dP = V_h(x,t) - V_k(x,t) \quad (\text{A.5})$$

where $R_h(x)$ is the generic point of the axis line of strand h (see Fig. A.1).

Let the transversal per unit length conductance $g_{h,k}$ between strand h and strand k be defined by the following relation:

$$J_{h,k}(x,t) = g_{h,k}(x,t) [V_k(x,t) - V_h(x,t)] \quad (\text{A.6})$$

From equation (A.1) the following equation is obtained:

$$\frac{\partial i_h}{\partial x}(x,t) = \sum_{k=1}^N g_{h,k}(x,t) [V_k(x,t) - V_h(x,t)] \quad (\text{A.7})$$

Let a sector of cable of length Δx be considered.

By neglecting the variation of the electric potential in the cross section of the strand, the following equation is obtained for a sector of strand h , with reference to a point P_h with coordinates ξ and η in the cross section of the strand (see figure A.1):

$$\int_{P_h(x)}^{P_h(x+\Delta x)} \mathbf{E}(P, t) \cdot dP = V_h(x, t) - V_h(x + \Delta x, t) - \int_{P_h(x)}^{P_h(x+\Delta x)} \frac{\partial \mathbf{A}}{\partial t}(P, t) \cdot dP \quad (\text{A.8})$$

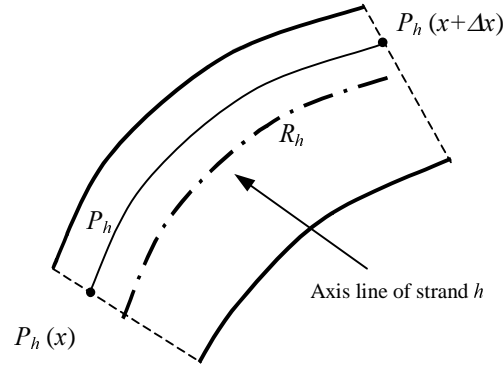


Fig. A.1. Scheme of a sector of strand h

Making use of the generalized Biot-Savart law the magnetic vector potential can be expressed as follows:

$$\begin{aligned} \mathbf{A}(P, t) = & \sum_{i=1}^{N_{ext}} \frac{\mu_0}{4\pi} \int_{\tau_{ext,i}} \frac{\mathbf{J}_{ext,i}(Q, t)}{r_{PQ}} d\tau_Q + \sum_{h=1}^N \frac{\mu_0}{4\pi} \int_{\tau_{h,1}(x)} \frac{\mathbf{J}_h(Q, t)}{r_{PQ}} d\tau_Q \\ & + \sum_{h=1}^N \frac{\mu_0}{4\pi} \int_{\Delta\tau_h(x, \Delta x)} \frac{\mathbf{J}_h(Q, t)}{r_{PQ}} d\tau_Q + \sum_{h=1}^N \frac{\mu_0}{4\pi} \int_{\tau_{h,2}(x+\Delta x)} \frac{\mathbf{J}_h(Q, t)}{r_{PQ}} d\tau_Q \end{aligned} \quad (\text{A.9})$$

where:

- $\tau_{ext,i}$ is the volume of the i^{th} external coil, $\mathbf{J}_{ext,i}$ is the current density vector in that coil and N_{ext} is the number of external coils,
- \mathbf{J}_h is the current density vector in strand h ,
- $\tau_{h,1}(x)$ is the volume of strand h from the inlet section to the section at coordinate x ,
- $\tau_{h,2}(x)$ is the volume of strand h from the section at coordinate x to the outlet section,
- $\Delta\tau_h(x, \Delta x)$ is the volume of strand h included between section at coordinate x and $x + \Delta x$.

The vector potential can be divided into two parts, corresponding to the sector considered and to the rest of the magnetic structure:

$$\mathbf{A}(P, t) = \mathbf{A}^{local} + \mathbf{A}^{ext} \quad (\text{A.10})$$

where:

$$\begin{aligned} \mathbf{A}^{local}(P, t) &= \sum_{h=1}^N \frac{\mu_0}{4\pi} \int_{\tau_{ext,i}} \frac{\mathbf{J}_{ext,i}(Q, t)}{r_{PQ}} d\tau_Q \\ \mathbf{A}^{ext}(P, t) &= \sum_{i=1}^{N_{ext}} \frac{\mu_0}{4\pi} \int_{\tau_{h,1}(x)} \frac{\mathbf{J}_h(Q, t)}{r_{PQ}} d\tau_Q + \sum_{h=1}^N \frac{\mu_0}{4\pi} \int_{\tau_{h,1}(x)} \frac{\mathbf{J}_h(Q, t)}{r_{PQ}} d\tau_Q \\ &\quad + \sum_{h=1}^N \frac{\mu_0}{4\pi} \int_{\tau_{h,1}(x)} \frac{\mathbf{J}_h(Q, t)}{r_{PQ}} d\tau_Q \end{aligned} \quad (\text{A.11})$$

From Equations (A.10) and (A.9) we obtain:

$$\begin{aligned} \int_{P_h(x)}^{P_h(x+\Delta x)} \mathbf{E}(P, t) \cdot dP &= [V_h(x, t) - V_h(x + \Delta x, t)] \\ &\quad - \sum_{k=1}^N \int_{P_h(x)}^{P_h(x+\Delta x)} \left[\frac{\mu_0}{4\pi} \int_{\Delta\tau_k(x, \Delta x)} \frac{\frac{\partial \mathbf{J}_k(Q, t)}{\partial t}}{r_{PQ}} d\tau_Q \right] \cdot dP \\ &\quad - \int_{P_h(x)}^{P_h(x+\Delta x)} \frac{\partial \mathbf{A}^{ext}(P, t)}{\partial t} \cdot dP \end{aligned} \quad (\text{A.12})$$

The operation current of the cable is a known variable given by:

$$i_{op}(t) = \sum_{h=1}^N i_h(x, t) \quad (\text{A.13})$$

The longitudinal resistance per unit length along the strand axis of strand h , $r_{s,h}$, is defined by the following relation:

$$\begin{aligned} r_{s,h}(x, t, \Delta x) &= \frac{\int_{\Delta\tau_h(x, \Delta x)} \mathbf{E}(P, t) \cdot \mathbf{J}(P, t) d\tau_P}{\Delta\ell_h i_h^2(x, t)} = \\ &= \frac{\int_{\Delta\tau_h(x, \Delta x)} \mathbf{E}(P, t) \cdot \mathbf{t}_h(P) d\tau_P}{\Delta\ell_h S_h i_h(x, t)} \end{aligned} \quad (\text{A.14})$$

Integrating equation (A.12) on the cross-section of strand h , in the hypothesis of an uniform external potential on the strand cross-section, by means of (A.14) we obtain:

$$\begin{aligned}
r_{s,h}(x,t,\Delta x)i_h(x,t)\Delta\ell_h &= [V_h(x,t) - V_h(x+\Delta x,t)] \\
&- \sum_{k=1}^N \int_{\Delta\tau_k(x,\Delta x)} \left[\frac{\mu_0}{4\pi} \int_{\Delta\tau_k(x,\Delta x)} \frac{\partial i_k}{\partial t}(x,t) \frac{\mathbf{t}_k(Q) \cdot \mathbf{t}_h(P)}{S_k S_h r_{PQ}} d\tau_Q \right] d\tau_P \\
&- \int_{R_h(x)}^{R_h(x+\Delta x)} \frac{\partial \mathbf{A}^{ext}(R,t)}{\partial t} \cdot dR
\end{aligned} \tag{A.15}$$

which can be written in the following form dividing by Δx :

$$\begin{aligned}
r_{s,h}(x,t,\Delta x)i_h(x,t) \frac{\Delta\ell_h}{\Delta x} &= \frac{V_h(x,t) - V_h(x+\Delta x,t)}{\Delta x} \\
&- \sum_{k=1}^N \frac{L_{h,k}(x,\Delta x)}{\Delta x} \frac{\partial i_k}{\partial t}(x,t) \\
&- \frac{1}{\Delta x} \int_{R_h(x)}^{R_h(x+\Delta x)} \frac{\partial \mathbf{A}^{ext}(R,t)}{\partial t} \cdot dR
\end{aligned} \tag{A.16}$$

where:

$$L_{h,k}(x,\Delta x) = \frac{\mu_0}{4\pi} \frac{1}{S_k S_h} \int_{\Delta\tau_k(x,\Delta x)} \int_{\Delta\tau_h(x,\Delta x)} \frac{\mathbf{t}_h(Q) \cdot \mathbf{t}_k(P)}{r_{PQ}} d\tau_P d\tau_Q \tag{A.17}$$

Equation (A.16) is a difference equation which depends on the amplitude Δx of the cable sector considered. In order to obtain a differential equation, a process of limit must be performed on equation (A.16).

$$r_h(x,t)i_h(x,t) = - \frac{\partial V_h}{\partial x}(x,t) - \sum_{k=1}^N l_{h,k}(x) \frac{\partial i_k}{\partial t}(x,t) + v_h^{ext}(x,t) \tag{A.18}$$

where:

$$r_h(x,t) = r_{s,h}(x,t) \frac{dl_h}{dx} = \frac{r_{sh}(x,t)}{\cos \gamma_h} \tag{A.19}$$

$$l_{h,k}(x) = \lim_{\Delta x \rightarrow 0} \frac{L_{h,k}(x,\Delta x)}{\Delta x} \tag{A.20}$$

$$v_h^{ext}(x,t) = -\lim_{\Delta x \rightarrow 0} \frac{1}{\Delta x} \int_{R_h(x)}^{R_h(x+\Delta x)} \frac{\partial \mathbf{A}^{ext}(R,t)}{\partial t} \cdot dR = -\frac{\partial \mathbf{A}^{ext}(R_h(x),t)}{\partial t} \cdot \mathbf{t}_h(x) \frac{1}{\cos(\gamma_h)} \quad (\text{A.21})$$

In equations (A.19 - A.21) r_h is the longitudinal resistance of strand h per unit length of cable, and γ_h the angle between the direction of the strand axis and the direction of the cable at coordinate x along the cable length.

Equation (A.18) is equal to equation (3.2), so that all parameters appearing in the model have been identified.

APPENDIX B NUMERICAL CALCULATION OF SELF AND MUTUAL INDUCTANCES

Generic strand geometry

The calculation of mutual inductances between sectors of different strands is necessary to develop the electromagnetic model of multistrand superconducting cables.

Several computer codes have been developed in order to calculate the induction coefficients for the case of a generic geometric disposition of the strands.

The induction coefficients are calculated making the following assumptions. It is assumed that the geometry of the wire is generated by a continuous motion of a flat surface in space. The surface moves perpendicular to the trajectory of the surface center of mass, which is the wire axis. The current density is considered to be homogenous in every wire cross-section, with the direction

of the tangent to the wire axis in the center of mass of the cross section considered. In the case considered here all wires are assumed to have a circular cross section, so that the center of mass simply corresponds to the center of the section.

The current density $\mathbf{J}(P)$ in a generic point P of the wire can be then expressed as follows:

$$\mathbf{J}(P) = \frac{i}{S} \mathbf{t}(P) \quad (B.1)$$

where \mathbf{t} is the unit vector normal to the cross section of the wire which includes P (and obviously tangent to the wire axis), S the area of the cross section and i the current flowing in the wire.

Under these hypotheses the mutual inductance between a generic sector i of strand h and a generic sector j of strand k with volumes $\tau_{h,i}$ and $\tau_{k,j}$ can be obtained by means of the following expression:

$$L_{h,i,k,j} = \frac{\mu_0}{4\pi} \int_{\tau_{h,i}} \int_{\tau_{k,j}} \frac{\mathbf{f}_h(P) \cdot \mathbf{f}_k(Q)}{r_{PQ}} d\tau_P d\tau_Q \quad (B.2)$$

where:

$$\mathbf{f}_h(P) = \frac{\mathbf{t}_h(P)}{S_h}$$

(B.3.a)

$$\mathbf{f}_k(Q) = \frac{\mathbf{t}_k(Q)}{S_k} \quad (B.3.b)$$

μ_0 is the permeability of vacuum, r_{PQ} is the distance between two generic points P and Q “moving” in volume $\tau_{h,i}$ and $\tau_{k,j}$ respectively.

The self inductance of a generic sector i of strand h with volume $\tau_{h,i}$ calculated in the same hypothesis is given by:

$$L_{h,i} = L_{h,i,h,i} = \frac{\mu_0}{4\pi} \int_{\tau_{h,i}} \int_{\tau_{h,i}} \frac{\mathbf{f}_h(P) \cdot \mathbf{f}_h(P')}{r_{PP'}} d\tau_P d\tau_{P'}, \quad (B.4)$$

where the meanings of symbols are analogous to those defined for equation (B.2).

The approximation introduced considering a uniform current density in the strand cross section is equivalent to neglect the non uniformities of current distribution inside each strand due to the presence of different materials (superconducting filaments and copper matrix) and to the coupling currents flowing among the filaments through the copper matrix.

Equations (B.2) and (B.4) can be integrated numerically by means of a recursive adaptive integration based on Gauss formula. Most problems arise when integrating equation (B.4) for the calculation of mutual inductances, because of the singularity obtained when P coincides with P' .

The numerical integration of equation (B.4) can be performed using the following numerical artefact:

$$L_{h,i,\varepsilon} = \frac{\mu_0}{4\pi} \int_{\tau_{h,i}} \int_{\tau_{h,j}} \frac{\mathbf{f}_h(P) \cdot \mathbf{f}_h(P')}{r_{PP'} + \varepsilon} d\tau_P d\tau_{P'}, \quad (\text{B.5})$$

where ε is a distance which should be taken as small as possible, verifying the convergence of the integral. It can be shown that the values of $L_{h,i,\varepsilon}$ calculated with definition (B.5) converge to the definition (B.4) when ε tends to zero. In fact it is possible to demonstrate the following relation [71]:

$$\lim_{\varepsilon \rightarrow 0} L_{h,i,\varepsilon} = L_{h,i} \quad (\text{B.6})$$

It is useful for the following calculations to introduce two different coordinate systems defined in the following way. The first system is a rectangular cartesian coordinate system with origin in point O and axis a , b and c .

The second coordinate system is a curvilinear coordinates system defined as follows:

x = parametric coordinate which follows the trajectory of the strand axis

r = radial polar coordinate varying in the strand cross section

α = azimuth angle (in the range $0, 2\pi$).

A generic cross section of strand h is defined by means of two unit vectors $\mathbf{u}_h(x)$ and $\mathbf{v}_h(x)$ orthogonal to vector $\mathbf{t}_h(x)$. The generic point $P_h(x)$ in the cross section of the strand h at coordinate x can be expressed as follows:

$$P_h(x) = R_h(x) + r \cos(\alpha) \mathbf{u}_h(x) + r \sin(\alpha) \mathbf{v}_h(x) \quad (\text{B.7})$$

where $R_h(x)$ is the point of the strand axis corresponding to the same cross section as point P .

The three unit vectors of the local reference frame can be found as follows:

$$\mathbf{t}_h(x) = \frac{\frac{dR_h(x)}{dx}}{\left| \frac{dR_h(x)}{dx} \right|} \quad (\text{B.8})$$

$$\mathbf{u}_h(x) = \frac{\frac{d^2 R_h(x)}{dx^2}}{\left| \frac{d^2 R_h(x)}{dx^2} \right|} \quad (\text{B.9})$$

$$\mathbf{v}_h(x) = \mathbf{t}_h(x) \times \mathbf{u}_h(x) \quad (\text{B.10})$$

If the trajectory of each strand axis is analytically known, i.e. if $R_h(x)$ is analytically known, all the terms of equations (B.8) through (B.10) can be easily evaluated by means of direct derivation. If the line of the strand axis is defined by the position of a sufficient number of points along the strand axis, the terms in equations (B.8)-(B.10) can be calculated via spline interpolation.

In order to evaluate the volume integral of eq. (B.2) and (B.4), it is necessary to calculate the Jacobian of the coordinates transformation from the coordinates a, b, c to the coordinates x, r, α . The Jacobian is the determinant of the transformation matrix \mathbf{J}_m :

$$|\mathbf{J}_m| = \begin{vmatrix} \frac{\partial a}{\partial x} & \frac{\partial a}{\partial r} & \frac{\partial a}{\partial \alpha} \\ \frac{\partial b}{\partial x} & \frac{\partial b}{\partial r} & \frac{\partial b}{\partial \alpha} \\ \frac{\partial c}{\partial x} & \frac{\partial c}{\partial r} & \frac{\partial c}{\partial \alpha} \end{vmatrix} \quad (\text{B.11})$$

All the terms comparing in the Jacobian matrix can be easily determined given the strand geometry. Defining with x_h, r_h and α_h , the mixed coordinates referred to strand h and with x_k, r_k and α_k the mixed coordinates referred to strand k , the evaluation of the integral in eq. (B.2) is straightforward:

$$\begin{aligned} M_{h,i,k,j} &= \frac{\mu_0}{4\pi S_{str}^2} \int_{\tau_{h,i}} da_h db_h dc_h \int_{\tau_{k,j}} \frac{\mathbf{t}_h(P) \cdot \mathbf{t}_k(Q)}{r_{PQ}} da_k db_k dc_k = \\ &= \frac{\mu_0}{4\pi S_{str}^2} \int_0^{2\pi} d\alpha_h \int_0^{R_s} dr_h \int_0^{L_{h,i}} dx_h \int_0^{2\pi} d\alpha_k \int_0^{R_s} dr_k \int_0^{L_{k,j}} dx_k \frac{\mathbf{t}_h(P) \cdot \mathbf{t}_k(Q)}{r_{PQ}} |\mathbf{J}_{mh}| |\mathbf{J}_{mk}| \end{aligned} \quad (\text{B.12})$$

where R_s is the radius of all strands, \mathbf{J}_{mh} and \mathbf{J}_{mk} are the Jacobian matrices relative to strand h and strand k and $L_{h,i}$ and $L_{k,j}$ the developed lengths of the strand sectors considered.

In a similar way the integral in eq. (B.5) can be calculated as follows:

$$L_{h,i} = \frac{\mu_0}{4\pi S_{str}^2} \int_0^{2\pi} d\alpha_h \int_0^{R_s} dr_h \int_0^{L_{h,i}} dx_h \int_0^{2\pi} d\alpha'_h \int_0^{R_s} dr'_h \int_0^{L_{h,i}} dx'_h \frac{\mathbf{t}_h(P) \cdot \mathbf{t}_h(P')}{r_{PP'}} |\mathbf{J}_{mh}|^2 \quad (\text{B.13})$$

Example of application: a triplex cable

In the case of a triplex cable with straight axis along z , the cartesian components of the helicoidal lines describing the strands axes can be defined analytically in the following way:

$$\begin{aligned} c_a(x) &= D \cos(\vartheta_{0h} + \varpi x) \\ c_b(x) &= D \sin(\vartheta_{0h} + \varpi x) \\ c_c(x) &= x \end{aligned} \quad (\text{B.14})$$

where:

$\varpi = \frac{2\pi}{L_P}$ is the winding velocity, L_P the cable twist pitch, $\vartheta_{0h} = (h-1)\frac{2\pi}{3}$, $h=1,3$ is the initial

angle of the h^{th} helix and D is the distance between the axes of the helices.

The unit vectors of the local reference frame can be found from equations (B.8)-(B.10), obtaining:

$$\begin{aligned}
 t_{ha} &= -D\varpi \sin(\vartheta_{0h} + \varpi x) \\
 t_{hb} &= D\varpi \cos(\vartheta_{0h} + \varpi x) \\
 t_{hc} &= 1 \\
 u_{ha} &= -\cos(\vartheta_{0h} + \varpi x) \\
 u_{hb} &= -\sin(\vartheta_{0h} + \varpi x) \\
 u_{hc} &= 0 \\
 v_{ha} &= \frac{\sin(\vartheta_{0h} + \varpi x)}{\sqrt{1 + D^2\varpi^2}} \\
 v_{hb} &= -\frac{\cos(\vartheta_{0h} + \varpi x)}{\sqrt{1 + D^2\varpi^2}} \\
 v_{hc} &= \frac{D\varpi}{\sqrt{1 + D^2\varpi^2}}
 \end{aligned} \tag{B.15}$$

The elements of the Jacobian matrix result in:

where $J_{i,j}$ is the element i, j of matrix \mathbf{J}_{mh} .

(B.16)

$$\begin{aligned}
J_{11} &= -\cos(\alpha)\cos(\theta_{0h} + \bar{\omega}x) + \frac{\sin(\alpha)\sin(\theta_{0h} + \bar{\omega}x)}{\sqrt{1 + D^2\bar{\omega}^2}} \\
J_{21} &= -\cos(\alpha)\sin(\theta_{0h} + \bar{\omega}x) - \frac{\sin(\alpha)\cos(\theta_{0h} + \bar{\omega}x)}{\sqrt{1 + D^2\bar{\omega}^2}} \\
J_{31} &= \sin(\alpha)\frac{D\bar{\omega}}{\sqrt{1 + D^2\bar{\omega}^2}} \\
J_{12} &= r\sin(\alpha)\cos(\theta_{0h} + \bar{\omega}x) + r\cos(\alpha)\frac{\sin(\theta_{0h} + \bar{\omega}x)}{\sqrt{1 + D^2\bar{\omega}^2}} \\
J_{22} &= r\sin(\alpha)\sin(\theta_{0h} + \bar{\omega}x) - r\cos(\alpha)\frac{\cos(\theta_{0h} + \bar{\omega}x)}{\sqrt{1 + D^2\bar{\omega}^2}} \\
J_{32} &= r\cos(\alpha)\frac{a\bar{\omega}}{\sqrt{1 + D^2\bar{\omega}^2}} \\
J_{13} &= -D\bar{\omega}\sin(\theta_{0h} + \bar{\omega}x) + r\bar{\omega}\cos(\alpha)\sin(\theta_{0h} + \bar{\omega}x) + \\
&\quad + r\bar{\omega}\sin(\alpha)\frac{\cos(\theta_{0h} + \bar{\omega}x)}{\sqrt{1 + D^2\bar{\omega}^2}} \\
J_{23} &= D\bar{\omega}\cos(\theta_{0h} + \bar{\omega}x) - r\bar{\omega}\cos(\alpha)\cos(\theta_{0h} + \bar{\omega}x) + \\
&\quad + r\bar{\omega}\sin(\alpha)\frac{\sin(\theta_{0h} + \bar{\omega}x)}{\sqrt{1 + D^2\bar{\omega}^2}} \\
J_{33} &= 1
\end{aligned}$$

The scalar product $\mathbf{t}_h(s_h) \cdot \mathbf{t}_k(s_k)$ is given by:

$$\begin{aligned}
\mathbf{t}_h(s_h) \cdot \mathbf{t}_k(s_k) &= \frac{1}{1 + D^2\bar{\omega}^2} (D^2\bar{\omega}^2 \sin(\theta_{0h} + \bar{\omega}x_h) \sin(\theta_{0k} + \bar{\omega}x_k) \\
&\quad + D^2\bar{\omega}^2 \cos(\theta_{0h} + \bar{\omega}x_h) \cos(\theta_{0k} + \bar{\omega}x_k) + 1)
\end{aligned}$$

(B.17)

The mutual inductances between any two sectors of two generic strands h and k can be then determined with an appropriate choice of the integration extremes in eq. (B.12).

Example of application: Rutherford cable

The strands in a flat cable are assumed to be made of straight cylinders layered alternatively in the upper and lower face of the cable. Starting from a generic position along the cable axis we consider all the cylinders of each strand within a certain number of cable pitches, in order to smear the periodic variations of the inductances matrix along the cable axis.

If we consider p pitches of cable the total number of cylinders for each strand introduced in the calculations is equal to $2p$ or $2p + 1$, depending on the strand chosen. As an example, the cylinders considered for the calculation of the mutual inductances matrix for strand 1 (2 cylinders) and strand 3 (3 cylinders) in the case of a calculation for 1 pitch are shown in Fig. 2.3.

The mutual inductance between a generic cylinder i of strand h and a generic cylinder j of strand k is calculated by means of an adaptive recursive numerical integration of formula (B.2):

$$M_{h,i,k,j} = \frac{\mu_0}{4\pi} \frac{S_{str}^2}{\tau_{h,i} \tau_{k,j}} \int \int \frac{\mathbf{t}_{h,i}(P) \cdot \mathbf{t}_{k,j}(Q)}{r_{PQ}} d\tau_P d\tau_Q \quad (\text{B.18})$$

$\tau_{h,i}$, $\tau_{k,j}$ are the volumes of the strands segments. Once the mutual inductances between all the strand sectors are known, the elements of the matrix of the self and mutual inductances per unit length (see section can be calculated as follows:

$$l_{h,k} = \frac{\sum_{i=1}^{C(h)} \sum_{j=1}^{C(k)} M_{h,i,k,j}}{pL_p} \quad (\text{B.19})$$

where $C(h)$ is the number of cylinders owing to strand h along the p pitches considered.

It is worth remarking that the absolute values of the mutual induction coefficients change with the number of cable pitches chosen for the smearing. However, only differences between these coefficients appear in the final equations in the matrix \mathbf{gl} of equation (3.7). We have verified that the elements of matrix \mathbf{gl} are quickly convergent with the number of pitches, obtaining a constant value within 6 - 7% after 10 twist pitches. As we are interested to study effects that involve many twist pitches (up to the whole cable length), we believe that in general these variations do not affect substantially the final current distribution, and we have verified it in the test cases reported in this thesis.

As an example, the mutual inductances matrix per unit length \mathbf{l} calculated for a 16 strand cable used for the simulations reported in Section 3.3 is reported in (B.20). The matrix was calculated using eq. (B.19) where p was taken equal to 1.

It can be noticed that the values of mutual inductances per unit length are equal for all strands having the same distance between their axes along the cable length. As an example, considering strand 1 and strand 16 their distance is equal to that between strand 1 and 2 or strand 2 and 3 and so on. The same happens for strand 2 and 4, or 3 and 5. This property makes the matrix

of mutual inductances circulant (see [63] and Appendix C). This property is very useful for a straightforward evaluation of the eigenvectors and eigenvalues of matrix \mathbf{I} that are needed for the analytical solution of the problem equations (see Chapter 4).

$$\mathbf{I} = \begin{pmatrix} 1.68 & 1.49 & 1.37 & 1.30 & 1.27 & 1.24 & 1.23 & 1.23 & 1.22 & 1.23 & 1.23 & 1.24 & 1.27 & 1.30 & 1.36 & 1.49 \\ 1.49 & 1.68 & 1.49 & 1.37 & 1.30 & 1.27 & 1.24 & 1.23 & 1.23 & 1.22 & 1.23 & 1.23 & 1.24 & 1.27 & 1.30 & 1.36 \\ 1.37 & 1.49 & 1.68 & 1.49 & 1.37 & 1.30 & 1.27 & 1.24 & 1.23 & 1.23 & 1.22 & 1.23 & 1.23 & 1.24 & 1.27 & 1.30 \\ 1.30 & 1.37 & 1.49 & 1.68 & 1.49 & 1.37 & 1.30 & 1.27 & 1.24 & 1.23 & 1.23 & 1.22 & 1.23 & 1.23 & 1.24 & 1.27 \\ 1.27 & 1.30 & 1.37 & 1.49 & 1.68 & 1.49 & 1.37 & 1.30 & 1.27 & 1.24 & 1.23 & 1.23 & 1.22 & 1.23 & 1.23 & 1.24 \\ 1.24 & 1.27 & 1.30 & 1.37 & 1.49 & 1.68 & 1.49 & 1.37 & 1.30 & 1.27 & 1.24 & 1.23 & 1.23 & 1.22 & 1.23 & 1.23 \\ 1.23 & 1.24 & 1.27 & 1.30 & 1.37 & 1.49 & 1.68 & 1.49 & 1.36 & 1.30 & 1.27 & 1.24 & 1.23 & 1.23 & 1.22 & 1.23 \\ 1.22 & 1.23 & 1.24 & 1.27 & 1.30 & 1.37 & 1.49 & 1.68 & 1.48 & 1.36 & 1.30 & 1.27 & 1.24 & 1.23 & 1.23 & 1.22 \\ 1.22 & 1.23 & 1.23 & 1.24 & 1.27 & 1.30 & 1.36 & 1.48 & 1.68 & 1.49 & 1.37 & 1.30 & 1.27 & 1.24 & 1.23 & 1.22 \\ 1.23 & 1.22 & 1.23 & 1.23 & 1.24 & 1.27 & 1.30 & 1.36 & 1.49 & 1.68 & 1.49 & 1.37 & 1.30 & 1.27 & 1.24 & 1.23 \\ 1.23 & 1.23 & 1.22 & 1.23 & 1.23 & 1.24 & 1.27 & 1.30 & 1.37 & 1.49 & 1.68 & 1.49 & 1.37 & 1.30 & 1.27 & 1.24 \\ 1.24 & 1.23 & 1.23 & 1.22 & 1.23 & 1.23 & 1.24 & 1.27 & 1.30 & 1.37 & 1.49 & 1.68 & 1.49 & 1.37 & 1.30 & 1.27 \\ 1.27 & 1.24 & 1.23 & 1.23 & 1.22 & 1.23 & 1.23 & 1.24 & 1.27 & 1.30 & 1.37 & 1.49 & 1.68 & 1.49 & 1.37 & 1.30 \\ 1.30 & 1.27 & 1.24 & 1.23 & 1.23 & 1.22 & 1.23 & 1.23 & 1.24 & 1.27 & 1.30 & 1.37 & 1.49 & 1.68 & 1.49 & 1.37 \\ 1.36 & 1.30 & 1.27 & 1.24 & 1.23 & 1.23 & 1.22 & 1.23 & 1.23 & 1.24 & 1.27 & 1.30 & 1.37 & 1.49 & 1.68 & 1.49 \\ 1.49 & 1.36 & 1.30 & 1.27 & 1.24 & 1.23 & 1.23 & 1.22 & 1.22 & 1.23 & 1.24 & 1.27 & 1.30 & 1.37 & 1.49 & 1.68 \end{pmatrix} \cdot 10^{-6} \text{ H/m} \quad (B.20)$$

APPENDIX B NUMERICAL CALCULATION OF SELF AND MUTUAL INDUCTANCES

Generic strand geometry

The calculation of mutual inductances between sectors of different strands is necessary to develop the electromagnetic model of multistrand superconducting cables.

Several computer codes have been developed in order to calculate the induction coefficients for the case of a generic geometric disposition of the strands.

The induction coefficients are calculated making the following assumptions. It is assumed that the geometry of the wire is generated by a continuous motion of a flat surface in space. The surface moves perpendicular to the trajectory of the surface center of mass, which is the wire axis. The current density is considered to be homogenous in every wire cross-section, with the direction of the tangent to the wire axis in the center of mass of the cross section considered. In the case considered here all wires are assumed to have a circular cross section, so that the center of mass simply corresponds to the center of the section.

The current density $\mathbf{J}(\mathbf{P})$ in a generic point \mathbf{P} of the wire can be then expressed as follows:

$$\mathbf{J}(P) = \frac{i}{S} \mathbf{t}(P) \quad (B.1)$$

where \mathbf{t} is the unit vector normal to the cross section of the wire which includes P (and obviously tangent to the wire axis), S the area of the cross section and i the current flowing in the wire.

Under these hypotheses the mutual inductance between a generic sector i of strand h and a generic sector j of strand k with volumes $\tau_{h,i}$ and $\tau_{k,j}$ can be obtained by means of the following expression:

$$L_{h,i,k,j} = \frac{\mu_0}{4\pi} \int_{\tau_{h,i}} \int_{\tau_{k,j}} \frac{\mathbf{f}_h(P) \cdot \mathbf{f}_k(Q)}{r_{PQ}} d\tau_P d\tau_Q \quad (B.2)$$

where:

$$\mathbf{f}_h(P) = \frac{\mathbf{t}_h(P)}{S_h}$$

(B.3.a)

$$\mathbf{f}_k(Q) = \frac{\mathbf{t}_k(Q)}{S_k} \quad (B.3.b)$$

μ_0 is the permeability of vacuum, r_{PQ} is the distance between two generic points P and Q “moving” in volume $\tau_{h,i}$ and $\tau_{k,j}$ respectively.

The self inductance of a generic sector i of strand h with volume τ_h calculated in the same hypothesis is given by:

$$L_{h,i} = L_{h,i,h,i} = \frac{\mu_0}{4\pi} \int_{\tau_{h,i}} \int_{\tau_{h,i}} \frac{\mathbf{f}_h(P) \cdot \mathbf{f}_h(P')}{r_{PP'}} d\tau_P d\tau_{P'} \quad (B.4)$$

where the meanings of symbols are analogous to those defined for equation (B.2).

The approximation introduced considering a uniform current density in the strand cross section is equivalent to neglect the non uniformities of current distribution inside each strand due to the presence of different materials (superconducting filaments and copper matrix) and to the coupling currents flowing among the filaments through the copper matrix.

Equations (B.2) and (B.4) can be integrated numerically by means of a recursive adaptive integration based on Gauss formula. Most problems arise when integrating equation (B.4) for the calculation of mutual inductances, because of the singularity obtained when P coincides with P' .

The numerical integration of equation (B.4) can be performed using the following numerical artefact:

$$L_{h,i,\varepsilon} = \frac{\mu_0}{4\pi} \int_{\tau_{h,i}} \int_{\tau_{h,i}} \frac{\mathbf{f}_h(P) \cdot \mathbf{f}_h(P')}{r_{PP'} + \varepsilon} d\tau_P d\tau_{P'}, \quad (\text{B.5})$$

where ε is a distance which should be taken as small as possible, verifying the convergence of the integral. It can be shown that the values of $L_{h,i,\varepsilon}$ calculated with definition (B.5) converge to the definition (B.4) when ε tends to zero. In fact it is possible to demonstrate the following relation [71]:

$$\lim_{\varepsilon \rightarrow 0} L_{h,i,\varepsilon} = L_{h,i} \quad (\text{B.6})$$

It is useful for the following calculations to introduce two different coordinate systems defined in the following way. The first system is a rectangular cartesian coordinate system with origin in point O and axis a , b and c .

The second coordinate system is a curvilinear coordinates system defined as follows:

x = parametric coordinate which follows the trajectory of the strand axis

r = radial polar coordinate varying in the strand cross section

α = azimuth angle (in the range $0, 2\pi$).

A generic cross section of strand h is defined by means of two unit vectors $\mathbf{u}_h(x)$ and $\mathbf{v}_h(x)$ orthogonal to vector $\mathbf{t}_h(x)$. The generic point $P_h(x)$ in the cross section of the strand h at coordinate x can be expressed as follows:

$$P_h(x) = R_h(x) + r \cos(\alpha) \mathbf{u}_h(x) + r \sin(\alpha) \mathbf{v}_h(x) \quad (\text{B.7})$$

where $R_h(x)$ is the point of the strand axis corresponding to the same cross section as point P .

The three unit vectors of the local reference frame can be found as follows:

$$\mathbf{t}_h(x) = \frac{\frac{dR_h(x)}{dx}}{\left| \frac{dR_h(x)}{dx} \right|} \quad (\text{B.8})$$

$$\mathbf{u}_h(x) = \frac{\frac{d^2 R_h(x)}{dx^2}}{\left| \frac{d^2 R_h(x)}{dx^2} \right|} \quad (\text{B.9})$$

$$\mathbf{v}_h(x) = \mathbf{t}_h(x) \times \mathbf{u}_h(x) \quad (\text{B.10})$$

If the trajectory of each strand axis is analytically known, i.e. if $R_h(x)$ is analytically known, all the terms of equations (B.8) through (B.10) can be easily evaluated by means of direct derivation. If the line of the strand axis is defined by the position of a sufficient number of points along the strand axis, the terms in equations (B.8)-(B.10) can be calculated via spline interpolation.

In order to evaluate the volume integral of eq. (B.2) and (B.4), it is necessary to calculate the Jacobian of the coordinates transformation from the coordinates a, b, c to the coordinates x, r, α . The Jacobian is the determinant of the transformation matrix \mathbf{J}_m :

$$|\mathbf{J}_m| = \begin{vmatrix} \frac{\partial a}{\partial x} & \frac{\partial a}{\partial r} & \frac{\partial a}{\partial \alpha} \\ \frac{\partial b}{\partial x} & \frac{\partial b}{\partial r} & \frac{\partial b}{\partial \alpha} \\ \frac{\partial c}{\partial x} & \frac{\partial c}{\partial r} & \frac{\partial c}{\partial \alpha} \end{vmatrix} \quad (\text{B.11})$$

All the terms comparing in the Jacobian matrix can be easily determined given the strand geometry. Defining with x_h, r_h and α_h , the mixed coordinates referred to strand h and with x_k, r_k , and α_k the mixed coordinates referred to strand k , the evaluation of the integral in eq. (B.2) is straightforward:

$$\begin{aligned} M_{h,i,k,j} &= \frac{\mu_0}{4\pi S_{str}^2} \int_{\tau_{h,i}} da_h db_h dc_h \int_{\tau_{k,j}} \frac{\mathbf{t}_h(P) \cdot \mathbf{t}_k(Q)}{r_{PQ}} da_k db_k dc_k = \\ &= \frac{\mu_0}{4\pi S_{str}^2} \int_0^{2\pi} d\alpha_h \int_0^{R_s} dr_h \int_0^{L_{h,i}} dx_h \int_0^{2\pi} d\alpha_k \int_0^{R_s} dr_k \int_0^{L_{k,j}} dx_k \frac{\mathbf{t}_h(P) \cdot \mathbf{t}_k(Q)}{r_{PQ}} |\mathbf{J}_{mh}| |\mathbf{J}_{mk}| \end{aligned} \quad (\text{B.12})$$

where R_s is the radius of all strands, \mathbf{J}_{mh} and \mathbf{J}_{mk} are the Jacobian matrices relative to strand h and strand k and $L_{h,i}$ and $L_{k,j}$ the developed lengths of the strand sectors considered.

In a similar way the integral in eq. (B.5) can be calculated as follows:

$$L_{h,i} = \frac{\mu_0}{4\pi S_{str}^2} \int_0^{2\pi} d\alpha_h \int_0^{R_s} dr_h \int_0^{L_{h,i}} dx_h \int_0^{2\pi} d\alpha'_h \int_0^{R_s} dr'_h \int_0^{L_{h,i}} dx'_h \frac{\mathbf{t}_h(P) \cdot \mathbf{t}_h(P')}{r_{PP'}} |\mathbf{J}_{mh}|^2 \quad (\text{B.13})$$

Example of application: a triplex cable

In the case of a triplex cable with straight axis along z, the cartesian components of the helicoidal lines describing the strands axes can be defined analytically in the following way:

$$\begin{aligned} c_a(x) &= D \cos(\vartheta_{0h} + \varpi x) \\ c_b(x) &= D \sin(\vartheta_{0h} + \varpi x) \\ c_c(x) &= x \end{aligned} \quad (\text{B.14})$$

where:

$\varpi = \frac{2\pi}{L_P}$ is the winding velocity, L_P the cable twist pitch, $\vartheta_{0h} = (h-1)\frac{2\pi}{3}$, $h=1,3$ is the initial

angle of the h^{th} helix and D is the distance between the axes of the helices.

The unit vectors of the local reference frame can be found from equations (B.8)-(B.10), obtaining:

$$\begin{aligned}
 t_{ha} &= -D\varpi \sin(\vartheta_{0h} + \varpi x) \\
 t_{hb} &= D\varpi \cos(\vartheta_{0h} + \varpi x) \\
 t_{hc} &= 1 \\
 u_{ha} &= -\cos(\vartheta_{0h} + \varpi x) \\
 u_{hb} &= -\sin(\vartheta_{0h} + \varpi x) \\
 u_{hc} &= 0 \\
 v_{ha} &= \frac{\sin(\vartheta_{0h} + \varpi x)}{\sqrt{1 + D^2 \varpi^2}} \\
 v_{hb} &= -\frac{\cos(\vartheta_{0h} + \varpi x)}{\sqrt{1 + D^2 \varpi^2}} \\
 v_{hc} &= \frac{D\varpi}{\sqrt{1 + D^2 \varpi^2}}
 \end{aligned} \tag{B.15}$$

The elements of the Jacobian matrix result in:

where $J_{i,j}$ is the element i, j of matrix \mathbf{J}_{mh} .

(B.16)

$$\begin{aligned}
J_{11} &= -\cos(\alpha)\cos(\theta_{0h} + \bar{\omega}x) + \frac{\sin(\alpha)\sin(\theta_{0h} + \bar{\omega}x)}{\sqrt{1 + D^2\bar{\omega}^2}} \\
J_{21} &= -\cos(\alpha)\sin(\theta_{0h} + \bar{\omega}x) - \frac{\sin(\alpha)\cos(\theta_{0h} + \bar{\omega}x)}{\sqrt{1 + D^2\bar{\omega}^2}} \\
J_{31} &= \sin(\alpha)\frac{D\bar{\omega}}{\sqrt{1 + D^2\bar{\omega}^2}} \\
J_{12} &= r\sin(\alpha)\cos(\theta_{0h} + \bar{\omega}x) + r\cos(\alpha)\frac{\sin(\theta_{0h} + \bar{\omega}x)}{\sqrt{1 + D^2\bar{\omega}^2}} \\
J_{22} &= r\sin(\alpha)\sin(\theta_{0h} + \bar{\omega}x) - r\cos(\alpha)\frac{\cos(\theta_{0h} + \bar{\omega}x)}{\sqrt{1 + D^2\bar{\omega}^2}} \\
J_{32} &= r\cos(\alpha)\frac{a\bar{\omega}}{\sqrt{1 + D^2\bar{\omega}^2}} \\
J_{13} &= -D\bar{\omega}\sin(\theta_{0h} + \bar{\omega}x) + r\bar{\omega}\cos(\alpha)\sin(\theta_{0h} + \bar{\omega}x) + \\
&\quad + r\bar{\omega}\sin(\alpha)\frac{\cos(\theta_{0h} + \bar{\omega}x)}{\sqrt{1 + D^2\bar{\omega}^2}} \\
J_{23} &= D\bar{\omega}\cos(\theta_{0h} + \bar{\omega}x) - r\bar{\omega}\cos(\alpha)\cos(\theta_{0h} + \bar{\omega}x) + \\
&\quad + r\bar{\omega}\sin(\alpha)\frac{\sin(\theta_{0h} + \bar{\omega}x)}{\sqrt{1 + D^2\bar{\omega}^2}} \\
J_{33} &= 1
\end{aligned}$$

The scalar product $\mathbf{t}_h(s_h) \cdot \mathbf{t}_k(s_k)$ is given by:

$$\begin{aligned}
\mathbf{t}_h(s_h) \cdot \mathbf{t}_k(s_k) &= \frac{1}{1 + D^2\bar{\omega}^2} (D^2\bar{\omega}^2 \sin(\theta_{0h} + \bar{\omega}x_h) \sin(\theta_{0k} + \bar{\omega}x_k) \\
&\quad + D^2\bar{\omega}^2 \cos(\theta_{0h} + \bar{\omega}x_h) \cos(\theta_{0k} + \bar{\omega}x_k) + 1)
\end{aligned}$$

(B.17)

The mutual inductances between any two sectors of two generic strands h and k can be then determined with an appropriate choice of the integration extremes in eq. (B.12).

Example of application: Rutherford cable

The strands in a flat cable are assumed to be made of straight cylinders layered alternatively in the upper and lower face of the cable. Starting from a generic position along the cable axis we consider all the cylinders of each strand within a certain number of cable pitches, in order to smear the periodic variations of the inductances matrix along the cable axis.

If we consider p pitches of cable the total number of cylinders for each strand introduced in the calculations is equal to $2p$ or $2p + 1$, depending on the strand chosen. As an example, the cylinders considered for the calculation of the mutual inductances matrix for strand 1 (2 cylinders) and strand 3 (3 cylinders) in the case of a calculation for 1 pitch are shown in Fig. 2.3.

The mutual inductance between a generic cylinder i of strand h and a generic cylinder j of strand k is calculated by means of an adaptive recursive numerical integration of formula (B.2):

$$M_{h,i,k,j} = \frac{\mu_0}{4\pi} \frac{S_{str}^2}{\tau_{h,i} \tau_{k,j}} \int \int \frac{\mathbf{t}_{h,i}(P) \cdot \mathbf{t}_{k,j}(Q)}{r_{PQ}} d\tau_P d\tau_Q \quad (\text{B.18})$$

$\tau_{h,i}$, $\tau_{k,j}$ are the volumes of the strands segments. Once the mutual inductances between all the strand sectors are known, the elements of the matrix of the self and mutual inductances per unit length (see section can be calculated as follows:

$$l_{h,k} = \frac{\sum_{i=1}^{C(h)} \sum_{j=1}^{C(k)} M_{h,i,k,j}}{pL_p} \quad (\text{B.19})$$

where $C(h)$ is the number of cylinders owing to strand h along the p pitches considered.

It is worth remarking that the absolute values of the mutual induction coefficients change with the number of cable pitches chosen for the smearing. However, only differences between these coefficients appear in the final equations in the matrix \mathbf{gl} of equation (3.7). We have verified that the elements of matrix \mathbf{gl} are quickly convergent with the number of pitches, obtaining a constant value within 6 - 7% after 10 twist pitches. As we are interested to study effects that involve many twist pitches (up to the whole cable length), we believe that in general these variations do not affect substantially the final current distribution, and we have verified it in the test cases reported in this thesis.

As an example, the mutual inductances matrix per unit length \mathbf{l} calculated for a 16 strand cable used for the simulations reported in Section 3.3 is reported in (B.20). The matrix was calculated using eq. (B.19) where p was taken equal to 1.

It can be noticed that the values of mutual inductances per unit length are equal for all strands having the same distance between their axes along the cable length. As an example, considering strand 1 and strand 16 their distance is equal to that between strand 1 and 2 or strand 2 and 3 and so on. The same happens for strand 2 and 4, or 3 and 5. This property makes the matrix

of mutual inductances circulant (see [63] and Appendix C). This property is very useful for a straightforward evaluation of the eigenvectors and eigenvalues of matrix \mathbf{I} that are needed for the analytical solution of the problem equations (see Chapter 4).

$$\mathbf{I} = \begin{pmatrix} 1.68 & 1.49 & 1.37 & 1.30 & 1.27 & 1.24 & 1.23 & 1.23 & 1.22 & 1.23 & 1.23 & 1.24 & 1.27 & 1.30 & 1.36 & 1.49 \\ 1.49 & 1.68 & 1.49 & 1.37 & 1.30 & 1.27 & 1.24 & 1.23 & 1.23 & 1.22 & 1.23 & 1.23 & 1.24 & 1.27 & 1.30 & 1.36 \\ 1.37 & 1.49 & 1.68 & 1.49 & 1.37 & 1.30 & 1.27 & 1.24 & 1.23 & 1.23 & 1.22 & 1.23 & 1.23 & 1.24 & 1.27 & 1.30 \\ 1.30 & 1.37 & 1.49 & 1.68 & 1.49 & 1.37 & 1.30 & 1.27 & 1.24 & 1.23 & 1.23 & 1.22 & 1.23 & 1.23 & 1.24 & 1.27 \\ 1.27 & 1.30 & 1.37 & 1.49 & 1.68 & 1.49 & 1.37 & 1.30 & 1.27 & 1.24 & 1.23 & 1.23 & 1.22 & 1.23 & 1.23 & 1.24 \\ 1.24 & 1.27 & 1.30 & 1.37 & 1.49 & 1.68 & 1.49 & 1.37 & 1.30 & 1.27 & 1.24 & 1.23 & 1.23 & 1.22 & 1.23 & 1.23 \\ 1.23 & 1.24 & 1.27 & 1.30 & 1.37 & 1.49 & 1.68 & 1.49 & 1.36 & 1.30 & 1.27 & 1.24 & 1.23 & 1.23 & 1.22 & 1.23 \\ 1.22 & 1.23 & 1.24 & 1.27 & 1.30 & 1.37 & 1.49 & 1.68 & 1.48 & 1.36 & 1.30 & 1.27 & 1.24 & 1.23 & 1.23 & 1.22 \\ 1.22 & 1.23 & 1.23 & 1.24 & 1.27 & 1.30 & 1.36 & 1.48 & 1.68 & 1.49 & 1.37 & 1.30 & 1.27 & 1.24 & 1.23 & 1.22 \\ 1.23 & 1.22 & 1.23 & 1.23 & 1.24 & 1.27 & 1.30 & 1.36 & 1.49 & 1.68 & 1.49 & 1.37 & 1.30 & 1.27 & 1.24 & 1.23 \\ 1.23 & 1.23 & 1.22 & 1.23 & 1.23 & 1.24 & 1.27 & 1.30 & 1.37 & 1.49 & 1.68 & 1.49 & 1.37 & 1.30 & 1.27 & 1.24 \\ 1.24 & 1.23 & 1.23 & 1.22 & 1.23 & 1.23 & 1.24 & 1.27 & 1.30 & 1.37 & 1.49 & 1.68 & 1.49 & 1.37 & 1.30 & 1.27 \\ 1.27 & 1.24 & 1.23 & 1.23 & 1.22 & 1.23 & 1.23 & 1.24 & 1.27 & 1.30 & 1.37 & 1.49 & 1.68 & 1.49 & 1.37 & 1.30 \\ 1.30 & 1.27 & 1.24 & 1.23 & 1.23 & 1.22 & 1.23 & 1.23 & 1.24 & 1.27 & 1.30 & 1.37 & 1.49 & 1.68 & 1.49 & 1.37 \\ 1.36 & 1.30 & 1.27 & 1.24 & 1.23 & 1.23 & 1.22 & 1.23 & 1.23 & 1.24 & 1.27 & 1.30 & 1.37 & 1.49 & 1.68 & 1.49 \\ 1.49 & 1.36 & 1.30 & 1.27 & 1.24 & 1.23 & 1.23 & 1.22 & 1.22 & 1.23 & 1.24 & 1.27 & 1.30 & 1.37 & 1.49 & 1.68 \end{pmatrix} \cdot 10^{-6} \text{ H/m} \quad (B.20)$$

BIBLIOGRAPHY

- [1] T. P. Sheahen, Introduction to High Temperature Superconductivity, Plenum Press, New York, 1994
- [2] C.P. Poole, H. A. Farach, R. J. Creswick, Superconductivity, Academic Press, 1995
- [3] T. P. Orlando, K. A. Delin, Foundations of Applied Superconductivity, Addison Wesley Publishing Company, 1991
- [4] M. N. Wilson, Superconducting Magnets, Clarendon Press, Oxford, 1983
- [5] A. Devred, "Review of superconducting storage-ring dipole and quadrupole magnets", Cern Accelerator School, Anacapri Italy, April, 1997.
- [6] L. Bottura, "Field Dynamics in Superconducting Magnets for Particle Accelerators", Cern Accelerator School, Anacapri, Italy, 1997.
- [7] N. Amemiya, "Overview of current distribution and re-distribution in superconducting cables and their influence on stability", Cryogenics 38, 1998.

- [8] N. Mitchell, "Steady state analysis of non uniform current distributions in cable in conduit conductors and comparison with experimental data", *Cryogenics* 40, 2000.
- [9] L. Krempasky, C. Schmidt, "Influence of a longitudinal variation of dB/dt on the magnetic field distribution of superconducting accelerator magnets", *Appl. Phys. Lett.*, 66, 1995.
- [10] L. Krempasky, C. Schmidt, "Theory of "supercurrents" and their influence on field quality and stability of superconducting magnets", *Jour. Appl. Phys.*, 78 (9), 1995.
- [11] L. Krempasky, C. Schmidt, "Ramp rate limitation in large superconducting magnets due to 'supercurrents'", *Cryogenics*, 36 (6), 1996.
- [12] *L. Krempasky, C. Schmidt, "Experimental verification of 'supercurrents' in superconducting cables exposed to AC fields", Cryogenics 39, 1999.*
- [13] Schermer RI. "Status of Superconducting Magnets for the Superconducting Super Collider", *IEEE Trans. Mag.*, 30, 1994.
- [14] H. Brueck et al., "Observation of a Periodic Pattern in the Persistent Current Fields of the Superconducting HERA Dipole Magnets", *Proc. of 1991 Part. Acc. Conf.*, San Francisco, 1991.
- [15] A. K. Gosh, K. E. Robins, W. B. Sampson, "The Ramp Rate Dependence of the Sextupole Field in Superconducting Dipoles", *IEEE Trans. Mag.*, vol. 30 (4), 1994.
- [16] *A. K. Ghosh, K. E. Robins and W. B. Sampson, "Axial variations in the magnetic field of superconducting dipoles," Supercollider 4, 1992.*
- [17] *W. B. Sampson, A. K. Gosh, "Induced Axial Oscillations in Superconducting Dipole Windings," IEEE Trans. Appl. Sup., vol. 5 (2), 1995.*
- [18] G.H. Morgan. Eddy currents in flat metal-filled superconducting braids. *Jour. Appl. Phys.*, 44 (7), 1973.
- [19] A. Akhmetov, A. Devred, T. Ogitsu, "Periodicity of Cross-over Currents in a Rutherford-type Cable Subjected to a Time Dependent Magnetic Field", *Jour. Appl. Phys.*, vol. 75 (6), 1994.
- [20] A. Akhmetov, "Network models of superconducting cables and the results of the matrix approach to their description", *Physica C*, 310, 1998.
- [21] A. Akhmetov, K. Kuroda, T. Koga, K. Ono and M. Takeo, "Decay of long current loops in the superconducting cables" *Proceedings of EUCAS'95*, 1995, Scotland.
- [22] A. Akhmetov, K. Kuroda, K. Ono and M. Takeo, "Eddy currents in flat two-layer superconducting cables", *Cryogenics* 35, 1995.
- [23] A. Akhmetov, S. S. Ivanov, O. Shchegolev, "Further Analysis of the eigen frequency spectrum of a flat two-layer superconducting cable", *Supercond. Sci. Technol.* 13, 2000.
- [24] A. Akhmetov, A. Devred, R. Mints, R. Schermer, "Current Loop Decay in Rutherford Type Cables", *Supercollider* 5, 1993.
- [25] A. Akhmetov, K. Kuroda, M. Takeo, "Calculation of Composites Ramp Rate Sensitivity Based on Two Layer Model", *Proc. 14th Int. Conf Mag Tech*, Tampere, Finland, 1995.

- [26] A. P. Verweij, H.H.J. ten Kate, "Super Coupling Currents in Rutherford Type of Cables due to longitudinal Non-homogeneities of dB/dt ". IEEE Trans. Appl. Sup., 5 (2), 1995.
- [27] A Verweij, "Electrodynamics of Superconducting cables in Accelerator Magnets" Ph.D. Thesis, 1995, University of Twente, Enschede, (NL).
- [28] R. Wolf, "The Decay of the Field Integral in Superconducting Accelerator Magnets wound with Rutherford Cables", Presented MT15, Beijing, China, 1997.
- [29] M. Haverkamp, A. Kuijper, A. Den Ouden, B. ten Haken, L. Bottura and H. H. J. ten Kate, "Interaction between Current Imbalance and Magnetization in LHC cables", presented at Applied Superconductivity Conference, ASC 2000, Virginia Beach, USA, September 2000.
- [30] L.Bottura, M. Breschi, F. Negrini, P.L. Ribani. Electromagnetic analysis of current distribution in multistrand superconducting cables. Inst. Phys. Conf. Ser., 167, 2000.
- [31] *L. Bottura. Modelling stability in superconducting cables. Physica C, 310, 1998.*
- [32] L. Bottura, M. Breschi, M. Schneider. Measurements of Magnetic Field Pattern in a Short LHC Dipole Model. Paper 1LH01, Presented at ASC 2000, Virginia Beach, September 2000.
- [33] L. Bottura, L. Walckiers and Z. Ang, "Experimental Evidence of Boundary Induced Coupling Currents in LHC Prototypes." Presented at 1996 Appl. Sup. Conf., Pittsburgh.
- [34] M. Haverkamp, L. Bottura, M. Schneider, "Studies of Decay and Snapback Effects on LHC Dipole Magnets." Proceedings EUCAS 99, Sitges, Spain 1999.
- [35] M. J. Lamm, M. Bleadon, K. I. Coulter, S. Delehamps, R. Hanfl, T. S. Jaffery, W. Kinney, W. Koska, J. P. Ozelis, J. Strait, M. Wake, J. DiMarco, IEEE Trans. Magn., 28, 1992.
- [36] M. Polak, L. Krempasky, I. Hlasnik, J. Perot, "Losses in 23 strands NbTi and Nb₃Sn flat cables", IEEE Trans. Magn., 17 (5), 1981.
- [37] V. E. Sytnikov, G. G. Svalov, S. G. Akopov, I. B. Peshkov, "Coupling losses in superconducting transposed conductors located in changing magnetic fields", Cryogenics 29, 1989.
- [38] A. Nijhuis, H. G. Knoopers, B. ten Haken, H. H. J. ten Kate, "Model Study on AC Loss and Current Distribution in a Superconducting Multi Strand Cable", Report UT-NET 2000-1. Faculty of Applied Physics, University of Twente, January 2000.
- [39] C. Meinecke, A. Miri, R. Petranovic, "Numerical Investigation of the Current Distribution in Cable in Conduit Conductors Using Lumped Network Models", presented at Applied Superconductivity Conference, ASC 2000, Virginia Beach, USA, September 2000.
- [40] K. P. Juengst and the Wendelstein 7-X Technical Group, "Superconducting model coil for the stella rator W 7-X under test", IEEE Trans. Magn., 32 (4), 1996.
- [41] F. Bellina, M. Ghin, "Analysis of the joints between superconducting cables of the ITER CS coils", Report Consorzio RFX, Padova, April, 1998.
- [42] W. J. Carr, AC loss and Macroscopic Theory of Superconductors, Gordon and Breach, New York, USA, 1983.
- [43] W. J. Carr, "AC loss in a multifilamentary superconducting wire", J. Appl. Phys. 45 (2), 1974.
- [44] W. J. Carr, V. T. Kovachev, "Interstrand eddy current losses in Rutherford cable", Cryogenics 35, 1995.

- [45] V. Vysotsky, K. Funaki, M. Takeo, "Current distribution in multistrand superconducting cables-experimental methods of study and results received", Presented at ICMC'98, University of Twente, Netherlands, 1998.
- [46] V. Vysotsky, M. Takayasu, S. Jeong, P. C. Michael, J. Schultz, J. V. Minervini, "Measurements of current distribution in a 12-strand Nb₃Sn cable in conduit conductor", *Cryogenics* 37, 1997.
- [47] V. Vysotsky, M. Takayasu, P. C. Michael, J. Schultz, J. V. Minervini, S. Jeong, "Current Distribution in a 12 Strand Nb₃Sn CICC and its Influence on Ramp Rate Limitation", *IEEE Trans. Appl. Sup.* 7 (2), 1997.
- [48] S. Kim, K. Nam, S. Jeong, "Current Measurements of the Individual Strands in CICC Magnet", *IEEE Trans. Appl. Sup.*, 1999.
- [49] N. Amemiya, O. Tsukamoto, "Stability Analysis of Multi Strand Superconducting Cables", *IEEE Trans. Appl. Sup.* 5, (2), 1995.
- [50] N. Amemiya, H. Yonekawa, N. Tsuchioka, O. Tsukamoto, "Experimental study on Current Re-Distribution and Stability of Multi-Strand Superconducting Cables", *IEEE Trans. Appl. Sup.* 7, (2), 1997.
- [51] N. Amemiya, H. Yonekawa, T. Ogitsu, E. Kobayashi, K. Sasaki, N. Ohuchi, K. Tsuchiya, K. Miyashita, "Influence of current re-distribution on minimum quench energy of superconducting triplex cable against local disturbance", *Cryogenics* 38, 1998.
- [52] T. Yoshino, M. Tsuda, A. Ishiyama, "Improvement of Transient Stability of Non-insulated AC Multi-strand Superconducting Cables", *IEEE Trans. Appl. Sup.* 7, (2), 1997.
- [53] A. Ishiyama et al., "Effect of Cu-sheath on transient stability of AC multistrand superconducting cables", presented at MT-15, Beijing, 1997.
- [54] A. Ishiyama, M. Sasaki, T. Susa, S.B. Kim, M. Tsuda, "Transient stability of AC Multi-strand Superconducting Cables", presented at ICMC'98, Twente, Netherlands.
- [55] A. Ninomiya, S. Sekine, T. Ishigohka, S. Yamaguchi, "Experimental Investigation on Current Imbalance of Stranded Conductors", *IEEE Trans. Appl. Sup.*, 9, (2), 1999.
- [56] T. Ishigohka, A. Ninomiya, S. Yamaguchi, I. Nomura, T. Sato, S. Hanai, Y Hasegawa, H. Okumura, R. Shimada, "Effect of Impedance Distributions on Current Imbalance in Insulated Multistranded Superconducting Conductor", Presented at MT-16, Florida, U.S.A, 1999.
- [57] S. Kawabata, D. Terashi, K. Miyata, "Current distribution in Multi-Strand Superconducting Cables for AC Use in Both Steady and Transient States", Presented at MT 16, Florida, 1999.
- [58] T. Mito, K. Takahata, A. Iwamoto, R. Maekawa, N. Yanagi, T. Satow, O. Motojima, J. Yamamoto, F. Sumiyoshi, S. Kawabata, N. Hirano, "Extra AC losses for a CICC coil due to the non-uniform current distribution in the cable", *Cryogenics* 38, 1998.
- [59] N. Mitchell, "Non uniform Current Diffusion in Super and Normal Conducting Cables", Presented at CHATS 2000, Frascati, Italy, September 2000.
- [60] M. D. Sumption, R. M. Scanlan, E. W. Collings, "Coupling Current Control in Rutherford Cables wound with NbTi, Nb₃Sn, and Bi:2212/Ag", Presented at ICMC'98, University of Twente, Netherlands, 1998.
- [61] *A. Devred, L. Bacquart, P. Bredy, C. E. Bruzek, Y. Laumond, R. Otmani, T. Schild, "Interstrand Resistance Measurements on Nb₃Sn Rutherford-Type Cables", IEEE Trans. Appl. Sup., 9, 1999.*
- [62] *G. Ries, "Stability in superconducting multistrand cables", Cryogenics, 1980.*
- [63] *I.S. Gradshteyn, I.M. Ryzhik, Tables of Integrals, Series, and Products, Academic Press, London, 1980.*

- [64] A. Devred, T. Ogitsu, " Ramp Rate Sensitivity of SSC Magnets", Frontiers of Accelerator Technologies, World Scientific, 1996.
- [65] L. Bottura, M. Breschi, M. Fabbri, "Analytical solutions for current distribution in Rutherford cables", submitted for publication.
- [66] J. Buckley et al., "Dynamic Magnetic Measurements of Superconducting Magnets for the LHC," *IEEE Trans. Appl. Sup.*, 5 (2), 1995.
- [67] R. Stiening, "A Possible Mechanism for Enhanced Persistent Current Sextupole Decay in SSC Dipoles," SSCL-359, 1991, unpublished.
- [68] M. Schneider, "Decay and Snapback Studies on the LHC Dipole Model Magnets A Scaling Law," Ph. D. Thesis, TU Wien, 1998.
- [69] S. Russenschuck, Procs. of the First Int. ROXIE users meeting, ed., Cern Report 99-01, Geneva, 1999.
- [70] N. K. Madsen, R. F. Sincovec, *ACM Trans. on Mathematical Software*, 5, 1979.
- [71] M. Fabbri, P. L. Ribani, "Error Estimations on Potentials, Fields and Energies Evaluated with a Modified Kernel", Internal Report, DIE Bologna, Italy, October 2000.
- [72] M. N. Wilson, R. Wolf, "Calculation of Minimum Quench Energies in Rutherford Cables", *IEEE Trans. Appl. Sup.*, 7 (2), 1997.
- [73] B. Turck, "Influence of a transverse conductance on current sharing in a two-layer superconducting cable", *Cryogenics*, 1974.
- [74] L. Bottura, C. Rosso, M. Breschi, "A General Model for Thermal, Hydraulic and Electric Analysis of Superconducting Cables", *Cryogenics* 40, 2000.

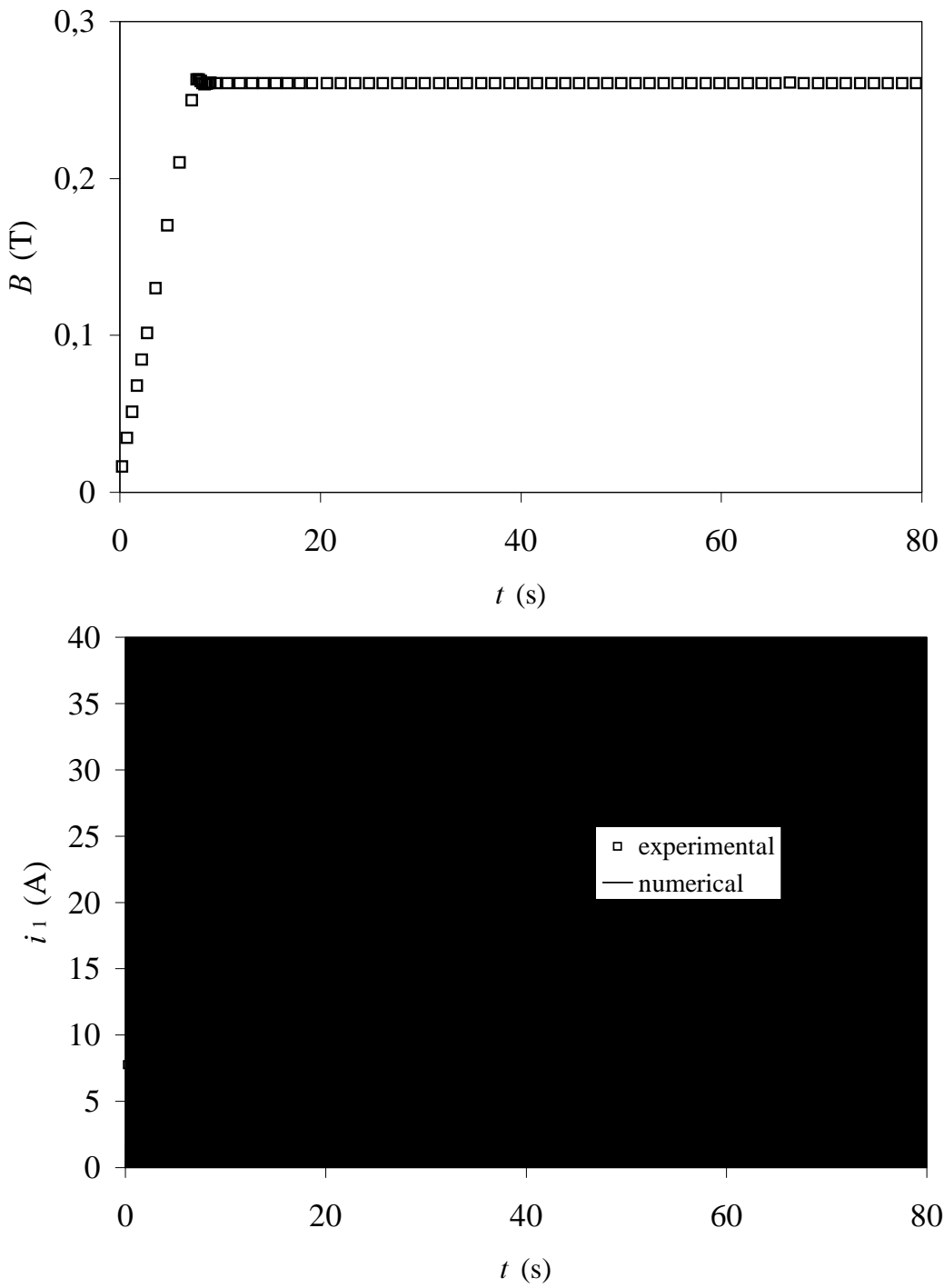


Fig. 5.1 Currents induced in a two strand cable a) Field sweep b) Comparison between experimental data and simulations with the distributed parameters model.

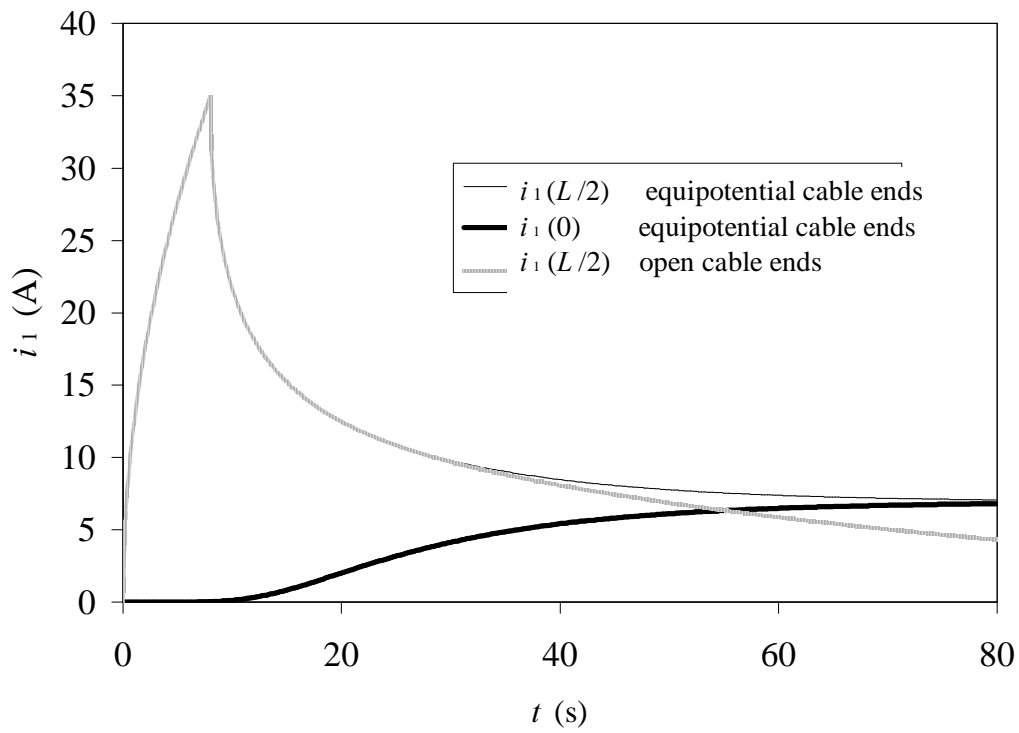
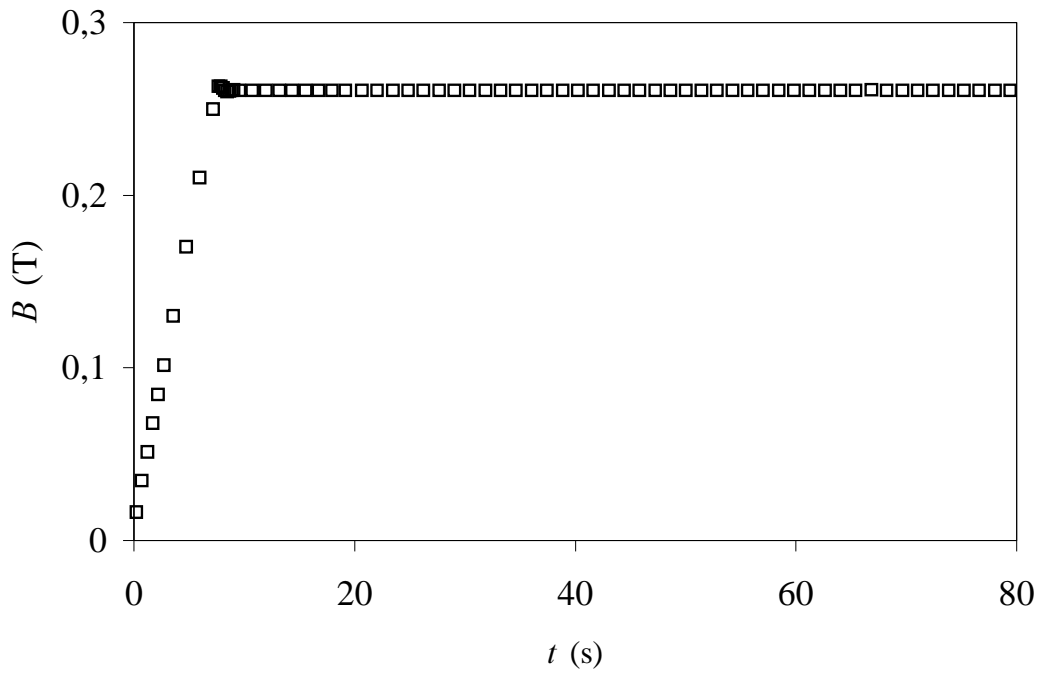
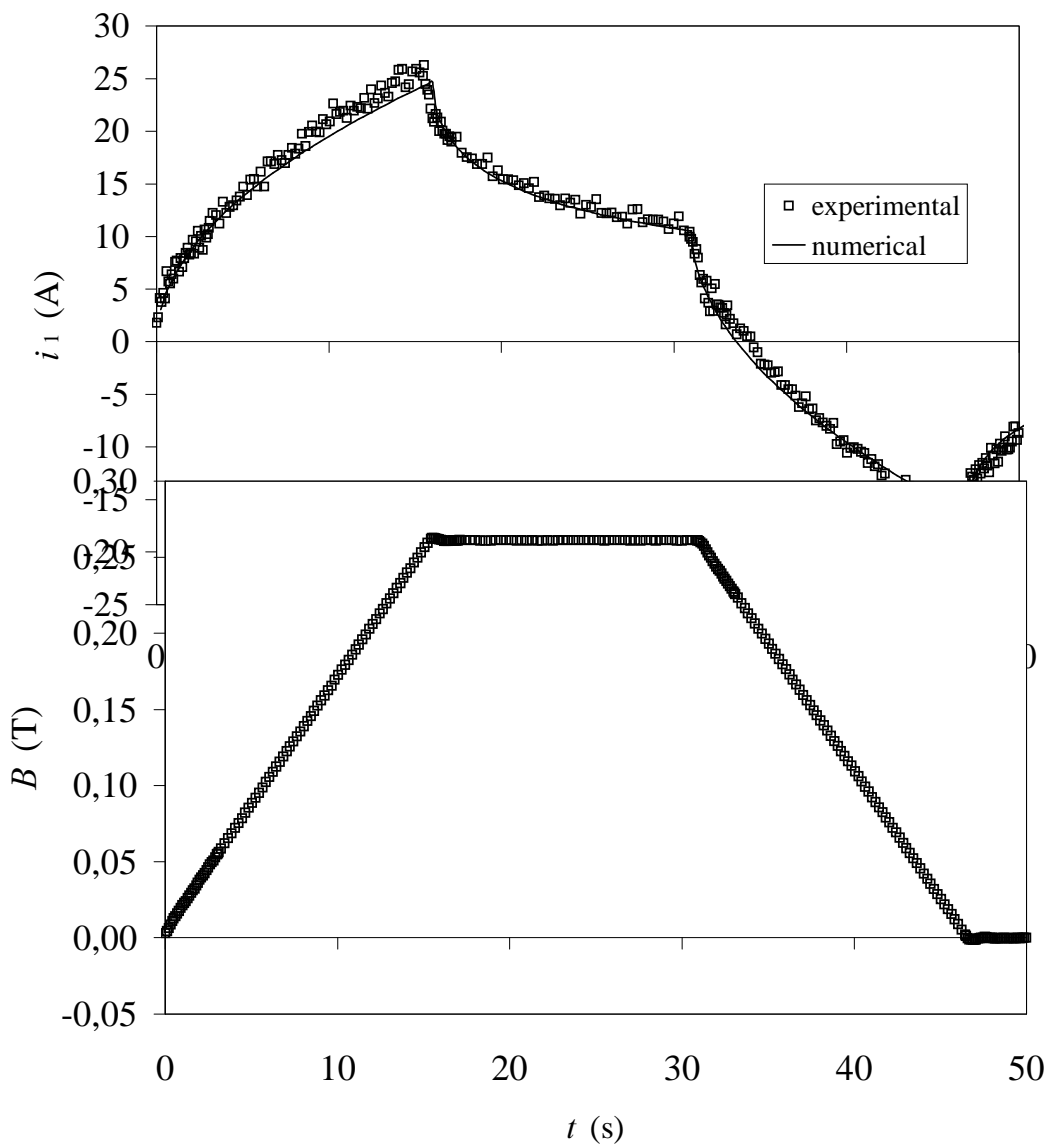


Fig. 5.2 Currents induced in a two strand cable a) External field sweep b) Comparison between different boundary conditions.

Fig. 5.3 Currents induced in a two strand cable a) Field sweep b) Comparison between experimental data and simulations with the distributed parameters model.



5.2 MEASUREMENTS OF MAGNETIC FIELD PATTERN IN A SHORT LHC DIPOLE MODEL

5.2.1 Introduction

As anticipated in Section 2.2.2, local field measurements in superconducting accelerator magnets have revealed a modulation with longitudinal periodicity on all harmonic components. Such periodicity has been measured on long models of the Large Hadron Collider (LHC) dipoles [33, 66]. In particular, systematic measurements have been performed in two 10-m long LHC model dipoles to explore the dependence of the periodicity on longitudinal position and time [33].

The main motivation for the experimental work in this field is the idea that the strand magnetization can be affected by internal field changes in the cable associated with the current redistribution, a phenomenon visible when the transport current is held constant [34, 68]. This effect causes a drift of the field in the magnet at constant operating current, and must be known and corrected for accelerator operation especially during the particle injection phases and the initial stage of the energy ramp. As anticipated in Section 2.2.2, the internal field changes causing the field drift at injection can be explained in terms of a diffusion of a current difference among strands in a cable. A current difference among strands in the cable in turn generates spatial variations of the field in the magnet bore, with a periodicity equal to the cable twist pitch. Given the relation between cable current distribution, field periodicity and field drift, it should be possible in last analysis to establish a correlation between the measured periodic pattern and the measured field decay.

In order to examine this possibility, we have measured extensively a short LHC model, MBSMT1, using an array of short rotating coils. We give in the following the detail on the measurement procedure and main results of this measurement. We concentrate on the results relative to the normal sextupole and normal decapole components of the multipole expansion of the magnetic field (see Equation 1.4), as they are the first allowed harmonics in the geometric configuration of the dipole [6].

5.2.2 *Experimental set up*

The measurements of the dipole model magnet MBSMT1 have been performed in a vertical test set-up, shown in Fig. 5.4. The magnet is suspended inside the cryostat. A λ -plate separates the pool boiling helium bath from the superfluid bath, both at atmospheric pressure (Claudet bath). The subcooled superfluid state in the lower portion of the cryostat is achieved by means of a heat exchanger, where saturated superfluid helium conditions are obtained via Joule-Thomson expansion of liquid helium from 1 bar down to approximately 15 mbar. The λ -plate has a number of leak-tight feed-throughs for superconducting bus-bars, instrumentation wires and a sliding bearing for the rotating shaft used for the magnetic measurements described below.

5.2.3 *Measurements of the magnetic flux density*

The measurement of the field and its harmonic components has been performed using radial coil arrays mounted on a glass-fibre shaft rotating in the bore of the magnet (see Fig. 5.5). Three arrays of coils, each composed of five adjacent coils sections, are installed to measure the field dependence along the magnet bore. Each coil is 25 mm long, so that each coil group covers approximately 125 mm. The top group is placed with the topmost coil at the beginning of the straight region at the layer jump, (connection end). The center group is placed with its topmost coil in the center of the magnet. The bottom group is placed with the bottom coil at the end of the straight part in the opposite-connection end. The coils rotate in the superfluid helium bath. The shaft axis is held at four places: by bearings at both ends of the magnet, a sliding bearing to intercept heat conduction across the λ -plate, and a pressure-tight bearing in the cryostat top flange.

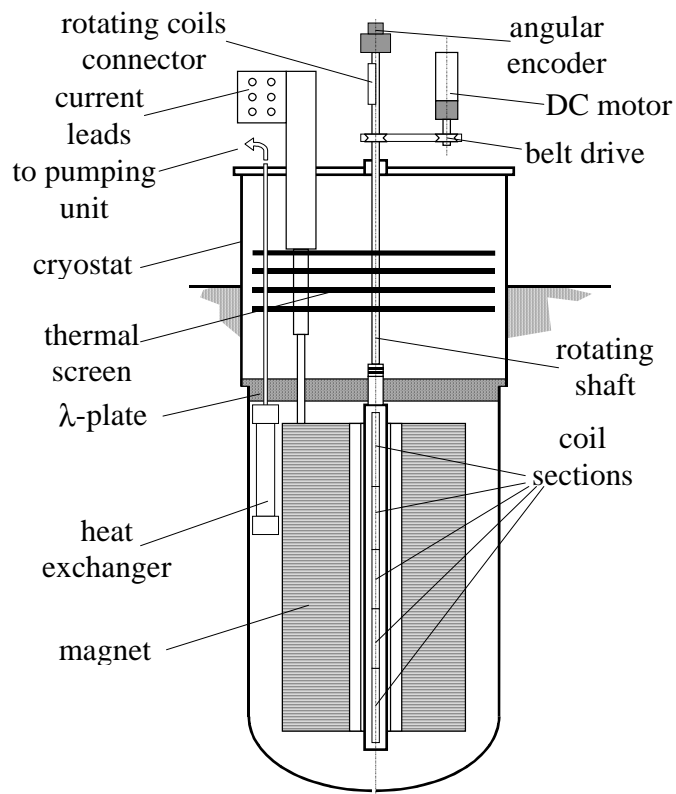


Fig. 5.4 Schematic view of the vertical test set-up for the dipole model magnets
(shown for a single aperture model).

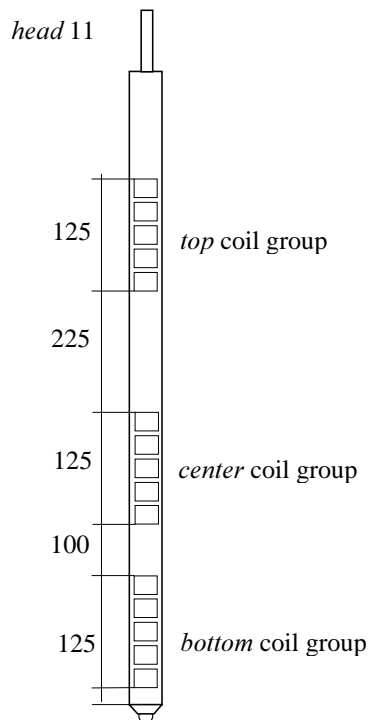


Fig. 5.5 Sketch of the rotating coil shaft showing the three arrays of five adjacent coils.

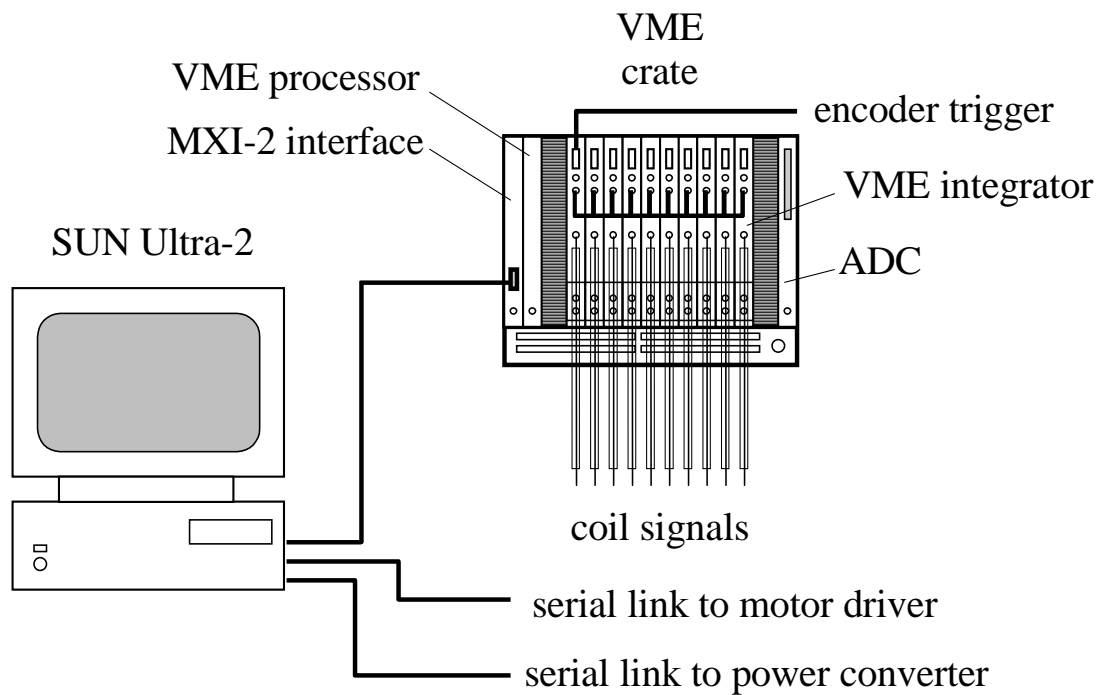


Fig. 5.6 Block diagram of the magnetic field measurement system.

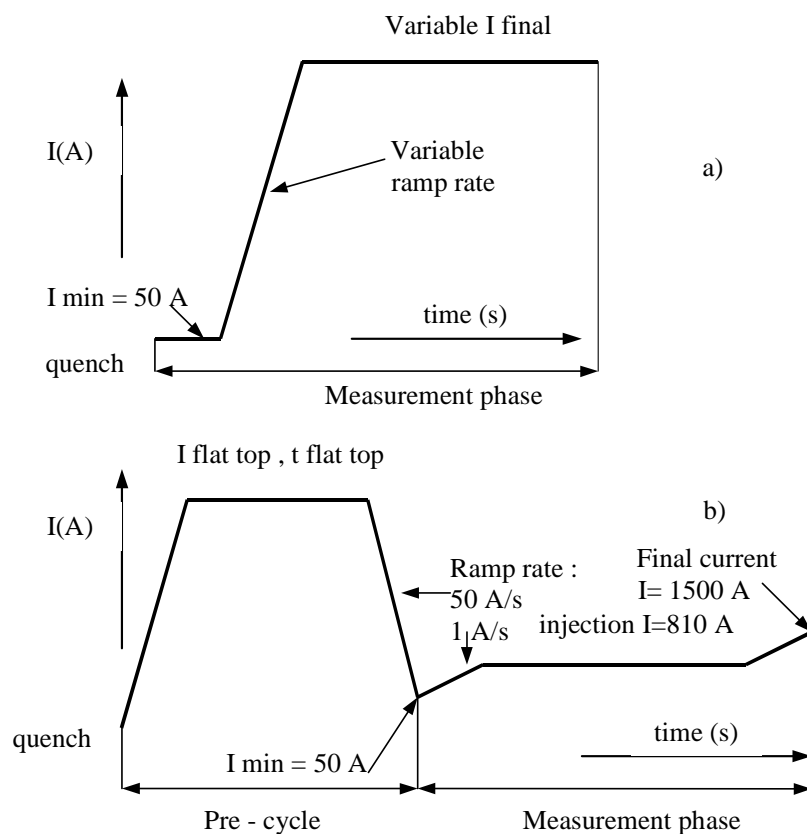


Fig. 5.7 a) Schematic diagram of step response measurements.

b) Schematic diagram of proposed operating current cycle for LHC.

The transitions from the magnet to the λ -plate and from cold to warm temperature are equipped with bellows, which are designed to be stiff with respect to torsion but allow axial misalignments. A DC motor mounted on the top flange of the cryostat drives the shaft via a belt transmission, while an encoder, rigidly mounted on the top end of the shaft, determines the angular position of the shaft. The rotation frequency is typically in the range of 1 Hz. Because of dead times between rotations, the time interval between two measurements is of the order of 20 s.

5.2.4 Acquisition system

Figure 5.6 shows a schematic of the acquisition system. The voltage signals from the five rotating coils sections are read-out simultaneously by precision integrators triggered by the angular encoder. The integrated voltages are thus equal to the flux changes through the measuring coil for all angular steps, and rotation velocity variations during the measurements are compensated up to the first order. A real-time processor configures the integrators and reads the integrated voltages. Integrators and processor are mounted on a VME-bus (Versa Module Europa, IEEE 1014-1987 standard). Overall control of the power supply, of the precision current reading, of the motor driving the shaft rotation and of the integrators is achieved using LabVIEW software running on a SUN Ultra-2 workstation.

5.2.5 Measurement cycles

Different kinds of measurement cycles were performed in order to obtain detailed information on the parameters influencing the generation and the development of the magnetic field pattern. The magnet was quenched before every cycle in order to erase the ‘memory’ of all induced currents.

In a first series of tests the magnet was ramped up in a single step from a small current to a flat top current, designated as I_{FT} , at varying ramp-rates RR. The analysis of simple step responses can provide useful qualitative and quantitative information about the magnetic pattern, and can be

directly compared with the measurements performed with the two strand cable. A characteristic current step is shown in Fig. 5.7a.

Several measurements were also performed following the proposed operating current cycle for LHC dipole magnets. The measurement cycles are shown in Fig. 5.7b. The measurements started after a pre-cycle consisting of a linear current increase up to a maximum value (flat top current), a constant current period (flat top), and a linear decrease of the current to 50 A. Both the current ramp-up and ramp-down rates were set to 50 A/s. The flat top current and the flat top time were separately varied throughout the experiments in order to explore their influence on the pattern generated. The measurement phase consisted of a linear increase of the operation current up to 810 A with a ramp rate of 1 A/s, a long constant current period (injection phase) and a final current ramp up to about 1500 A.

5.2.6 Data analysis

We will refer in the discussion to the harmonic components of the following complex expansion of the magnetic field in the magnet bore:

$$B_y + iB_x = \sum_{n=1}^{\infty} [B_n + iA_n] \left(\frac{\mathbf{s}}{R_0} \right)^{n-1} \quad (5.1)$$

where $\mathbf{s} = x + iy$ is the complex co-ordinate in the (x, y) coil cross sectional plane, R_0 is the reference radius for LHC (17 mm) and B_n and A_n are the multipole coefficients.

There are five working coils in the bottom and top coils array while only four are correctly working in the middle coils array. We indicate with N_{co} the total number of coils of a generic coils array. Each array provides a set of N_{co} values for every field harmonic up to the 15th component for every measurement. Each value is referred to a different position along the magnet bore axis; we indicate with z_i , ($i=1, N_{co}$) the positions along the magnet axis, and with h_{ni} the measured values of the harmonic h_n at position z_i .

The following expression is used to fit the experimental data and to find characteristic quantities describing the longitudinal field variations:

$$h_n = F_0 + F_1 z + A \sin \left(\frac{2\pi z}{L_p} + \varphi \right) \quad (5.2)$$

where z is the abscissa running along the magnet axis and F_0 , F_1 , A and φ are the fitting parameters. In particular F_0 is a constant offset, F_1 the slope of a linear term taking into account field gradients along the magnet axis, A the amplitude of the sinusoidal variation and φ its initial phase.

Finally, in order to evaluate the drift of the field harmonics during the constant current phases, we consider the arithmetic average of the measured values:

$$\bar{h}_n = \frac{\sum_{i=1}^N h_{ni}}{N} \quad (5.3)$$

5.2.7 Step response measurements

Several step response measurements have been performed with different ramp rates (ranging from 50 A/s to 200 A/s) and final flat top currents (ranging from 2000 A to 8000 A). A longitudinal variation of the field harmonics is found in every step response measurement.

Amplitude of the magnetic field pattern

measurements have been rates (ranging from 50 A/s to 200 A/s) and final flat top currents (ranging from 2000 A to 8000 A). A longitudinal variation of the field harmonics is found in every step response measurement.

These longitudinal variations have different features for the three positions along the magnet. At the top part of the magnet we observe a strong longitudinal gradient of the field harmonics, so that it is not possible to recognize a precise and repeatable pattern (see Fig. 5.8). This could be due to the end field deformation at the connection end.

In the middle and bottom parts of the magnet, however, the field harmonics exhibit an oscillation characterized by a period equal to the inner cable twist pitch, so that we can consider them as part of a periodic pattern. The measured values of the normal sextupole and normal decapole components are shown in Figs. 5.9 and 5.10 for the middle and the bottom part of the magnet respectively, after 100 s from the beginning of the flat top in the step response measurement with 2000 A of final current and 450 A/s of ramp rate.

The experimental data can be well fitted by equation (5.2).

Figure 5.11 shows the temporal evolution of the amplitude of the sextupole pattern calculated by means of the fitting function (5.2) in the case of a 450 A/s ramp rate and a 2000 A final current. The step response to a ramp with the same ramp rate (450 A/s), but higher final current (8000A) is shown in Fig. 5.12, while the responses to ramps with low ramp rate (50 A/s) are reported in Figs. 5.13 and 5.14 for a final current of 2000 A and 5000 A respectively.

A typical feature is always exhibited by the pattern amplitude of the sextupole component: it is about null before the current ramp, then quickly increases during the ramping up, and finally decays when the flat top is reached. We observe that this behavior is very similar to that shown

by the amplitude of the “supercurrents” induced by a flux density variation in a loop between two strands measured in the experiments performed by Krempasky and Schmidt (see Fig. 5.1). In [12] the experimental results were compared with the analytic solution of the equation of diffusion of the supercurrents (4.41). From (4.42) it can be shown that the following equation holds locally for the diffusion of the supercurrent during its decay after the field ramp:

$$i_1(t) = \sum_{n \text{ uneven}}^{\infty} I_n \left(1 - e^{-\frac{t_1}{\tau_n}} \right) e^{-\frac{(t-t_1)}{\tau_n}} \quad (5.4)$$

for $t > t_1$, where t_1 is the time at which the flat top is reached, τ_n is the decay time constant of each component of the infinite sum and I_n its amplitude. In particular I_n is a function of the driving voltage of the loop, the transverse conductance between the two strands and the length of the cable (see 4.42).

Given the relation between the amplitude of the supercurrents flowing in the cable and the sinusoidal oscillations of the field harmonics, we plot in Figs. 8c-11c the logarithm of the amplitude of these oscillations, in order to explore the nature of their decay. After an initial phase where we can suppose the superposition of different time constants, the logarithmic plot can be approximated through a straight line with the slope of the longest time constant. Fitting the logarithmic plot with a straight line, we have found the slope of the linear fit to be dependent on the initial time chosen for fitting, obtaining higher time constants with a higher initial time. This is due to the relatively short measurement time (1000 s), after which the system has not yet reached its final exponential decay with the longest time constant. An underestimate of this time constant leads to a range of 3000 to 4500 s.

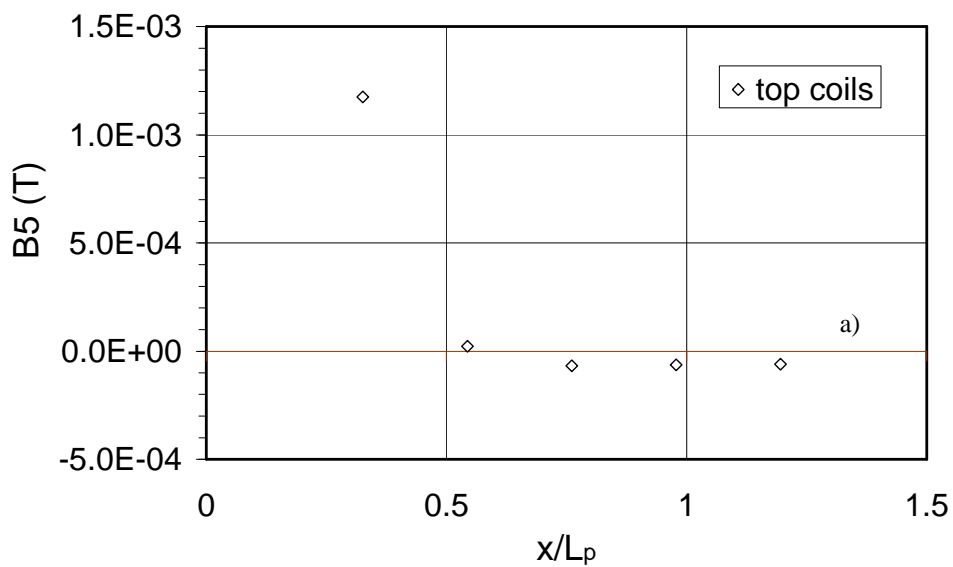
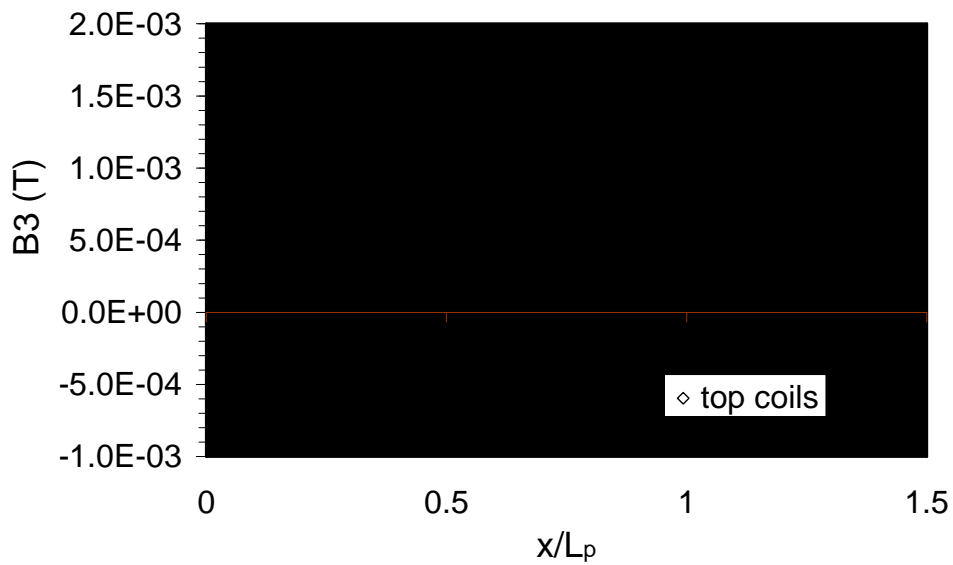


Fig. 5.8 Longitudinal variations of the sextupole (a) and decapole (b) components at the top position of the magnet. The values are referred to the



step response measurement with $I_{FT} = 2000$ A, $RR = 450$ A/s, after 100 s from the beginning of the flat top.

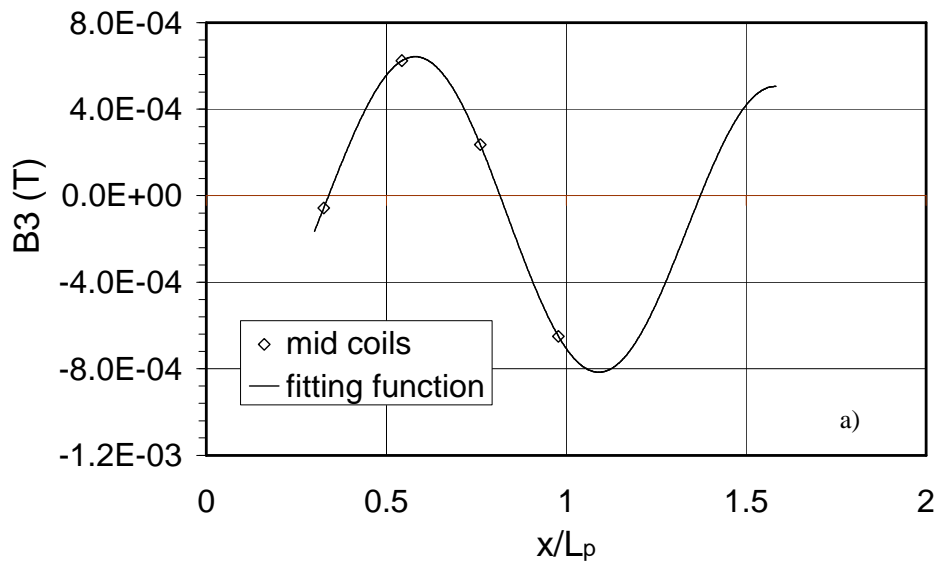
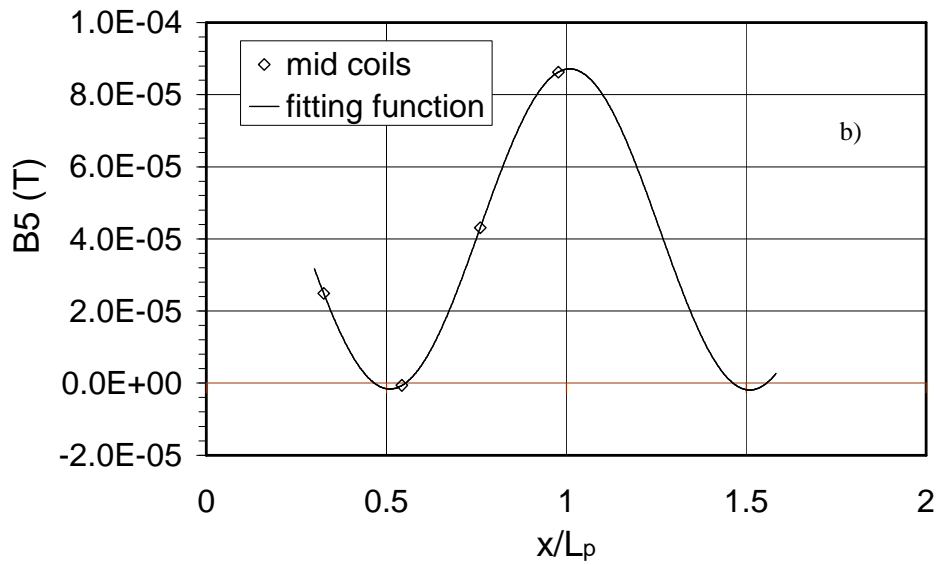


Fig. 5.9 Longitudinal variations of the sextupole (a) and decapole (b) components at the middle position of the magnet. The fitting function is



calculated by means of equation (5.2). The values are referred to the step response measurement with $I_{FT} = 2000$ A, $RR = 450$ A/s, after 100 s from the beginning of the flat top.

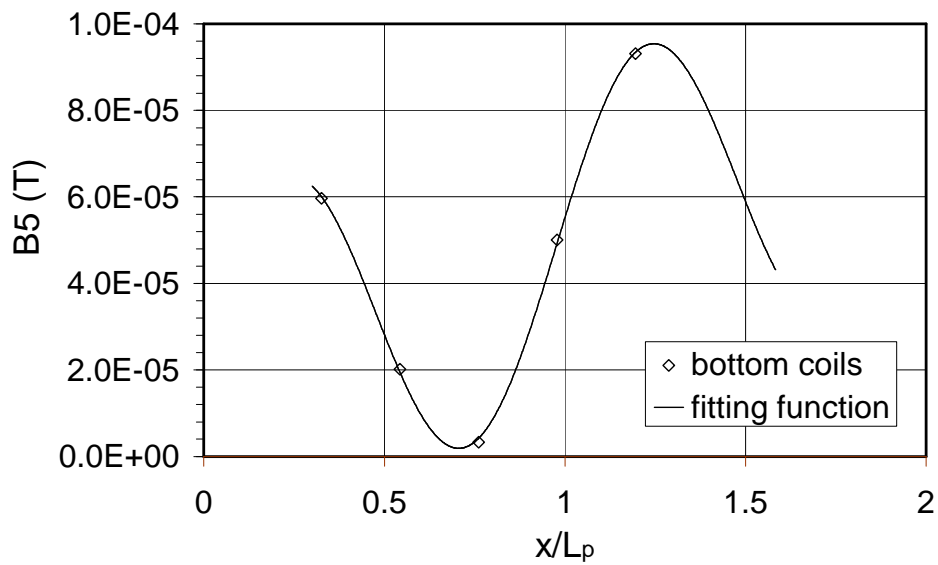
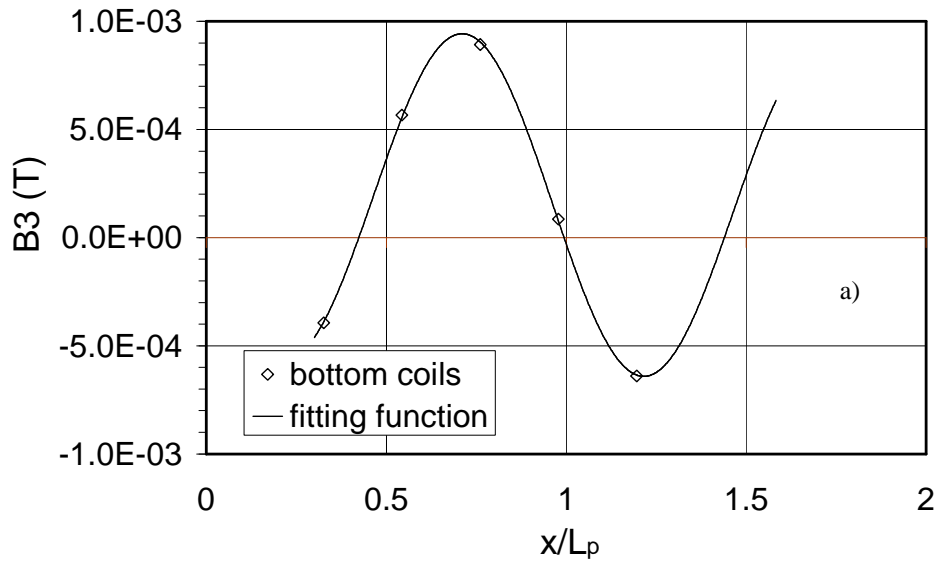


Fig 5.10 Longitudinal variations of the sextupole (a) and decapole (b) components at the bottom position of the magnet. The fitting function is calculated by means of equation (5.2). The values are referred to the step response measurement with $I_{FT} = 2000$ A, $RR = 450$ A/s, after 100 s from the beginning of the flat top.

b)

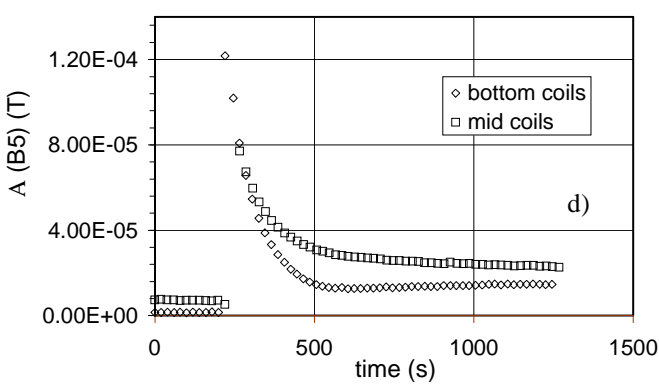
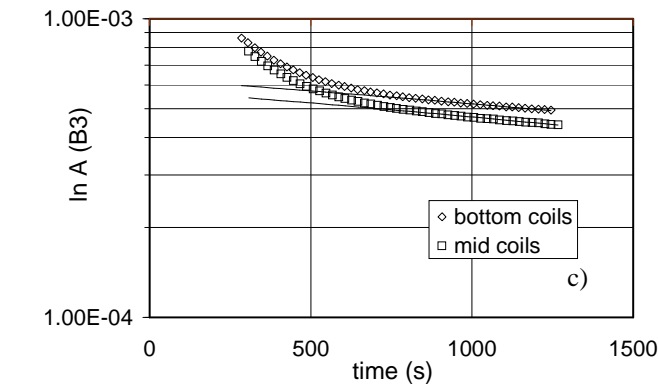
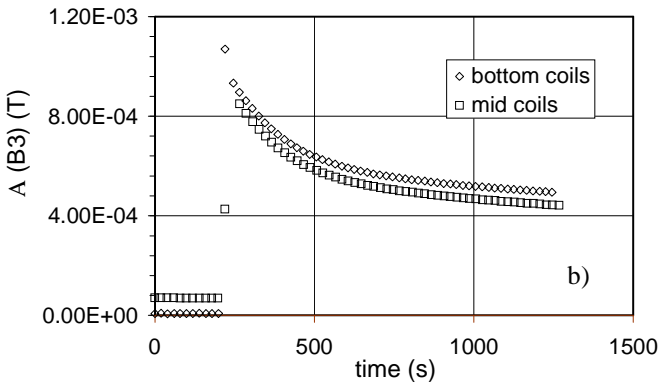
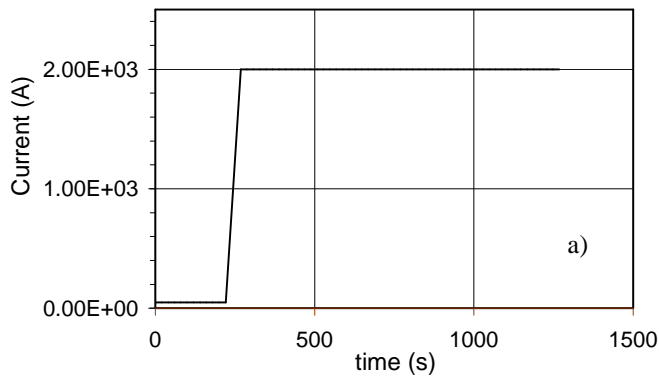


Fig. 5.11 a) Current ramp (450 A/s ramp rate and 2000 A final current). b) Amplitude variation versus time (B3). c) Logarithmic plot (B3). d) Amplitude variation versus time (B5).

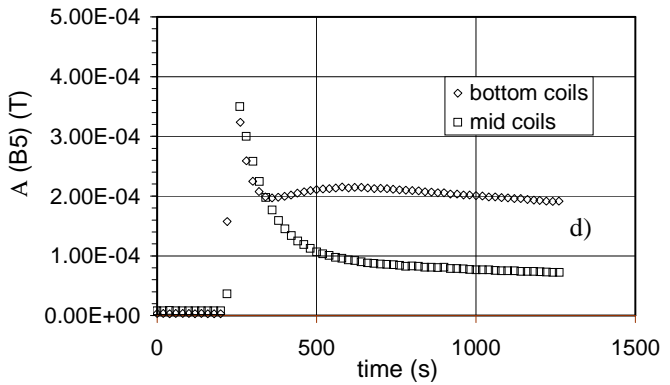
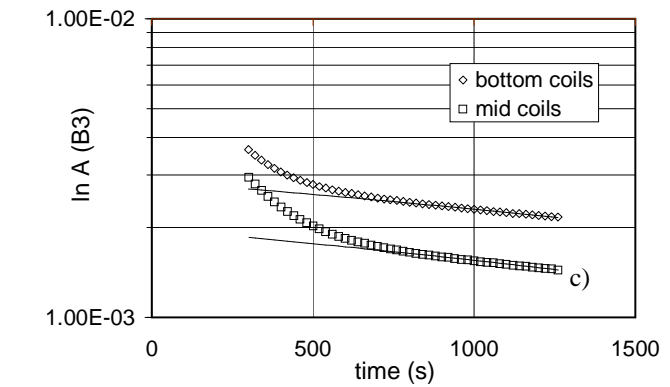
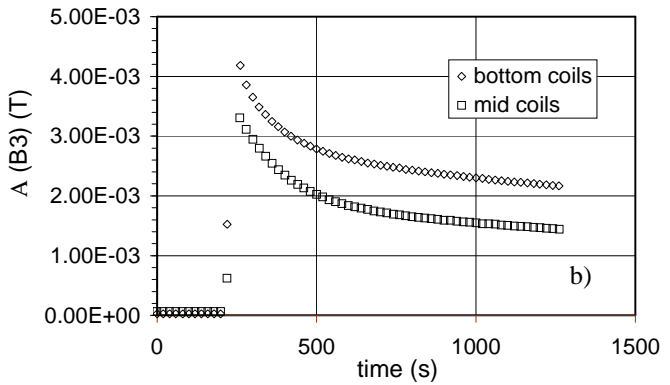
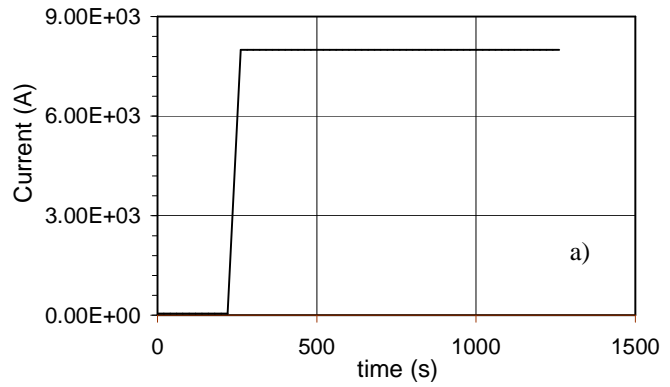


Fig. 5.12 a) Current ramp (450 A/s ramp rate and 8000 A final current). b) Amplitude variation versus time (B3). c) Logarithmic plot (B3). d) Amplitude variation versus time (B5).

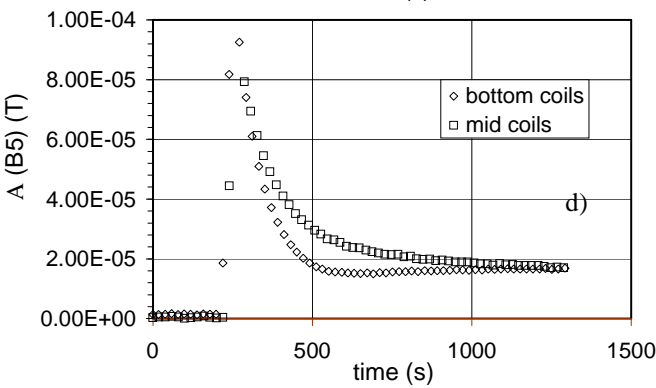
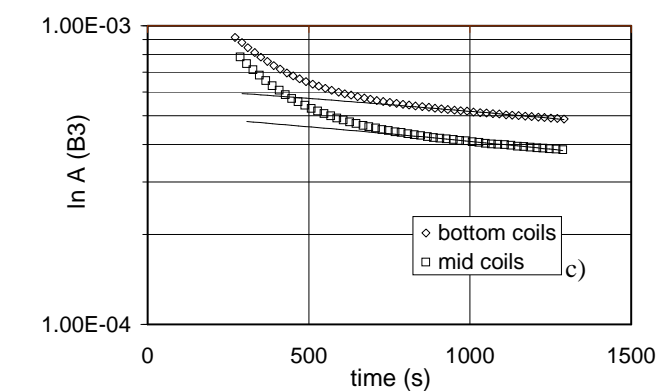
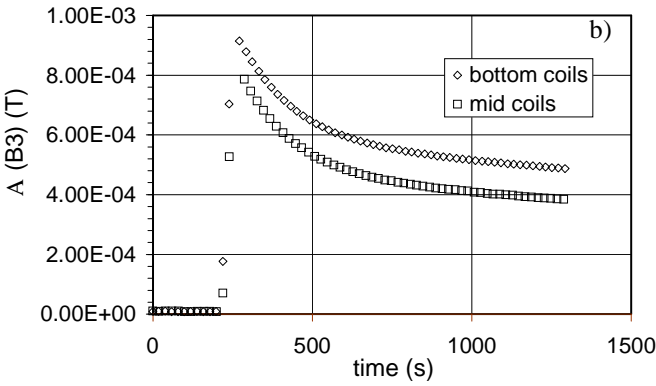
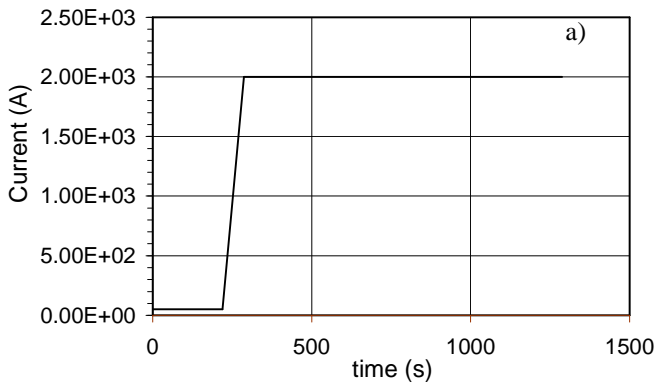


Fig. 5.13 a) Current ramp (50 A/s ramp rate and 2000 A final current). b) Amplitude variation versus time (B3). c) Logarithmic plot (B3). d) Amplitude variation versus time (B5).

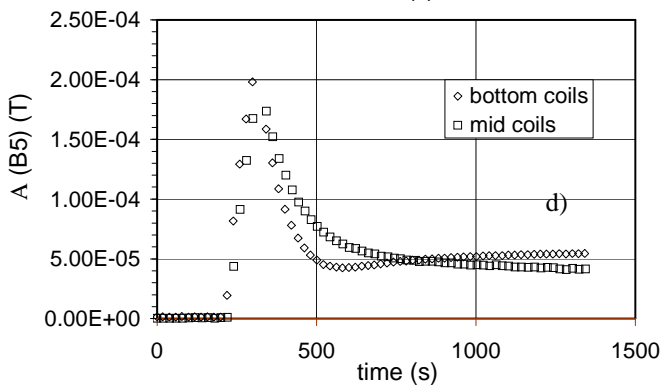
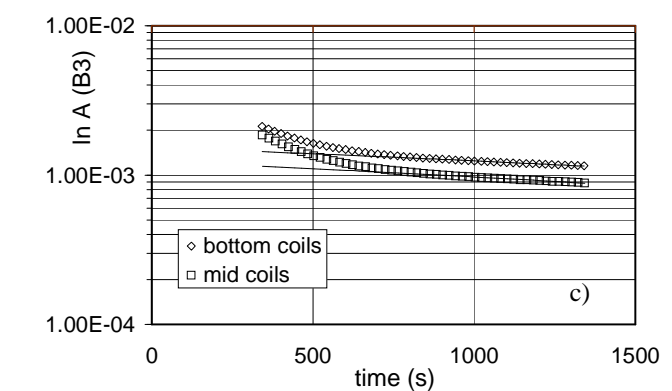
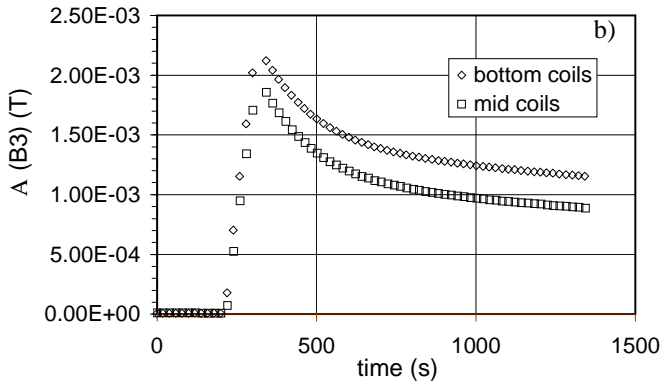
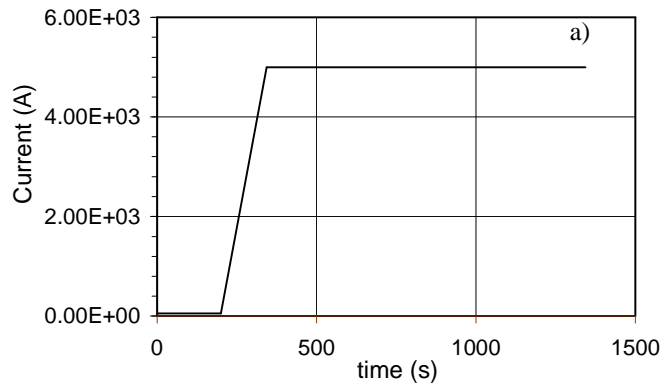


Fig. 5.14 a) Current ramp (50 A/s ramp rate and 5000 A final current). b) Amplitude variation versus time (B3). c) Logarithmic plot (B3). d) Amplitude variation versus time (B5).

In all measurements, the amplitude in correspondence of the middle coils is lower than that in the bottom part. This may be due to the greater distance of the central coils from the origin of the BICCs, which are one of the sources of the development of the field harmonics periodic pattern. The BICCs are mainly generated by longitudinal variations of the time derivative of the magnetic flux density perpendicular to the broad face of the cable, which are more pronounced at the magnet ends due to the cable bending over the magnet bore.

The step responses of the pattern amplitude of the normal decapole component are reported in Figs. 5.11d-5.14d. The amplitude of the normal decapole pattern at the central position of the magnet shows a variation in time similar to that of the amplitude of the normal sextupole pattern, while a different kind of decay is sometimes shown by the measurements at the bottom position of the magnet (see for example the case of bottom coils in Figs. 5.11d and 5.12d). The absolute values of the amplitude of the decapole component are about one order of magnitude lower than the corresponding values of the sextupole component.

Comparing Figs. 5.11b and 5.12b we note that the amplitude of the sextupole pattern at the beginning of the constant current phase is higher in the case of higher flat top current. The same observation can be made for the decapole component comparing Fig. 5.11d to Fig. 5.12d. In order to investigate better this dependence, we plot in Fig. 5.15 the sextupole pattern amplitude at the beginning of the current flat top as a function of the flat top current for different values of the ramp rate. The same plot in the case of the decapole pattern is shown in Fig. 5.16. We observe a linear dependence of the initial amplitude on the final current in the case of high ramp rates (450 A/s and 200 A/s). The linear fit is very good in particular in the case of mid coil measurements.

The dependence of the amplitude at the beginning of the constant current phase on the ramp rate is shown in Figs. 5.17 and 5.18 for the sextupole and the decapole pattern respectively. The amplitude is independent of the ramp rate at low flat top current (Figs. 5.17a and 5.18a), while it slightly increases with the ramp rate for high flat top currents (Figs. 5.17c and 5.18c).

In order to compare the size of the amplitude decay of the sextupole pattern in different measurements, we consider the pattern amplitude variation after 1000 s from the beginning of the decay:

$$\delta A = A(t_f + 1000 \text{ s}) - A(t_f) \quad (5.5)$$

where t_f is the time at which the current plateau is reached.

This parameter depends linearly on the final current for all ramp rates, while it is approximately independent of the current ramp rate. This is expected, as the maximum amplitude reached after the ramp is linearly dependent on the final current and independent of the ramp rate and the decay time constants in different measurements are very similar.

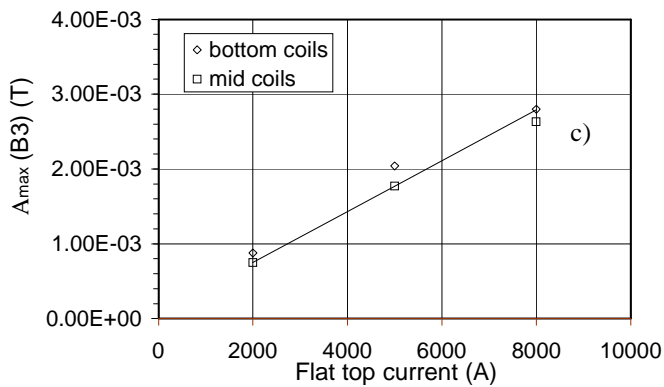
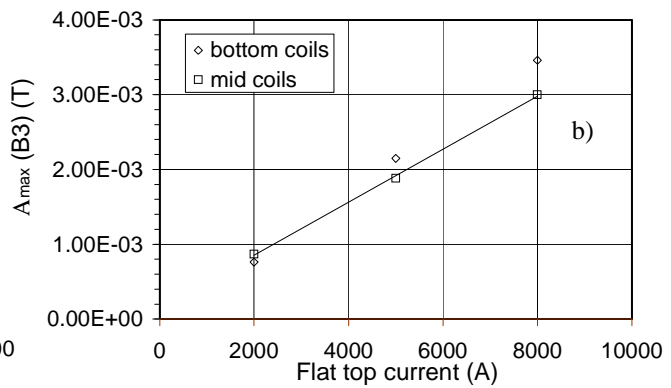
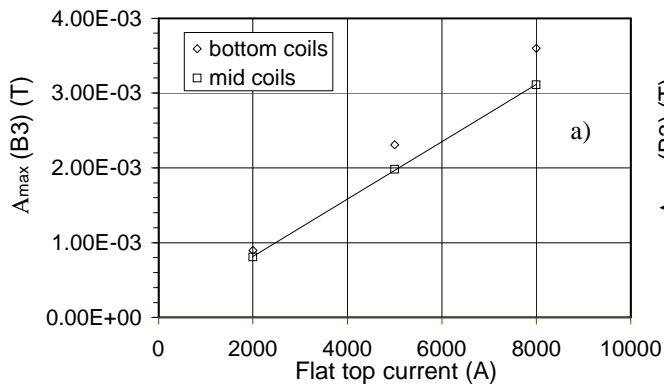


Fig. 5.15 Dependence of the amplitude of the normal sextupole pattern at the beginning of the flat top on the final current of the ramp. a) $RR = 450 A/s$ b) $RR = 200 A/s$ c) $RR = 50 A/s$

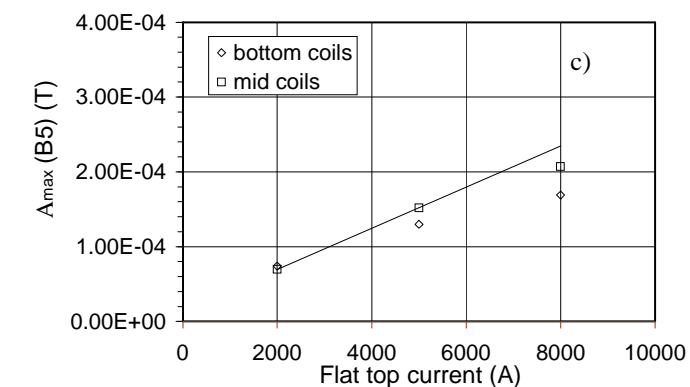
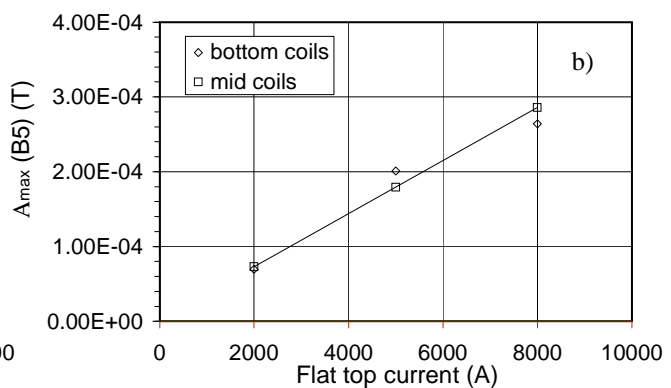
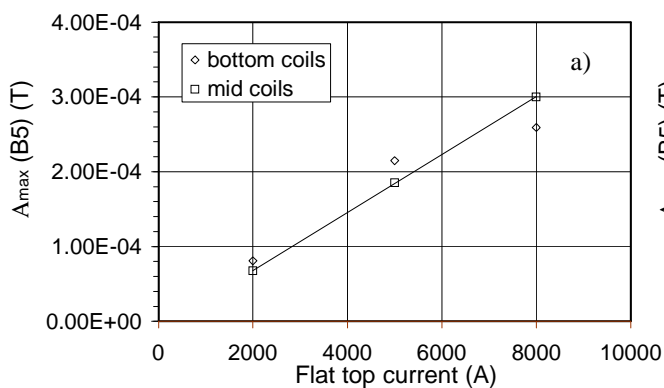


Fig. 5.16 Dependence of the amplitude of the normal decapole pattern at the beginning of the flat top on the final current of the ramp. a) $RR = 450 A/s$ b) $RR = 200 A/s$ c) $RR = 50 A/s$

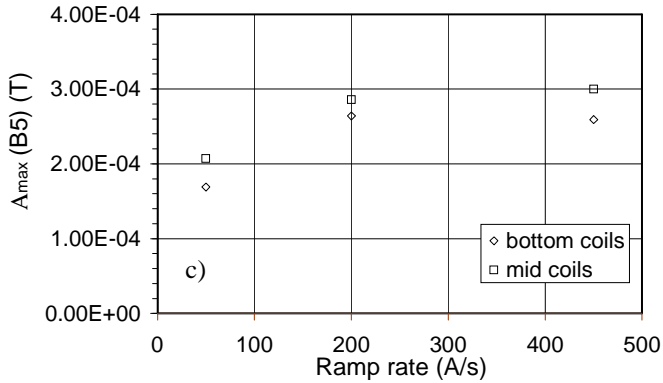
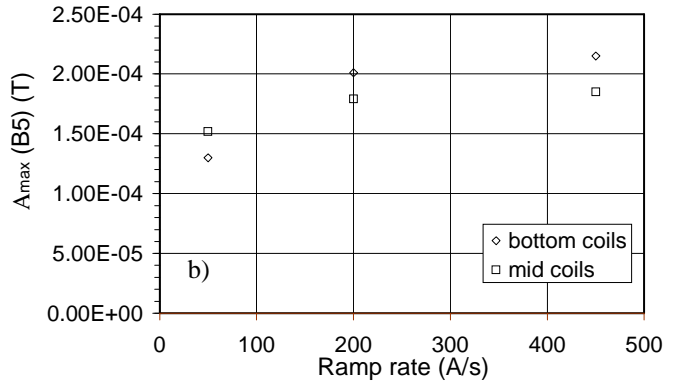
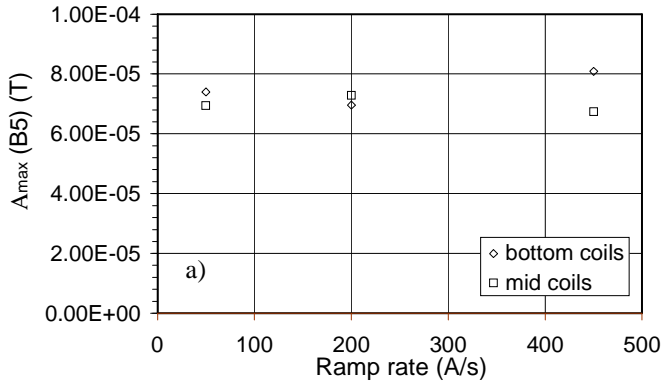
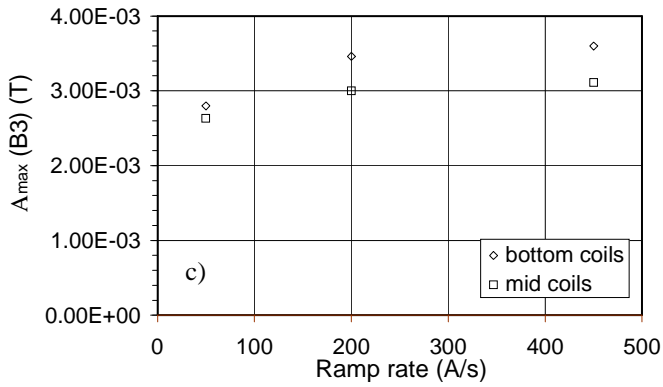
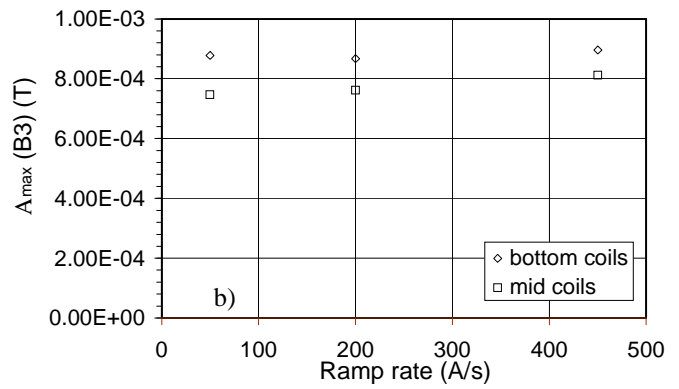
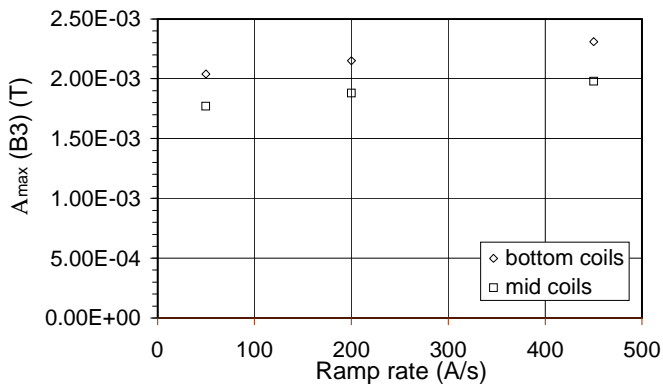


Fig. 5.18 Dependence of the amplitude of the normal decapole pattern at the beginning of the flat top on the ramp rate of the ramp.

a) $I_{FT} = 2000 A$ b) $I_{FT} = 5000 A$
 c) $I_{FT} = 8000 A$

Fig. 5.17 Dependence of the amplitude of the normal sextupole pattern at the beginning of the flat top on the ramp rate of the ramp. a) $I_{FT} = 2000 A$ b) $I_{FT} = 5000 A$ c) $I_{FT} = 8000 A$

The temporal Average value of the field harmonics evolution of the average harmonics over the two coil groups mid and bottom [see definition (5.3)] is shown in Fig. 5.19 for the step response measurement with a 2000 A flat top current and a 450 A/s ramp rate and in Fig. 5.20 for the step response measurement with 8000 A flat top current and 450 A/s ramp rate. The variation in time is different for the two positions in the magnet, but each kind of pattern is repeated in different experiments.

The average in the mid coil measurements always decreases during the constant current phase, while in the bottom coil measurements it always increases. The variation of the average value after 1000 s from the beginning of the flat top phase has been taken as a parameter to compare different experiments. The plot of this parameter versus the flat top current and the ramp rate is shown in Figs. 5.21 and 5.22 respectively.

In the case of the mid coil measurements we can observe that the variation of the average is approximately linear with the final current, and constant with the ramp rate.

Phase of the modulation

The variation in time of the phase φ of the normal sextupole pattern is shown in Figs. 5.23 and 5.24 for the same measurements reported in Figs. 5.19 and 5.20. We have found the same kind of phase variation in every measurement. We observe that the maximum change of the phase of the sinusoidal fit of the measured data is approximately equal to 0.1 radians during a total time of 1000 s. The phase shift of the sinusoidal pattern is equivalent to a translational movement of the pattern along the magnet axis. The average linear velocity of this translation can be calculated as follows:

$$v_t = \frac{\Delta\varphi}{\Delta t} \cdot \frac{L_p}{2\pi} \quad (5.6)$$

where v_t is the translational velocity and $\Delta\varphi$ the total phase variation.

We obtain an average velocity of about $1.8 \cdot 10^{-6}$ m/s, equivalent to 6.6 mm/h. This value is negligible, also considering that in the final part of the decay the phase variation in time is slower than in the initial part.

Comparison between average and amplitude variations

Considering the measurements referred to the middle part of the magnet, we note that the same dependence on the final current and on the ramp rate is shown by the variation of the amplitude of the sextupole pattern after 1000 s of decay and by the variation of the average over the mid coil group in the same time interval. These variations are in fact linearly dependent on the final current and independent of the ramp rate. The variation of the average is in all cases in the range from 10 to 15% of the variation of the amplitude of the periodic pattern (see Fig. 5.25).

The variation of the average could be due to the mismatch between the total length covered by the measurement coils and the inner cable twist pitch. The integral of the sinusoidal variation over this region contributes to the determination of the average value and depends linearly on the value of the amplitude of the sinusoidal curve. The highest possible variation of the average value is found when one border of the region covered by the coils happens to be aligned with a zero of the sinusoidal variation. In this case the measured average (indicated as \bar{h}_{meas}) can be expressed by the following equation:

$$\bar{h}_{meas} = \bar{h}_{real} + \bar{h}_{err} \quad (5.7)$$

where \bar{h}_{real} is the real value of the average and \bar{h}_{err} is the error due to the misalignment. The error is given by the following expression:

$$\delta \bar{h}_{err} = \int_0^{L_{co}-L_p} A \sin\left(\frac{2\pi z}{L_p}\right) dz = A \left(1 - \cos\left(\frac{2\pi(L_{co}-L_p)}{L_p}\right)\right) \quad (5.8)$$

where L_{co} is the length of the region covered by the coils array. The variations in time of the measured values of the average are given by:

$$\delta \bar{h}_{ea} = \delta \bar{h}_{real} + \delta \bar{h}_{err} \quad (5.9)$$

In the case of the mid coils array the relation between the variations in time of the average and of the amplitude due to the quoted misalignment is given by:

$$\delta \bar{h}_{err} = 0.32 \delta A \quad (5.10)$$

The average delta is always lower than 30% of the amplitude delta, so that the measured drift could be due to this effect.

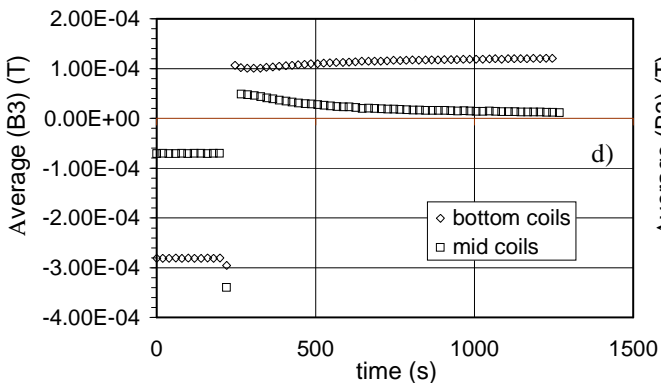
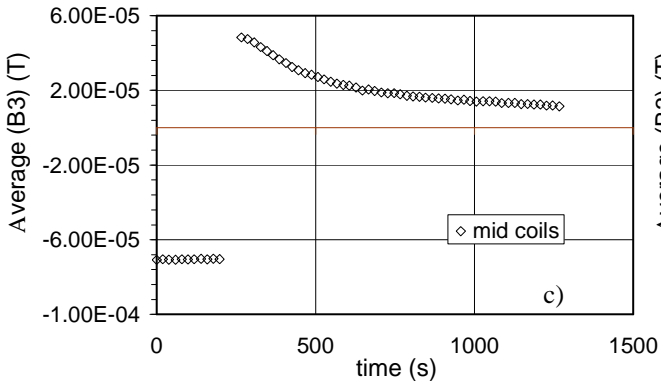
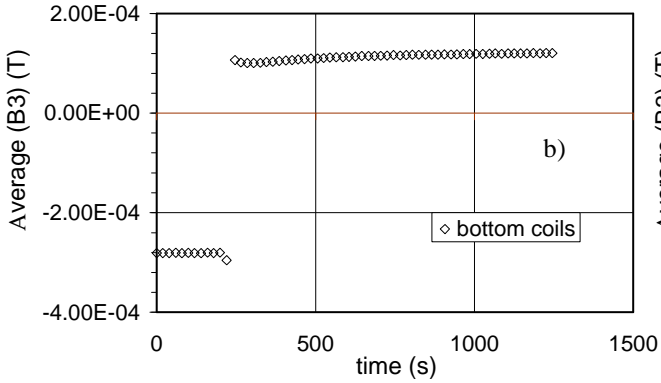
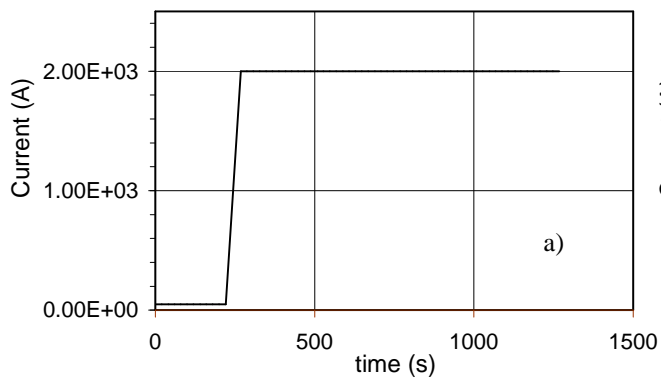


Fig. 5.19 Average variation in time (2000 A, 450 A/s). a) Current sweep. b) Bottom coil measurements. c) Mid coil measurements. d) Comparison between different positions.

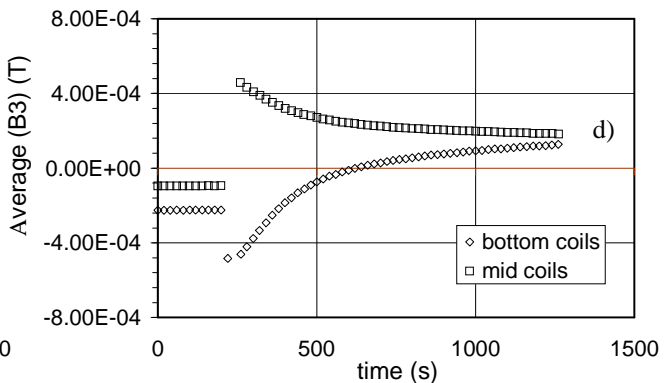
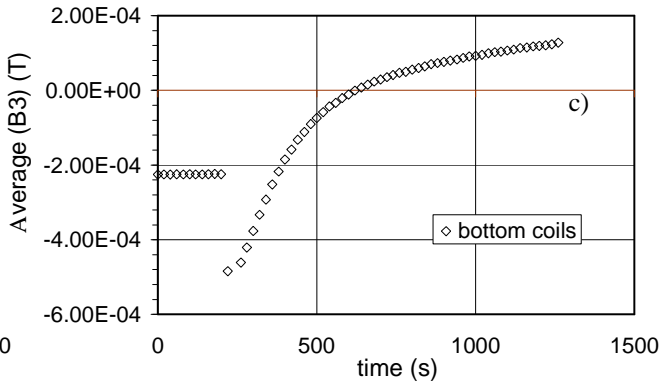
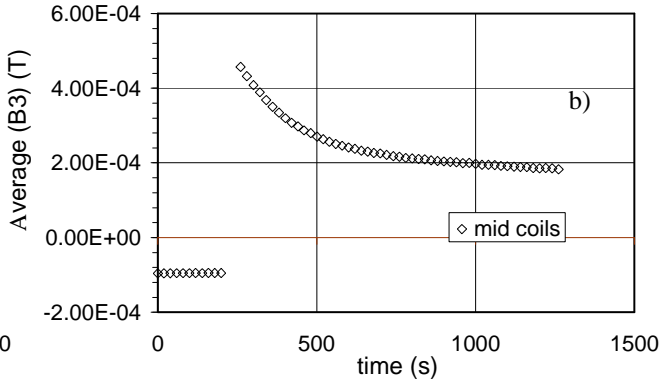
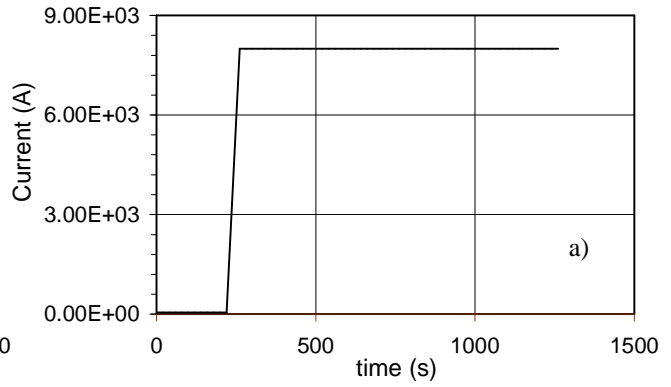


Fig. 5.20 Average variation in time (8000 A, 450 A/s). a) Current sweep. b) Bottom coil measurements. c) Mid coil measurements. d) Comparison between different positions.

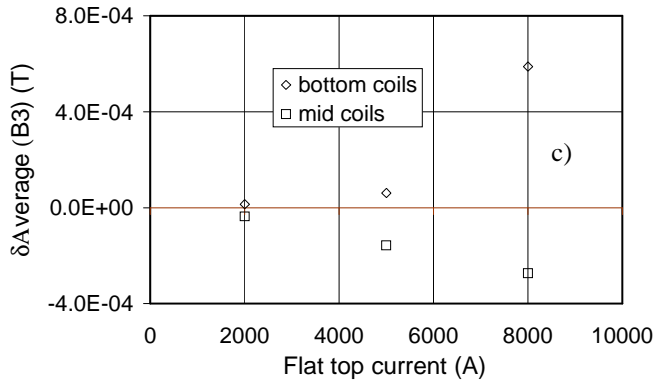
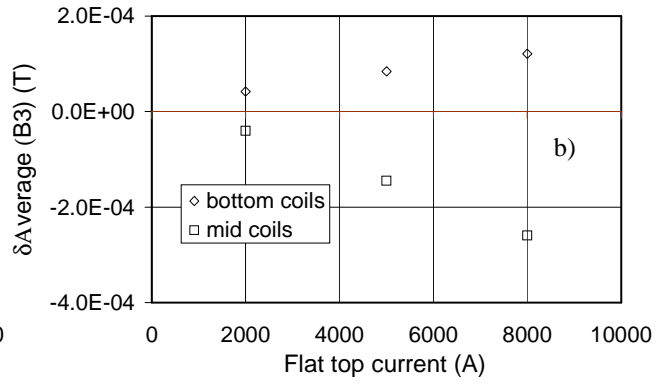
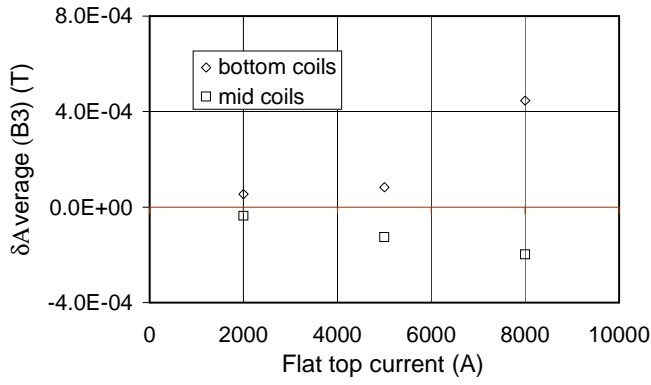


Fig. 5.21 Dependence of the average sextupole variation after 1000 s of decay on the flat top current for different ramp rates. a) 450 A/s. b) 200 A/s. c) 50 A/s.

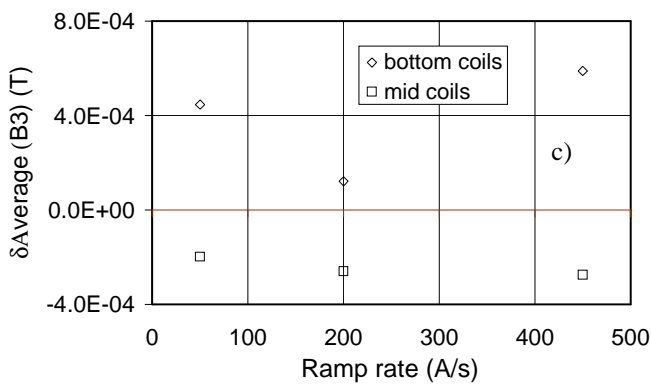
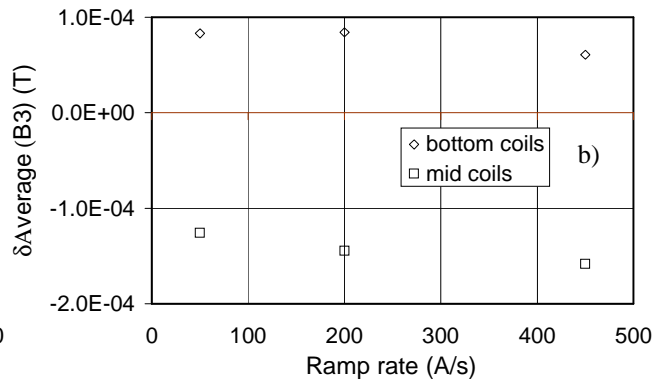
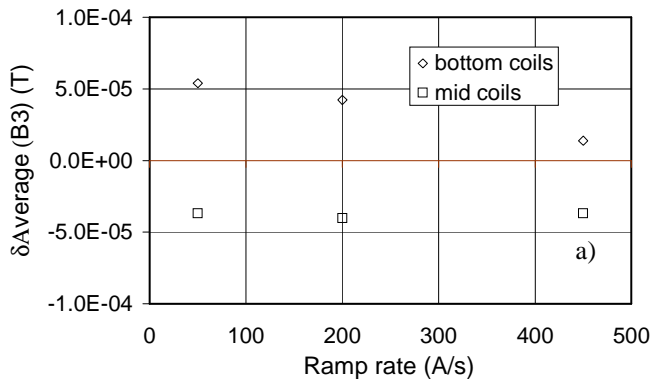


Fig. 5.22 Dependence of the average sextupole variation after 1000 s of decay on ramp rate for different flat top currents. a) 2000 A. b) 5000 A. c) 8000 A.

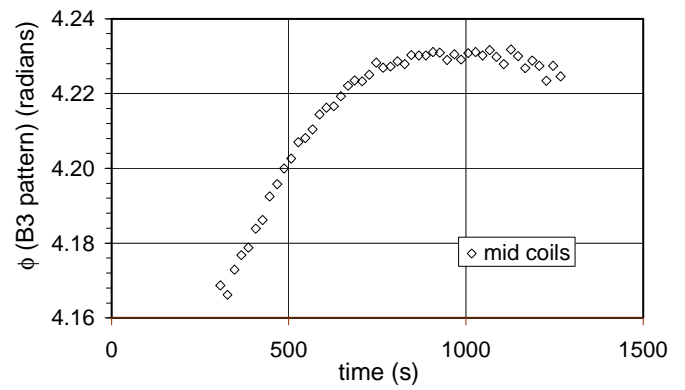
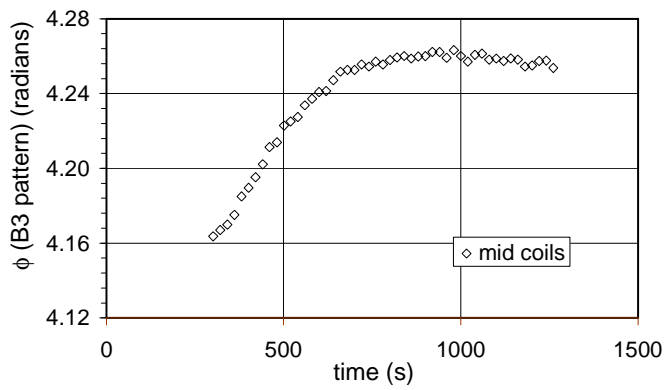
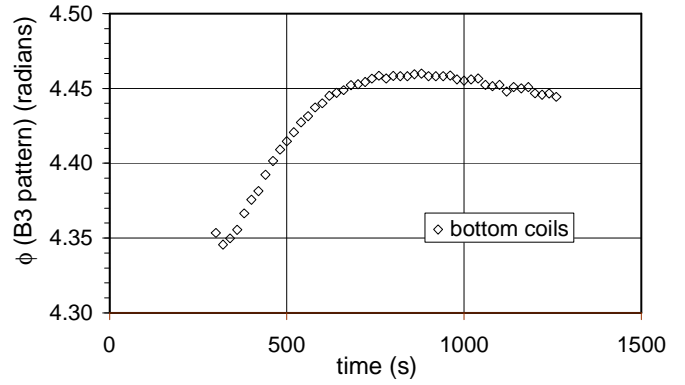
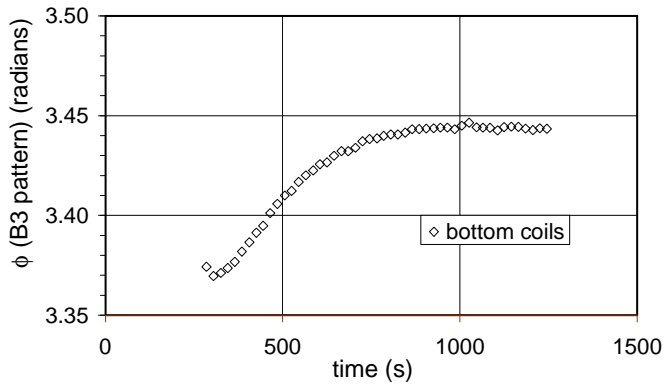


Fig. 5.23 Phase variation during flat top (2000 A, 450 A/s). a) Bottom coils. b) Mid coils.

Fig. 5.24 Phase variation during flat top

(8000 A, 450 A/s). a) Bottom coils.

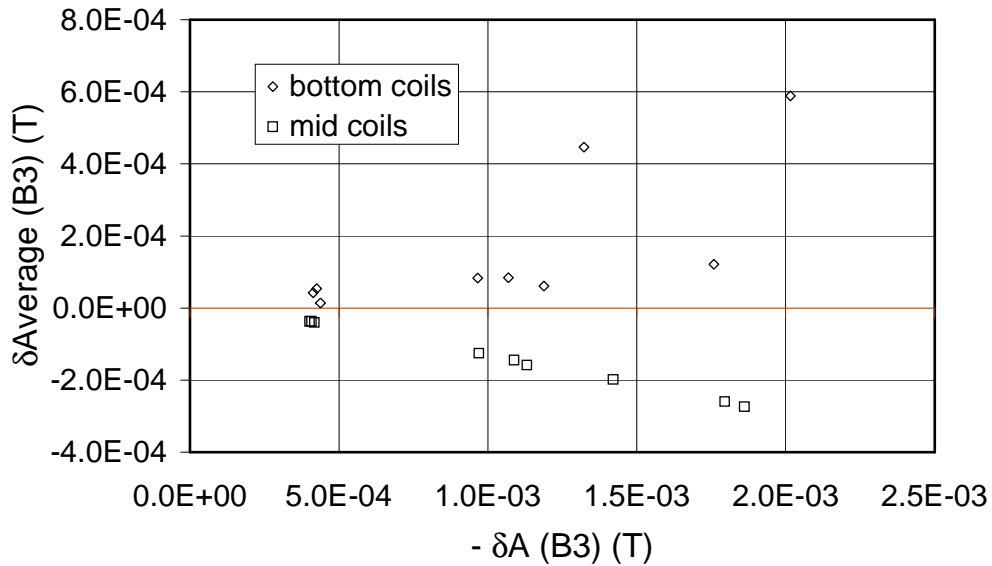


Fig. 5.25 Variation of the average normal sextupole vs variation of the amplitude (changed of sign) of the normal sextupole pattern in the first 1000 s of flat top for all the step response measurements performed.

In every real operation observe longitudinal variations the case of the step response bottom and middle part of the the sinusoidal shape of a

Amplitude of the magnetic field pattern

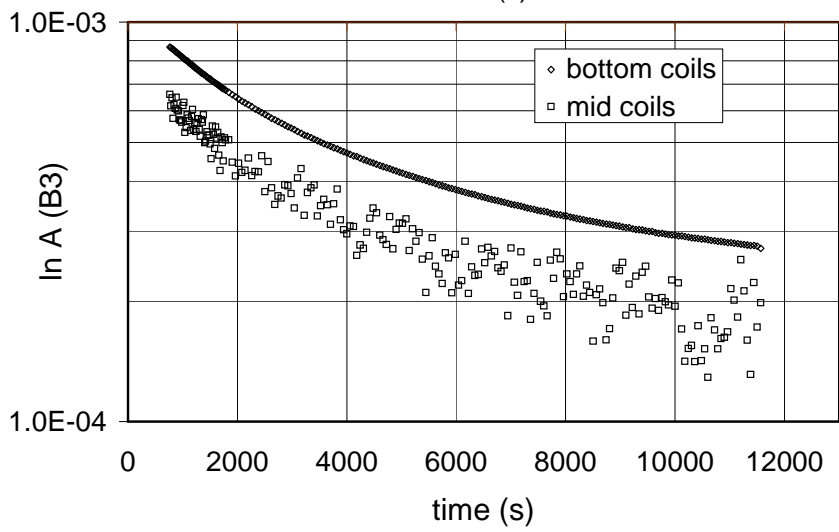
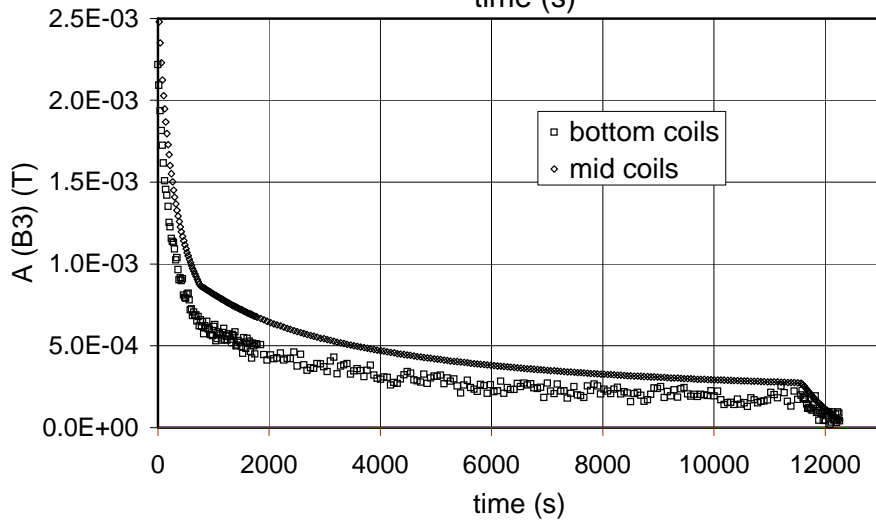
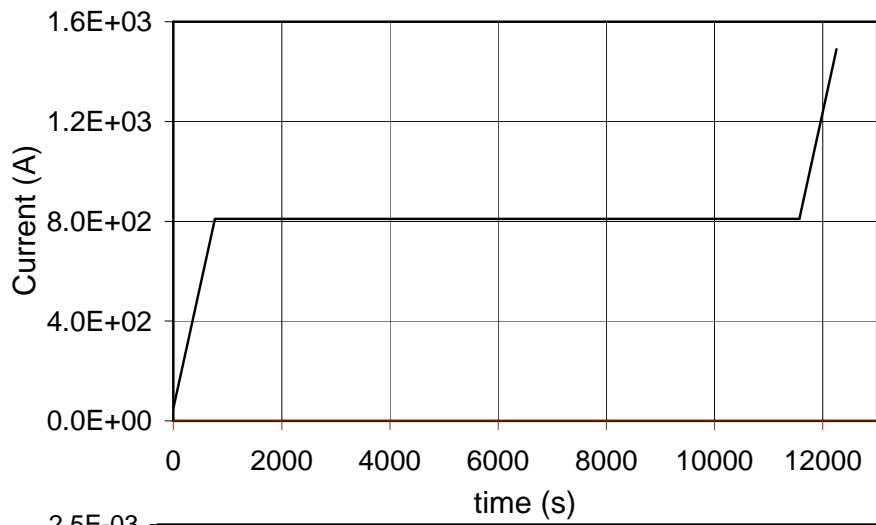
cycle measurement we of the field harmonics. As in measurements, only in the magnet these variations have periodic pattern.

The evolution in time of the sextupole pattern amplitude for the case of a flat top time $T_{FT} = 30$ min and a flat top current $I_{FT} = 11750$ A (nominal current of this dipole model) is shown in Fig. 5.26b for the bottom and middle part of the magnet. The pattern amplitude decreases during the initial ramp until the injection phase starts, in contrast to what observed during the step response runs.

As the injection phase starts, we observe a slope variation in the amplitude curve and the beginning of a slower decay of the pattern amplitude. Figure 5.26c reports a logarithmic plot of the decay phase for the longest measurement performed. This plot shows that the decay curve does not approach a straight line as in the case of the step response measurements. It seems that there is a superposition of different time constants and that the highest are so large that even with this very long measurement (12000 s of injection phase) it is not possible to reach a simple exponential regime. In shorter measurements (1000 s) the decay phase can be well fitted with an exponential curve. The time constants of these fitting curves range from 2000 to 5000 s. These time constants are larger than the measurement time and have to be considered only as characteristic times of the initial phase of the decay.

During the final ramping up, there are evident variations of the amplitude of the sextupole pattern. The variation in time of the pattern amplitude is shown in Fig. 5.27 for measurements with different pre-cycle flat top times.

Fig. 5.26 Amplitude variation in time after a pre-cycle with $T_{FT} = 30$ min, $I_{FT} = 11750$ A. a) Current sweep during measurement. b) Comparison between different positions. c) Logarithmic plot of the decay phase



The pattern amplitude behaves essentially in the same way in the two locations at the bottom and center of the magnet, and *is strongly dependent on the current cycle*.

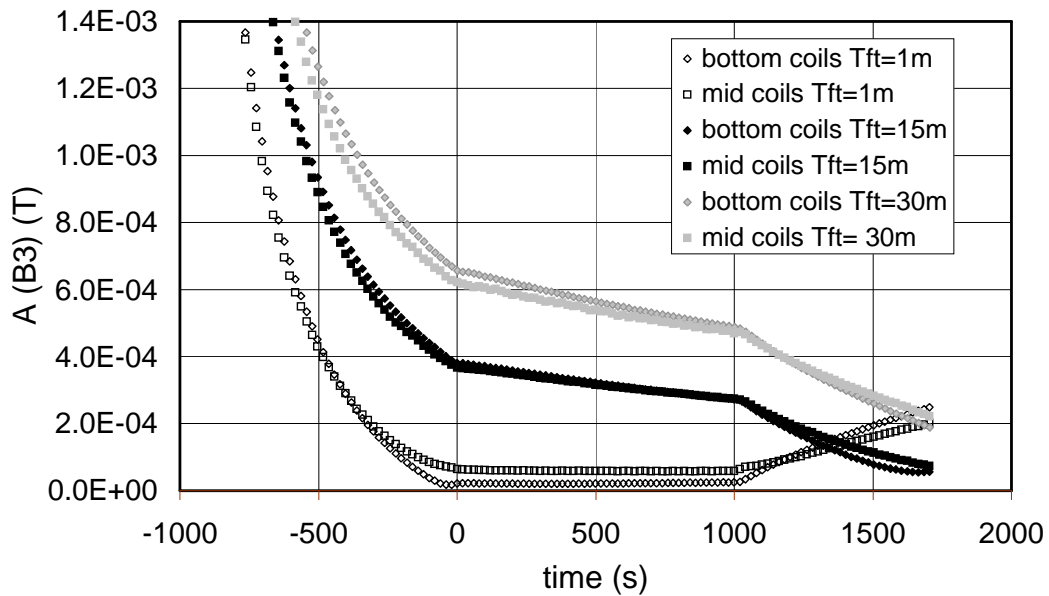
With very short flat top times the pattern has a decreasing amplitude during the initial ramp, until it disappears during the injection phase (see the curves for a 1 minute flat top time in Fig. 5.27). The periodic pattern restores during the final ramp.

In analogy to the study of the step response measurements we have estimated the pattern amplitude decay during the injection phase measured with different pre-cycles, considering the pattern amplitude variation after 1000 s from the beginning of the decay:

$$\delta A = A(t_2 + 1000 \text{ s}) - A(t_2) \tag{5.11}$$

where t_2 is the time at which injection begins.

Fig 5.27 Variation in time of the amplitude of the normal sextupole pattern after pre-cycles with different flat top times.



The time reference is set to zero at the beginning of the injection phase.

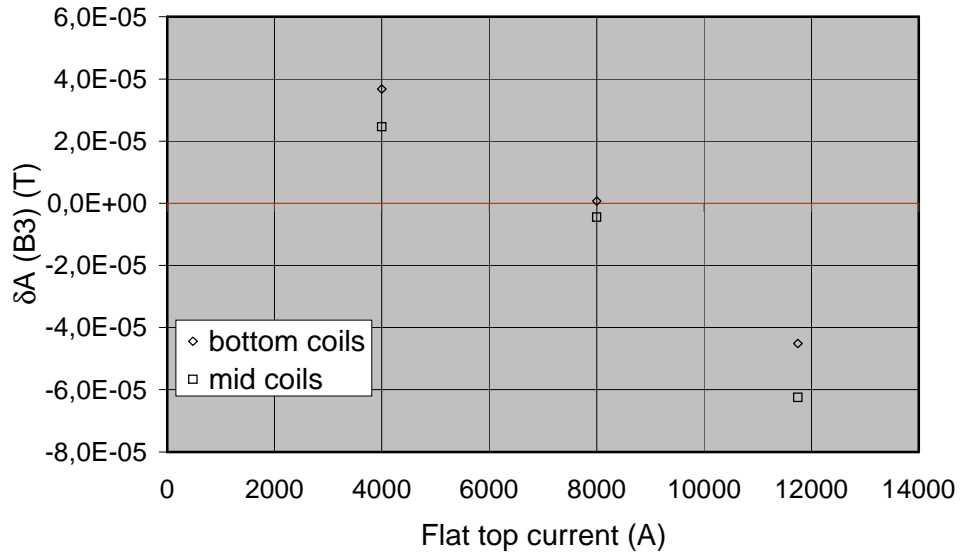


Fig. 5.28 Dependence of the amplitude variation of the normal sextupole pattern after 1000.s of constant current phase on pre-cycle flat top current.

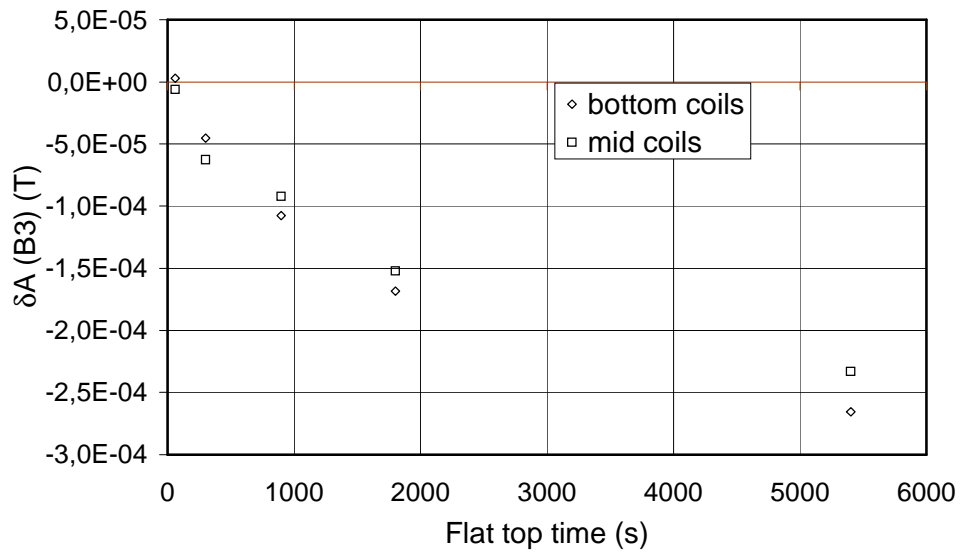


Fig. 5.29 Dependence of the amplitude variation of the normal sextupole pattern after 1000.s of constant current phase on pre-cycle flat top time.

The results show that there is a clear correlation between $\delta A(B_3)$ and both the flat top current and the flat top time. The change of sextupole pattern scales approximately linearly with the flat top current reached in the pre-cycle (see Fig. 5.28).

The scaling with the flat top time (see Fig. 5.29) in the pre-cycle can be well approximated by the following exponential function

$$\delta A = K + B \cdot \left(1 - e^{-\frac{t_{FT}}{\tau}} \right) \quad (5.12)$$

where K , B , and τ are fitting parameters and t_{FT} is the flat top time. The values of the fitting parameters are reported in Table 5.1 for different measurements.

Bottom coils	1.82	$-2.87 \cdot 10^{-4}$	$+6 \cdot 10^{-6}$
	B3	τ (* 10^3 s)	

Mid coils	1.95	$-2.36 \cdot 10^{-4}$	$-1.09 \cdot 10^{-5}$
-----------	------	-----------------------	-----------------------

Table 5.1 Fitting parameters for the dependence of the sextupole pattern amplitude variation after 1000 s from the beginning of the injection phase on the pre-cycle flat top time. The parameters are calculated by means of the fitting function (5.12).

As reported in [34], the decay of the average multipoles during injection follows the same scaling with the pre-cycle flat top time and flat top current.

Average value of the field harmonics

The normal sextupole always exhibits the same kind of variation in time, as shown in Fig. 5.30 for measurements after pre-cycles with different flat top times in the same cases reported in Fig. 5.27. At the end of the decay we observe the characteristic ‘snapback’ [34], and the following enhancement of the average value during the final ramp.

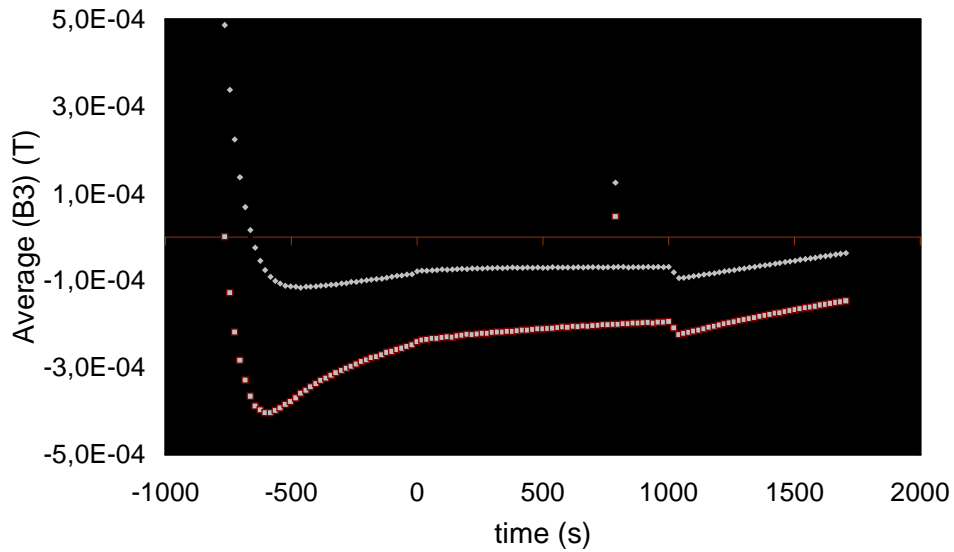


Fig 5.30 Variation in time of the average value of the normal sextupole pattern after pre-cycles with different flat top times. The time reference is set to zero at the beginning of the injection phase.

It is interesting to note that the variation of the average value of the sextupole with very short flat top times is not negligible.

This variation is not due to the relation of the current distribution with the superconductor magnetization because in this case the amplitude of the pattern is negligible. The variation may be due to the thermally activated “flux creep” occurring in the superconducting material of the cable, as already observed in [34, 68].

Phase of the modulation of the field harmonics

The variation of the initial phase of the field modulation during the operation cycle measurements is always very small. The phase variation during the injection phase of the longest measurement performed is reported in Fig. 5.31 in the bottom position of the magnet. The average translation velocity in this case is of about $9 \cdot 10^{-8}$ m/s, equivalent to 0.3 mm/h. The longitudinal displacement of the pattern is negligible.

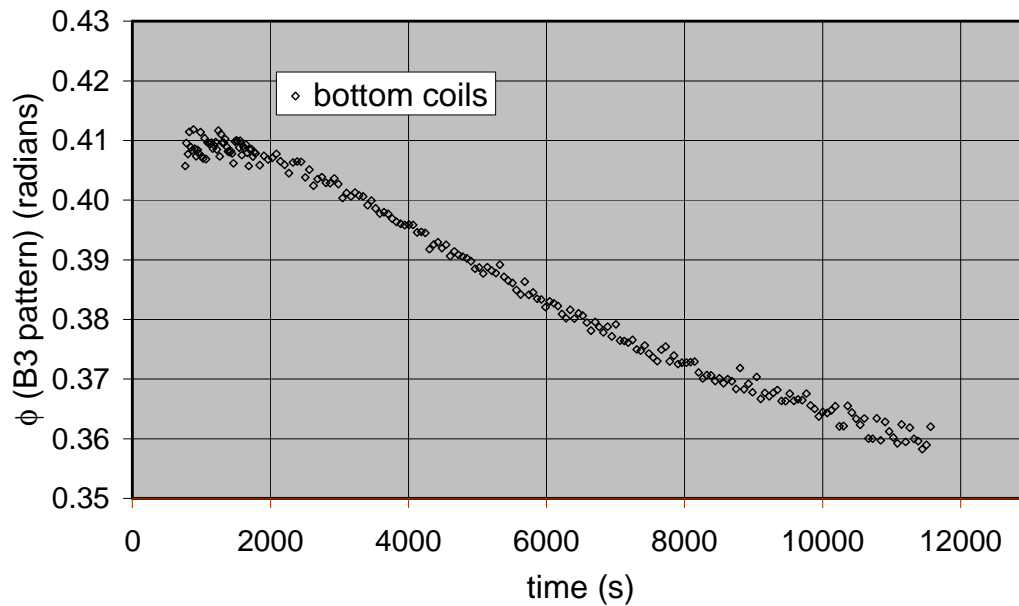


Fig 5.31 Initial phase of the sextupole pattern during the injection of the longest measurement performed (pre-cycle with $T_{FT} = 30$ min and $I_{FT} = 11750$ A).

Comparison between average and amplitude variations

The amplitude variation and the field drift exhibit a similar dependence on the pre-cycle flat top time at both positions of the magnet.

The variation of the average value is plotted in Fig. 5.32 as a function of the amplitude variation for every real operation cycle measurement.

The apparent correlation between the variation of the amplitude and the variation of the average in correspondence of the middle part of the magnet indicates that the two phenomena are indeed dependent on each other, as hypothesized in [28].

In the case of real operation cycles measurements we can exclude that the average value variation is only due to the effect of misalignment between the coil group and the sinusoidal oscillation explained in Section. 5.2.8 for the step response measurements. If that were the case, due to the linear dependence shown in eq. 5.5, we would expect the same kind of temporal evolution for the amplitude of the periodic pattern and the average value of the harmonic considered. Instead,

we note in Fig. 5.30 the characteristic snap-back of the average value, which has not any corresponding feature in the amplitude variation in the same measurements (see Fig. 5.27).

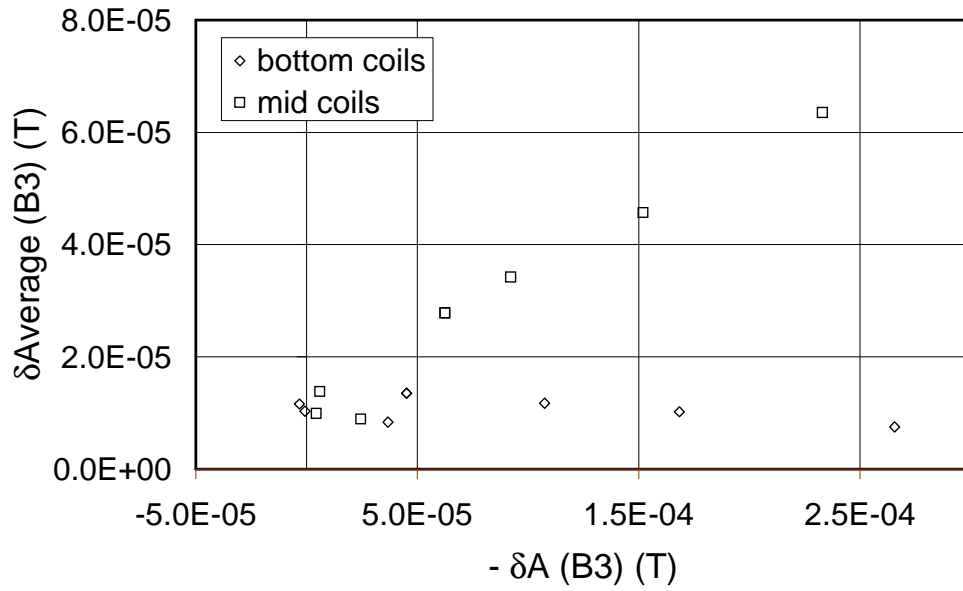


Fig. 5.32 Average delta variation versus amplitude variation (changed of sign) for all operation cycles measurements.

5.3 MODEL VALIDATION

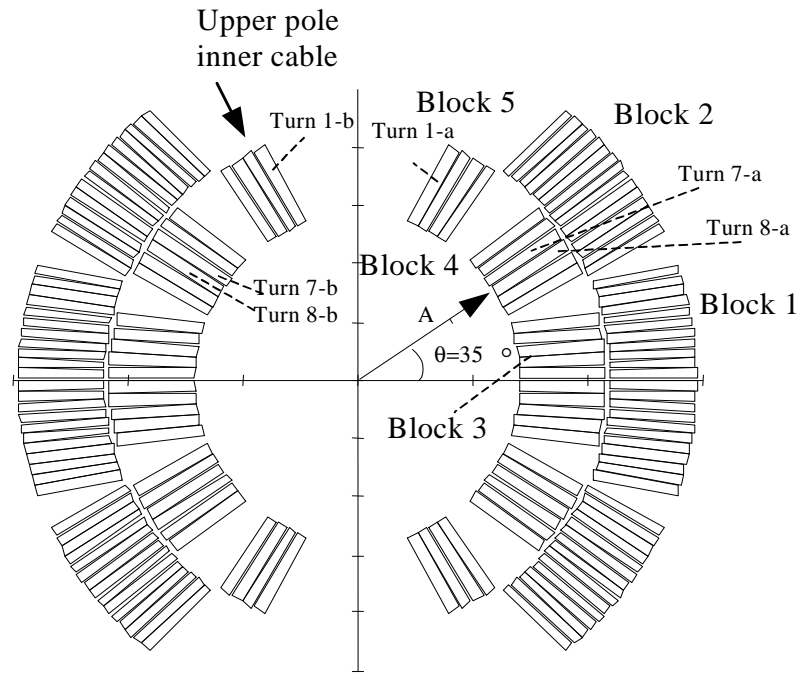


Fig. 5.33 Cross section of one aperture of the double aperture dipole model MBSMT1 used for the measurements of magnetic field pattern.

This section is dedicated to the analysis of the experimental findings described in Section 5.2. In this analysis we use both the network and the distributed parameters circuit model. The first one is based on a network approach which approximates the cable as a lumped parameters circuit. The network model (see Section 2.3.2) used in this study is that described in detail in [19].

The distributed parameters circuit model is described in Section 3.1.

5.3.1 Basic assumptions for the simulations

We postulate that the periodic magnetic field pattern is due to the long current loops circulating in the cable. In this study we consider a single cable subjected to both a current increase and, proportional to it, a non uniform time dependent magnetic field. The iron saturation at high magnetic fields is neglected. The strands of the cable are assumed to be identical, ideally transposed, and soldered to current leads via electrical resistances which are much lower than the

contact resistances of the cable. Finally, the latter are assumed to be equal, and uniform along the cable length.

Therefore, among the possible sources of non uniform current distribution listed in Section 2.1 the only source of long range current loops that we consider here is the field variation along the cable length.

A schematic view of the coil cross section of one aperture of the LHC dipole model MBSMT1 is shown in Fig. 5.33. The coil has two poles (upper and lower) assembled from an inner and an outer layer. The inner layer of a single pole is wound from 15 turns arranged into 3 blocks, while the outer layer has 26 turns arranged in 2 blocks corresponding to different angular positions. We have numbered turns and blocks as shown in Fig. 5.33.

The layers in a pole are wound individually, and the cable ends are either soldered together at the interconnection between layers and poles or connected through splices to the current leads. Because of the assumption of low splice resistance compared to the interstrand resistance in the cable, we can identify a cable unit length in a single layer (i.e. between two splices) as the shortest length to be used for analysis purposes.

In order to simulate the experimental results on the amplitude of the magnetic field pattern reported in Section 5.2, we assume that the longitudinal oscillations of the secondary field are only due to the current distribution in the inner cable of the magnet. This assumption is motivated by the fact that the periodicity of the measured oscillations of the secondary magnetic field is equal to the inner cable twist pitch.

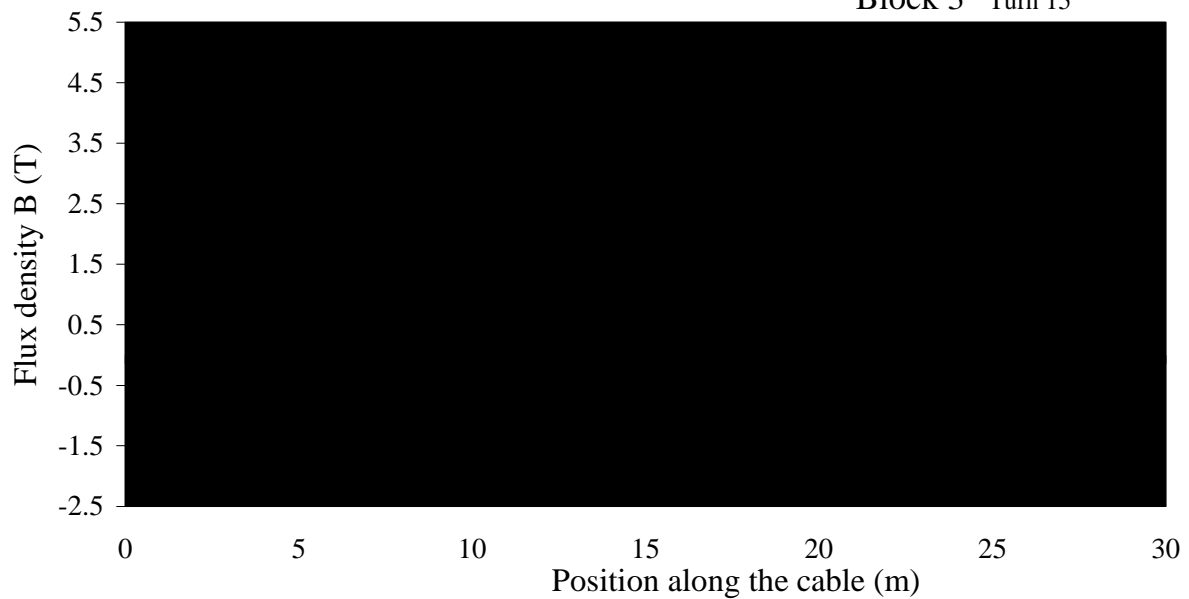


Fig. 5.34 *Magnetic flux density perpendicular to the broad face of the inner cable of the 1m long LHC dipole magnet MBSMT1. The reported field is the average field across the cable width calculated with ROXIE, at a total current of 11500 A.*

A unit length of the inner layer cable is made of 28 strands, with a total length L of 27.8 m, a twist pitch of 115 mm., and a thickness of 1.88 mm.

As we stated previously, we take spatial variations of the magnetic flux as the only source of long range current loops. The distribution of the magnetic flux density perpendicular to the broad face of the cable calculated with the computer program ROXIE [69] is shown in Fig. 5.34. We recognize two types of variations of the perpendicular field along the cable length.

Sharp, short range variations of the field are due to the cable bending over the magnet bore, while step changes in the value of the field along the straight part of the cable correspond to the transitions from block to block.

We have performed two sets of simulations using either the network or the continuum model, in order to imitate the cable excitation with current cycles made of a linear ramp up followed by a current plateau as were performed in the experiments reported in the previous section.

Simulations with the network model are aimed to look at the fine details of the origination of the short and long range eddy currents. The size of the network model grows quickly with the length of cable analyzed. For this reason we limited the simulations to a short length of cable to explore general features of the transient response of the long range current loops to field changes.

We have then performed simulations of the whole cable response to current steps with the distributed parameters model. This model does not reproduce accurately the details, but is suitable for the simulation of a full cable length in a magnet.

In both sets of simulations we have varied parametrically the flat top current and the ramp rate in order to study their influence on the current distribution.

5.3.2 *Network model*

The simulations using the network model have been focussed at an ideal cable close to the coil midplane. In order to minimize the computation time, a four strand cable has been considered. The cable length L is equal to approximately 23 twist pitches. We have assumed a symmetric magnetic field distribution along half of the cable length, shown in Fig. 5.35. The magnetic field is zero at the cable ends and at its center. In between, there are regions of uniform magnetic field. The magnetic field is twice as high at the inner edge of the cable as at the outer one.

This geometry imitates a complete turn in a dipole magnet, where the uniform field regions represent the straight length of the magnet included between the low field regions at the magnet ends.

Let us consider elemental current cycles made of a ramp up followed by a current plateau. Let also the plateau current be much less than the critical current. The results of simulations show that soon after the beginning of the cycle eddy currents associated with the local value of dB/dt appear.

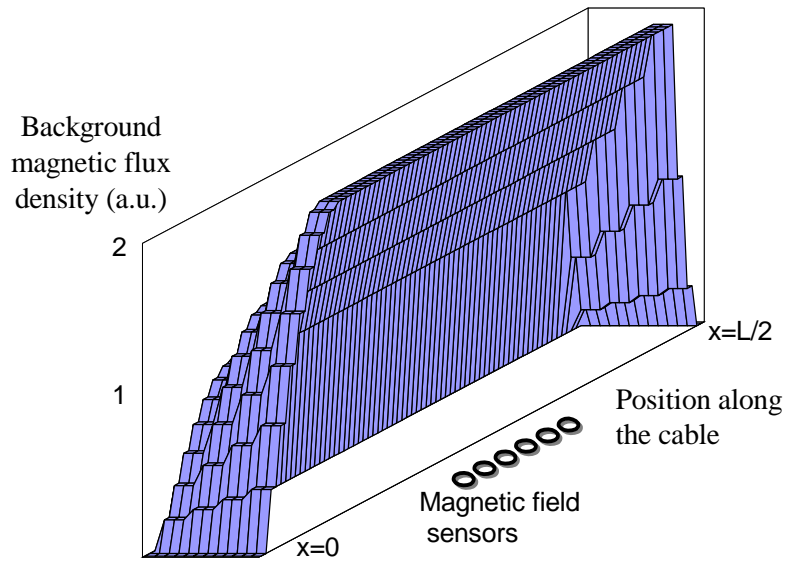


Fig 5.35 Magnetic flux density perpendicular to the broad face of the ideal cable considered for the simulations performed with the network model.

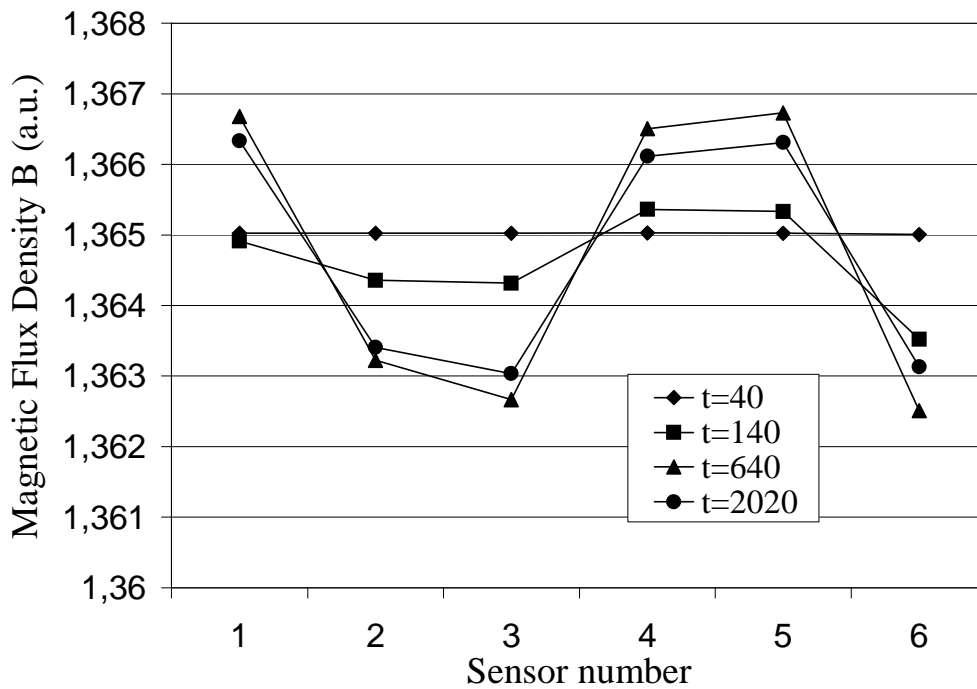


Fig. 5.36 Development of magnetic field pattern in the uniform field region

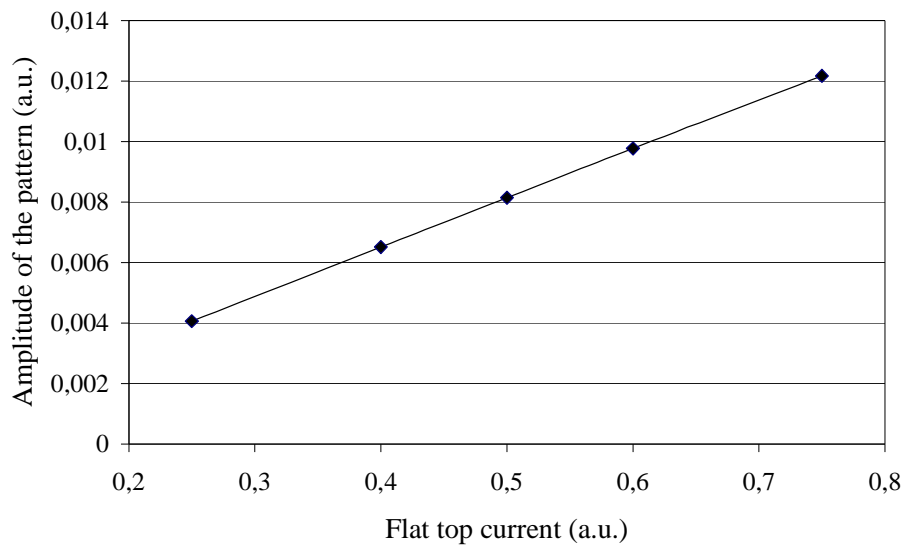


Fig. 5.37 Dependence of the amplitude of the magnetic field pattern on the flat top current at the end of the ramp.

These eddy currents produce a uniform field in the neighborhood of the cable, without any periodic oscillation. Gradually, however, the strand currents become different in the ends of the cable, where the magnetic field has a longitudinal gradient, thus originating current loops.

As time advances, the current in these loops diffuses from the cable end regions into the center. The time t_p needed to complete this process is much higher than the time of development of uniform, short range eddy currents.

The buildup and following decay of a periodic magnetic field pattern is shown in Fig. 5.36. The amplitude of the pattern increases at $t < t_p$ and decreases afterwards.

Calculations show that if the time of the ramp is short compared to t_p , the amplitude of the periodic magnetic field pattern on the plateau at a certain moment, $t > t_p$ does not depend on the ramp rate, while it is linearly dependent on the flat top current (see Fig. 5.37).

5.3.3 Distributed parameters model

We have performed calculations with the continuum model for a cable made of 28 strands, as in reality, and with a cable composed of 8 *equivalent* superstrands.

In accordance with measured value in the dipole model MBSMT1, we have taken a contact resistance between strands in the range 10 to 20 $\mu\Omega$ per contact.

We have used the magnetic field map shown in Fig. 5.34 as an input for the calculation, scaling the field proportionally to the current in the magnet. In the simulations performed with the continuum model we have neglected the field variations across the cable width. This, as demonstrated in the detailed analysis discussed in the previous section, is inessential for the development of long range current loops.

The results of simulations are reported in Fig. 5.38 for a current step with a ramp rate of 50 A/s and a final current of 2000 A. It can be noticed that soon after the beginning of the ramp sharp current spikes appear in these regions of high field gradient (Fig. 5.38a). At the end of the field ramp the correspondence between the field profile and the current pattern is less evident (Fig. 5.38b). After 1000 s from the beginning of the current flat top, we note a remarkable current difference between the strand currents, but the correspondence with the field profile is lost (Fig. 5.38c).

As we have postulated that the magnetic field pattern is due to long current loops circulating in the cable, it is reasonable to assume that its amplitude is proportional to the difference between the currents flowing in the strands. In particular we have taken the values of the maximum difference between the strand currents in the middle of the uniform field regions, ΔI_{max} , as the reference quantity for a qualitative comparison with the amplitude of the magnetic field pattern measured outside the cable and next to these positions.

As an example we compare in Fig. 5.39 the amplitude of the total magnetic field pattern at position A ($r = 17$ mm and $\theta = 35^\circ$) to the parameter ΔI_{max} calculated for turn 7-a which faces the point selected. The amplitude of the total field pattern has been reconstructed at point A from the

data presented in Section 5.2, obtained with the rotating coils placed in the middle of the straight length of the magnet. The comparison is shown for a step response measurement with $I_{FT} = 2000\text{A}$ and $RR = 50 \text{ A/s}$. We have performed the simulations with the complete 28 strands cable, for different values of the cross contact resistances (10 and 20 $\mu\Omega$).

The value of ΔI_{max} at the end of the ramp calculated in four consecutive straight parts of the cable (turns 7-8, see Fig. 5.33) is shown in Fig. 5.40 for the case of $RR = 450 \text{ A/s}$. These simulations have been performed with the equivalent, 8 superstrands cable for the whole set of ramp rates and flat top currents considered in the experiments, and the results confirm that the amplitude of ΔI_{max} at the end of the ramp is proportional to the flat top current and approximately independent on the ramp rate, as obtained in the experiments and with the network model.

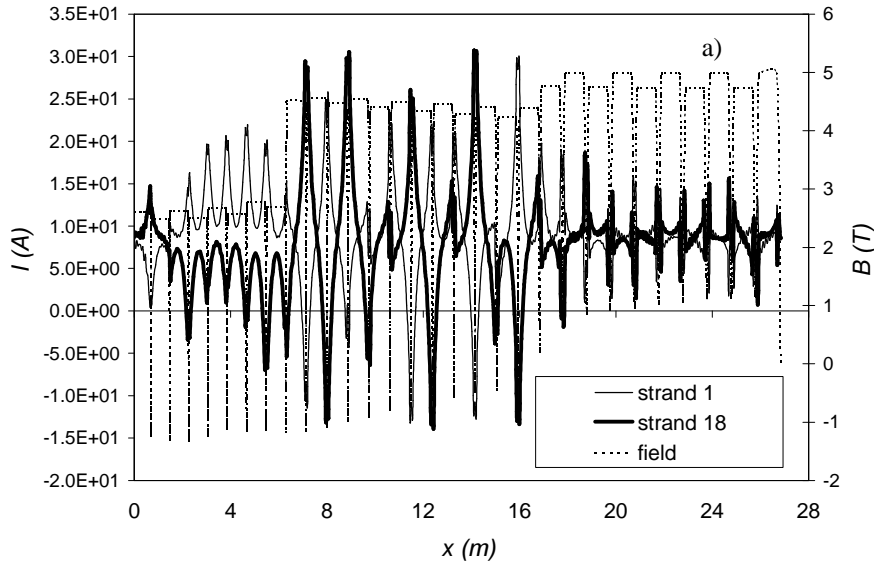
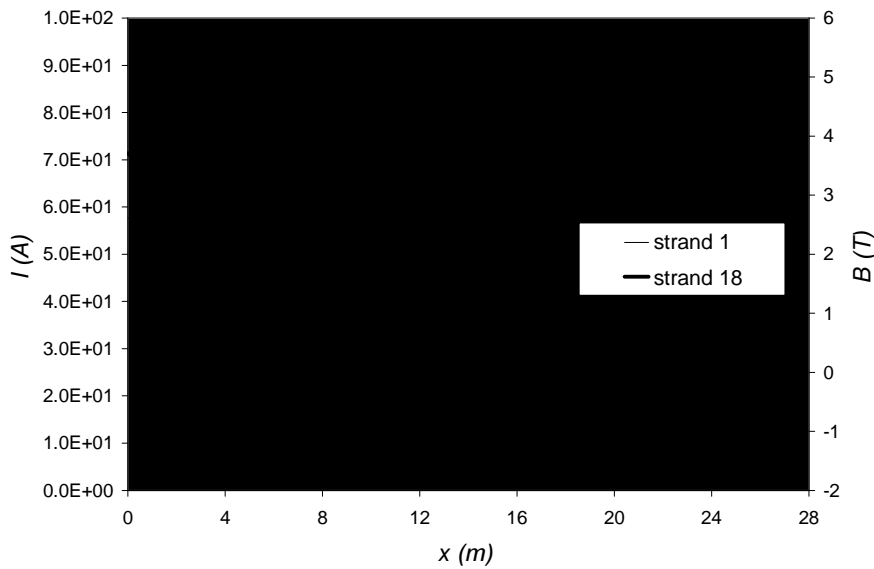
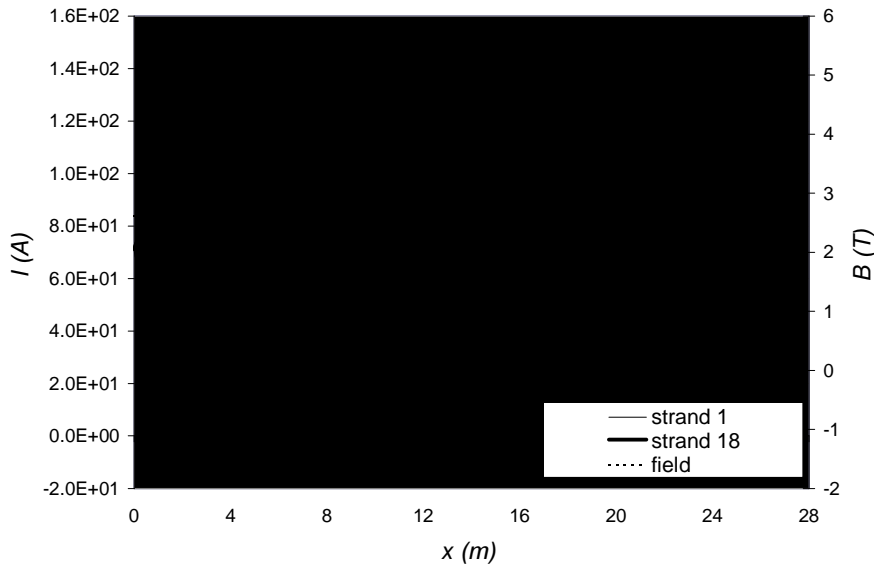


Fig. 5.38 Behaviour of the currents in two strands of the 28 strand cable along the cable length at different times. $RR = 50 \text{ A/s}$ $I_{FT} = 2000 \text{ A}$ a) $t = 3.85 \text{ s}$ (soon after ramp start) b) $t = 39 \text{ s}$ (end of the ramp) c) $t = 1039 \text{ s}$ (end of the plateau). The dotted line indicates the main background magnetic field perpendicular to the cable axis calculated at $i_{OP} = 11500 \text{ A}$.



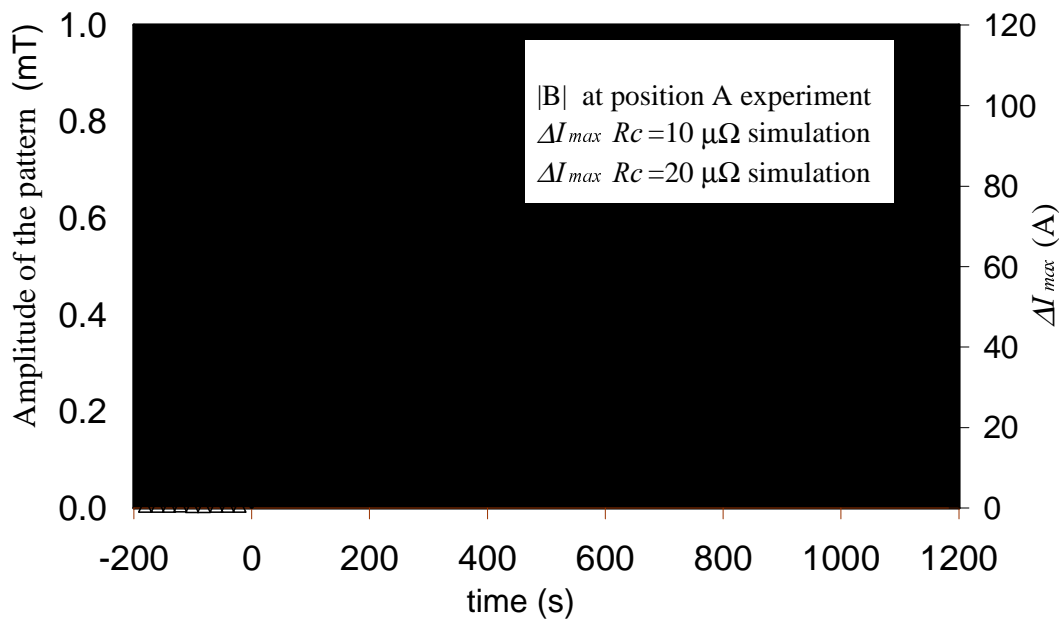
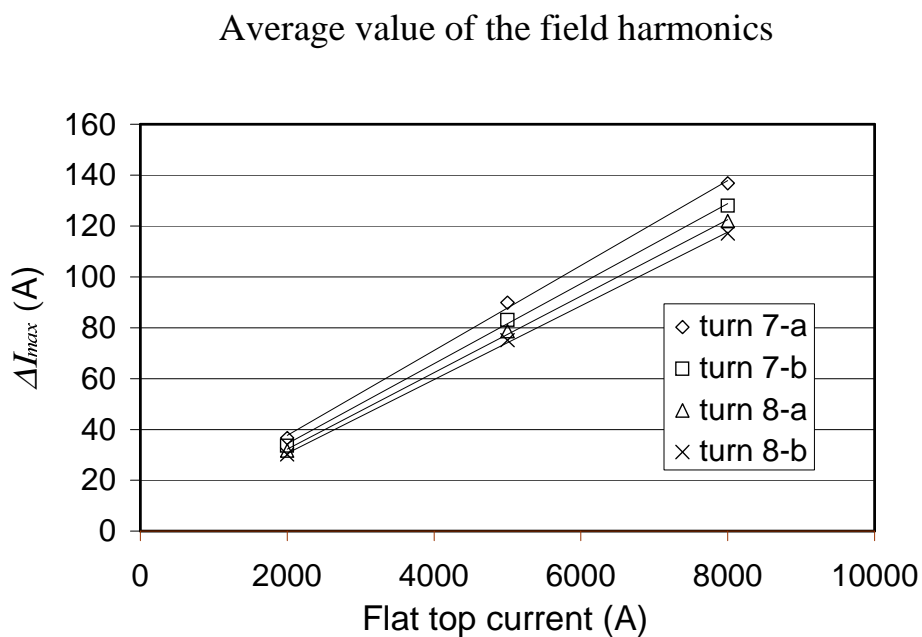


Fig. 5.39 Comparison between the time evolution of the amplitude of the periodic pattern in the middle of the uniform field region and that of parameter ΔI_{max} calculated at turn 7-a. Time t is set to zero at the beginning of the current step, made of a linear increase up to 2000 A with a ramp rate of 50 A/s and a flat top of 1000 s at the maximum current.

Fig 5.40 Dependence of parameter ΔI_{max} on the final flat top current in different cable turns (RR=450 A/s).



The temporal evolution of the average harmonics over the two coil groups mid and bottom [see definition (5.3)] is shown in Fig. 5.19 for the step response measurement with a 2000 A flat top current and a 450 A/s ramp rate and in Fig. 5.20 for the step response measurement with 8000 A

flat top current and 450 A/s ramp rate. The variation in time is different for the two positions in the magnet, but each kind of pattern is repeated in different experiments.

The average in the mid coil measurements always decreases during the constant current phase, while in the bottom coil measurements it always increases. The variation of the average value after 1000 s from the beginning of the flat top phase has been taken as a parameter to compare different experiments. The plot of this parameter versus the flat top current and the ramp rate is shown in Figs. 5.21 and 5.22 respectively.

In the case of the mid coil measurements we can observe that the variation of the average is approximately linear with the final current, and constant with the ramp rate.

Phase of the modulation

The variation in time of the phase ϕ of the normal sextupole pattern is shown in Figs. 5.23 and 5.24 for the same measurements reported in Figs. 5.19 and 5.20. We have found the same kind of phase variation in every measurement. We observe that the maximum change of the phase of the sinusoidal fit of the measured data is approximately equal to 0.1 radians during a total time of 1000 s. The phase shift of the sinusoidal pattern is equivalent to a translational movement of the pattern along the magnet axis. The average linear velocity of this translation can be calculated as follows:

$$v_t = \frac{\Delta\phi}{\Delta t} \cdot \frac{L_p}{2\pi} \quad (5.6)$$

where v_t is the translational velocity and $\Delta\phi$ the total phase variation.

We obtain an average velocity of about $1.8 \cdot 10^{-6}$ m/s, equivalent to 6.6 mm/h. This value is negligible, also considering that in the final part of the decay the phase variation in time is slower than in the initial part.

Comparison between average and amplitude variations

Considering the measurements referred to the middle part of the magnet, we note that the same dependence on the final current and on the ramp rate is shown by the variation of the amplitude of the sextupole pattern after 1000 s of decay and by the variation of the average over the mid coil group in the same time interval. These variations are in fact linearly dependent on the final current and independent of the ramp rate. The variation of the average is in all cases in the range from 10 to 15% of the variation of the amplitude of the periodic pattern (see Fig. 5.25).

The variation of the average could be due to the mismatch between the total length covered by the measurement coils and the inner cable twist pitch. The integral of the sinusoidal variation over this region contributes to the determination of the average value and depends linearly on the value of the amplitude of the sinusoidal curve. The highest possible variation of the average value is found when one border of the region covered by the coils happens to be aligned with a zero of the sinusoidal variation. In this case the measured average (indicated as \bar{h}_{meas}) can be expressed by the following equation:

$$\bar{h}_{meas} = \bar{h}_{real} + \bar{h}_{err} \quad (5.7)$$

where \bar{h}_{real} is the real value of the average and \bar{h}_{err} is the error due to the misalignment. The error is given by the following expression:

$$\delta \bar{h}_{err} = \int_0^{L_{co} - L_p} A \sin\left(\frac{2\pi z}{L_p}\right) dz = A \left(1 - \cos\left(\frac{2\pi(L_{co} - L_p)}{L_p}\right)\right) \quad (5.8)$$

where L_{co} is the length of the region covered by the coils array. The variations in time of the measured values of the average are given by:

$$\delta \bar{h}_{ea} = \delta \bar{h}_{real} + \delta \bar{h}_{err} \quad (5.9)$$

In the case of the mid coils array the relation between the variations in time of the average and of the amplitude due to the quoted misalignment is given by:

$$\delta \bar{h}_{err} = 0.32 \delta A \quad (5.10)$$

The average delta is always lower than 30% of the amplitude delta, so that the measured drift could be due to this effect.

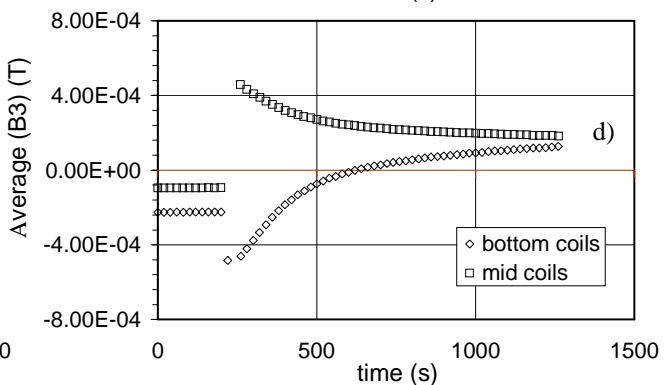
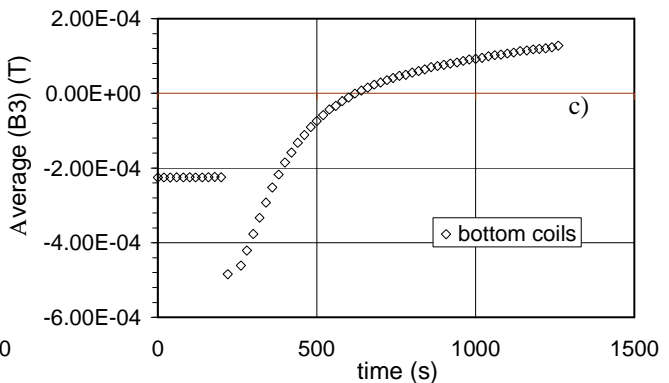
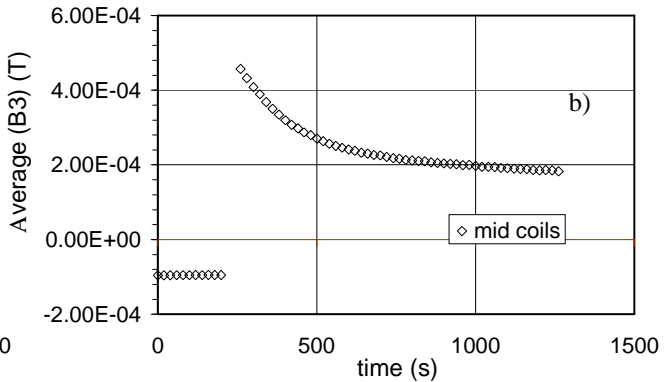
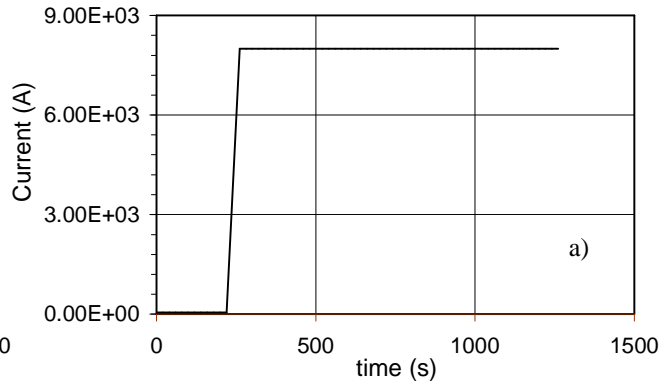
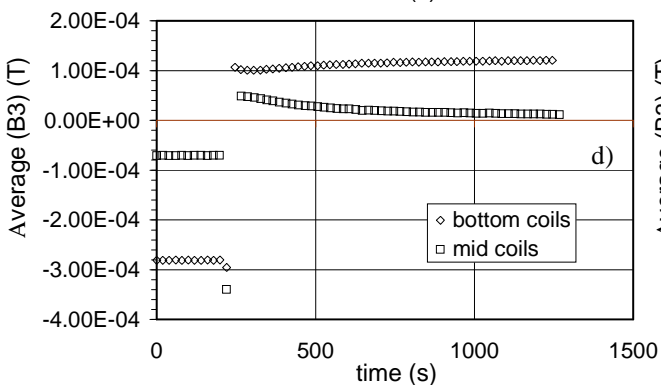
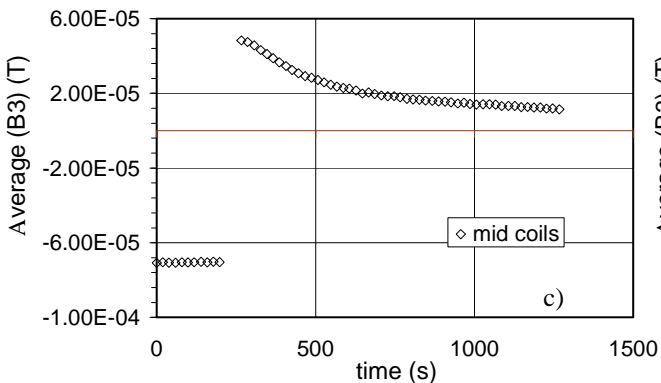
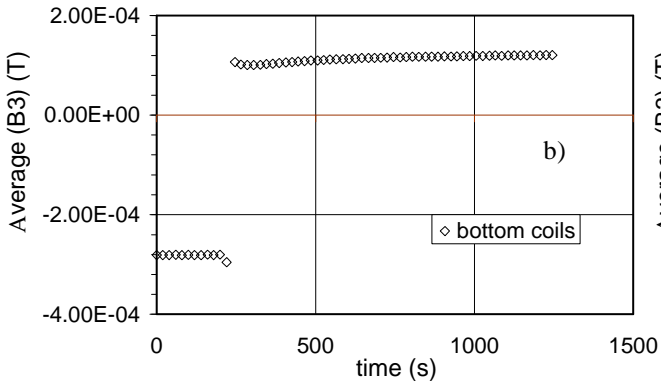
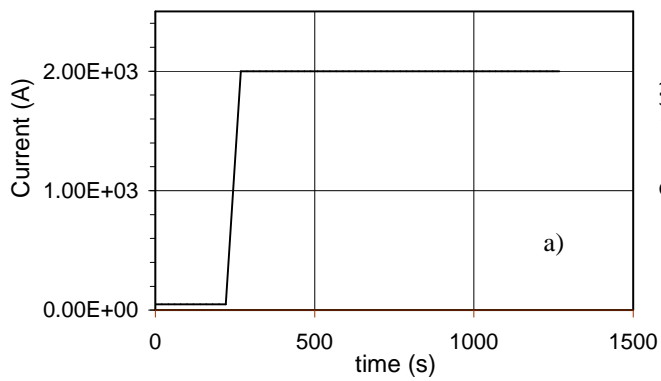


Fig. 5.19 Average variation in time (2000 A, 450 A/s). a) Current sweep. b) Bottom coil measurements. c) Mid coil measurements. d) Comparison between different positions.

Fig. 5.20 Average variation in time (8000 A, 450 A/s). a) Current sweep. b) Bottom coil measurements. c) Mid coil measurements. d) Comparison between different positions.

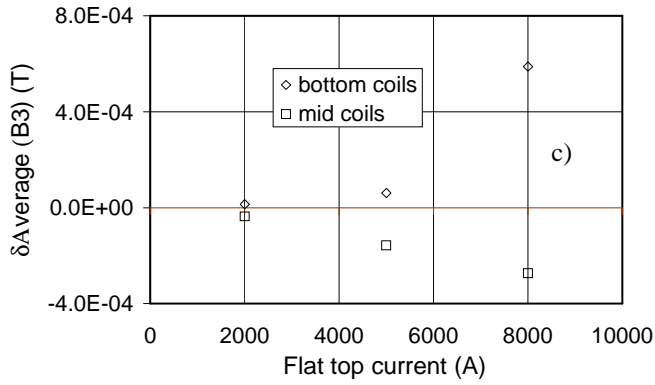
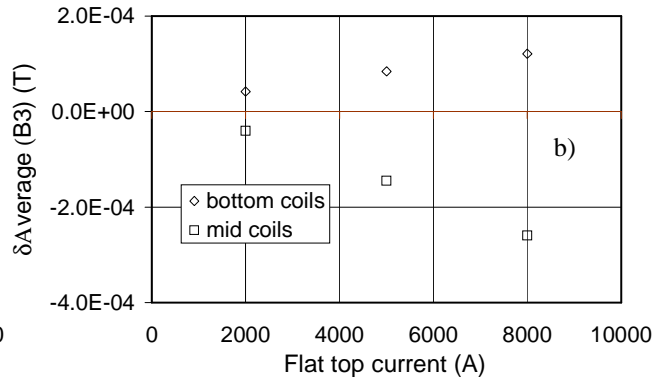
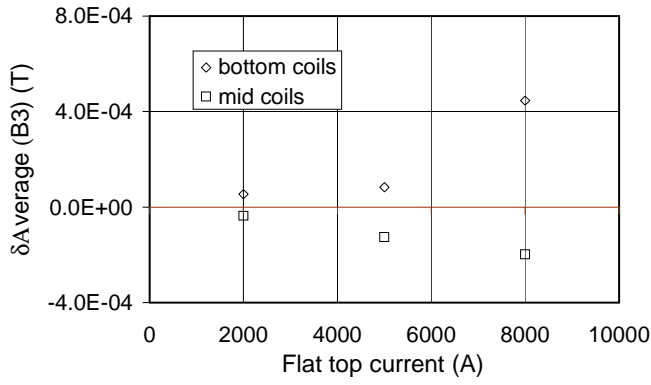


Fig. 5.21 Dependence of the average sextupole variation after 1000 s of decay on the flat top current for different ramp rates. a) 450 A/s. b) 200 A/s. c) 50 A/s.

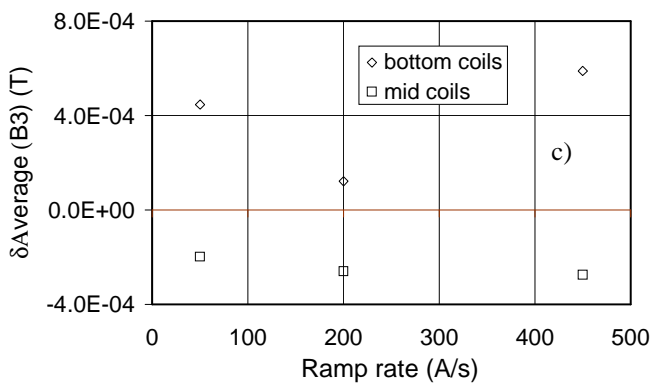
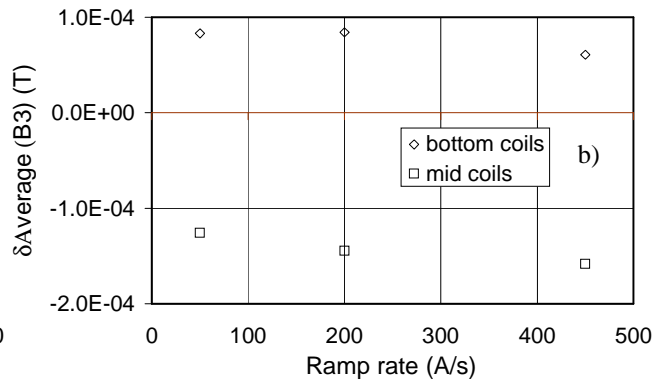
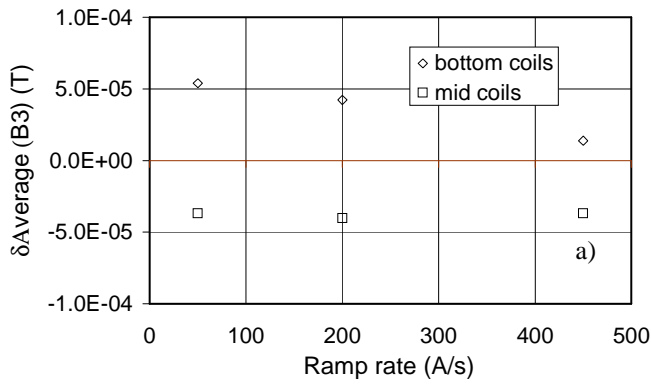


Fig. 5.22 Dependence of the average sextupole variation after 1000 s of decay on ramp rate for different flat top currents. a) 2000 A. b) 5000 A. c) 8000 A.

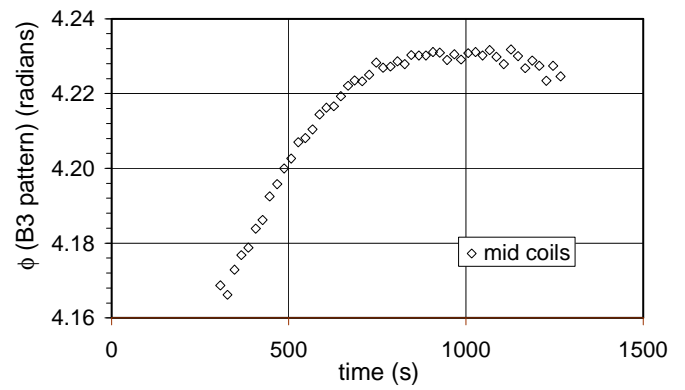
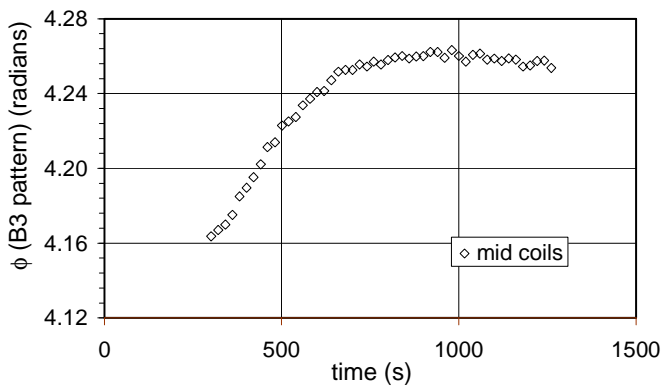
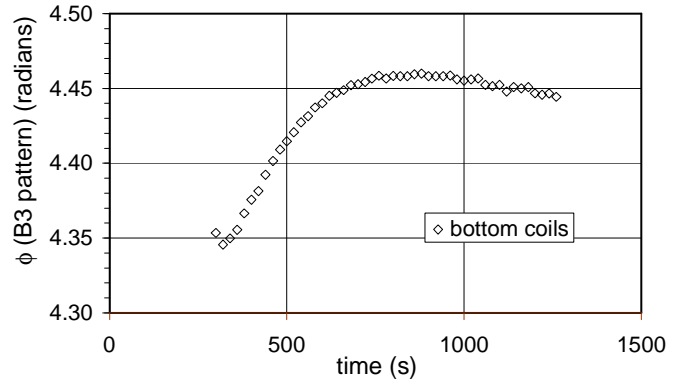
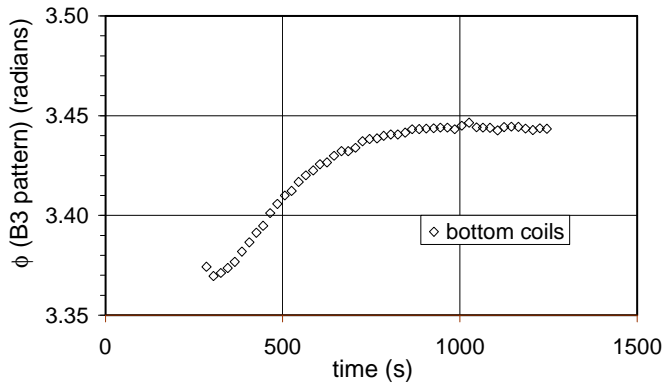


Fig. 5.23 Phase variation during flat top (2000 A, 450 A/s). a) Bottom coils. b) Mid coils.

Fig. 5.24 Phase variation during flat top

(8000 A, 450 A/s). a) Bottom coils.

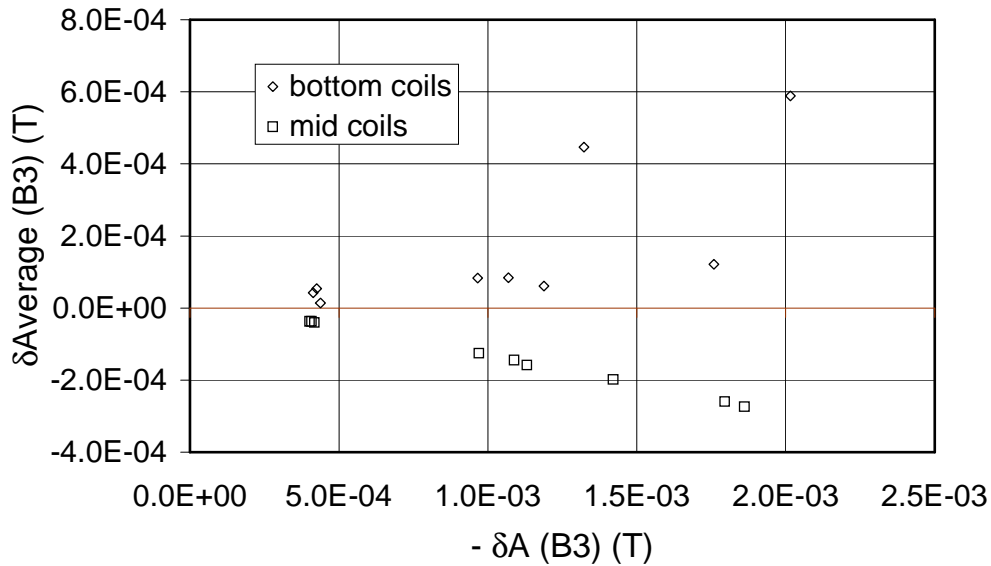


Fig. 5.25 Variation of the average normal sextupole vs variation of the amplitude (changed of sign) of the normal sextupole pattern in the first 1000 s of flat top for all the step response measurements performed.

In every real operation observe longitudinal variations the case of the step response bottom and middle part of the the sinusoidal shape of a

Amplitude of the magnetic field pattern

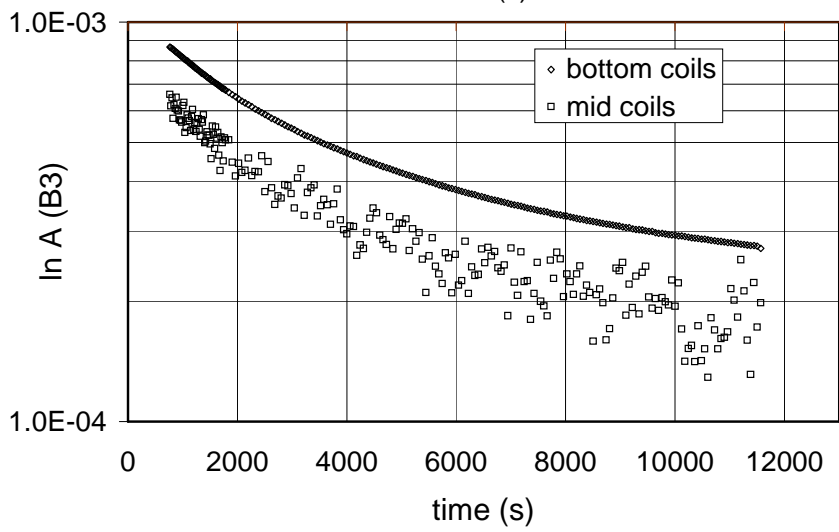
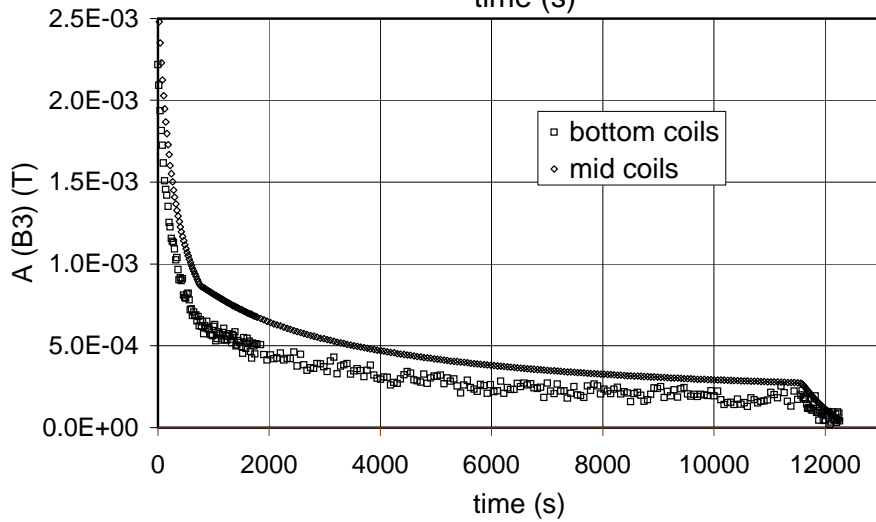
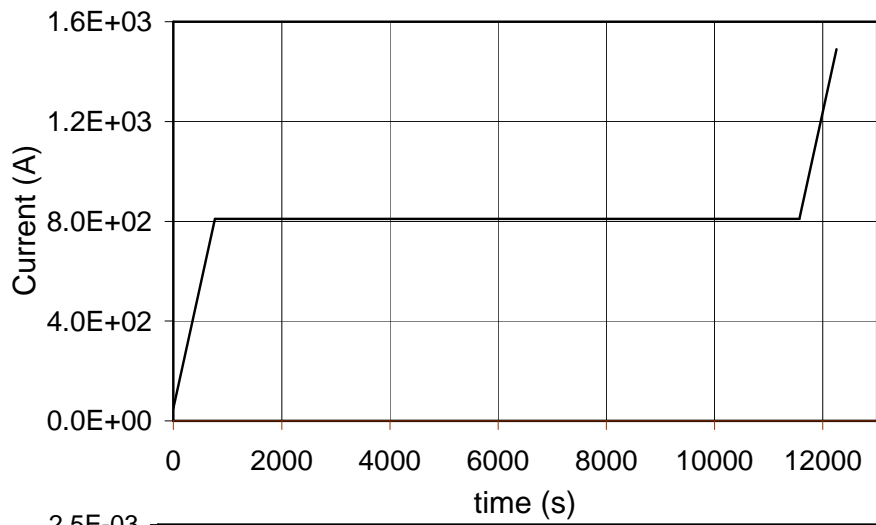
cycle measurement we of the field harmonics. As in measurements, only in the magnet these variations have periodic pattern.

The evolution in time of the sextupole pattern amplitude for the case of a flat top time $T_{FT} = 30$ min and a flat top current $I_{FT} = 11750$ A (nominal current of this dipole model) is shown in Fig. 5.26b for the bottom and middle part of the magnet. The pattern amplitude decreases during the initial ramp until the injection phase starts, in contrast to what observed during the step response runs.

As the injection phase starts, we observe a slope variation in the amplitude curve and the beginning of a slower decay of the pattern amplitude. Figure 5.26c reports a logarithmic plot of the decay phase for the longest measurement performed. This plot shows that the decay curve does not approach a straight line as in the case of the step response measurements. It seems that there is a superposition of different time constants and that the highest are so large that even with this very long measurement (12000 s of injection phase) it is not possible to reach a simple exponential regime. In shorter measurements (1000 s) the decay phase can be well fitted with an exponential curve. The time constants of these fitting curves range from 2000 to 5000 s. These time constants are larger than the measurement time and have to be considered only as characteristic times of the initial phase of the decay.

During the final ramping up, there are evident variations of the amplitude of the sextupole pattern. The variation in time of the pattern amplitude is shown in Fig. 5.27 for measurements with different pre-cycle flat top times.

Fig. 5.26 Amplitude variation in time after a pre-cycle with $T_{FT} = 30$ min, $I_{FT} = 11750$ A. a) Current sweep during measurement. b) Comparison between different positions. c) Logarithmic plot of the decay phase



The pattern amplitude behaves essentially in the same way in the two locations at the bottom and center of the magnet, and *is strongly dependent on the current cycle*.

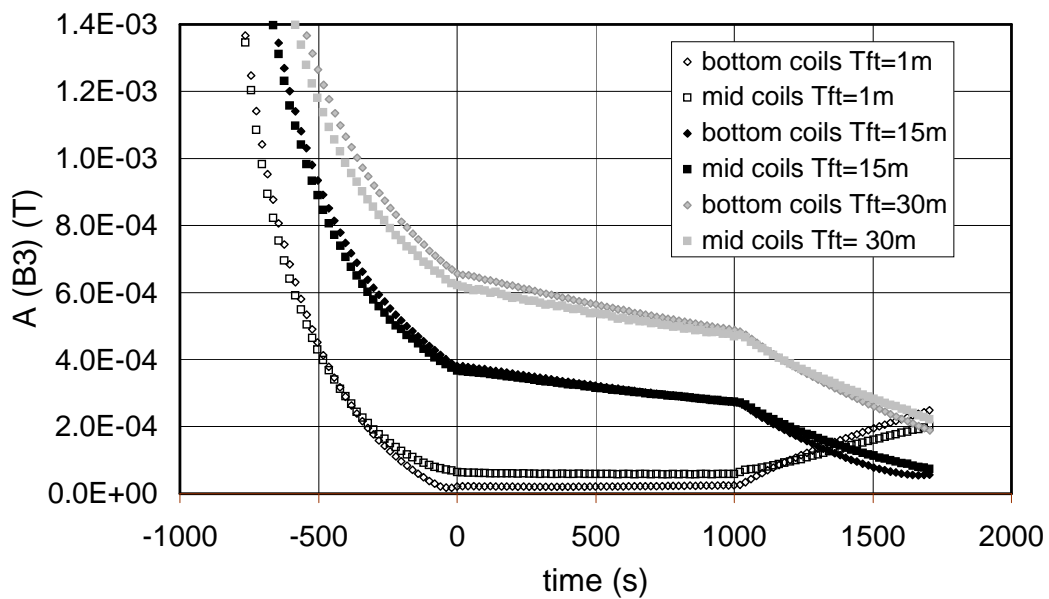
With very short flat top times the pattern has a decreasing amplitude during the initial ramp, until it disappears during the injection phase (see the curves for a 1 minute flat top time in Fig. 5.27). The periodic pattern restores during the final ramp.

In analogy to the study of the step response measurements we have estimated the pattern amplitude decay during the injection phase measured with different pre-cycles, considering the pattern amplitude variation after 1000 s from the beginning of the decay:

$$\delta A = A(t_2 + 1000 \text{ s}) - A(t_2) \tag{5.11}$$

where t_2 is the time at which injection begins.

Fig 5.27 Variation in time of the amplitude of the normal sextupole pattern after pre-cycles with different flat top times.



The time reference is set to zero at the beginning of the injection phase.

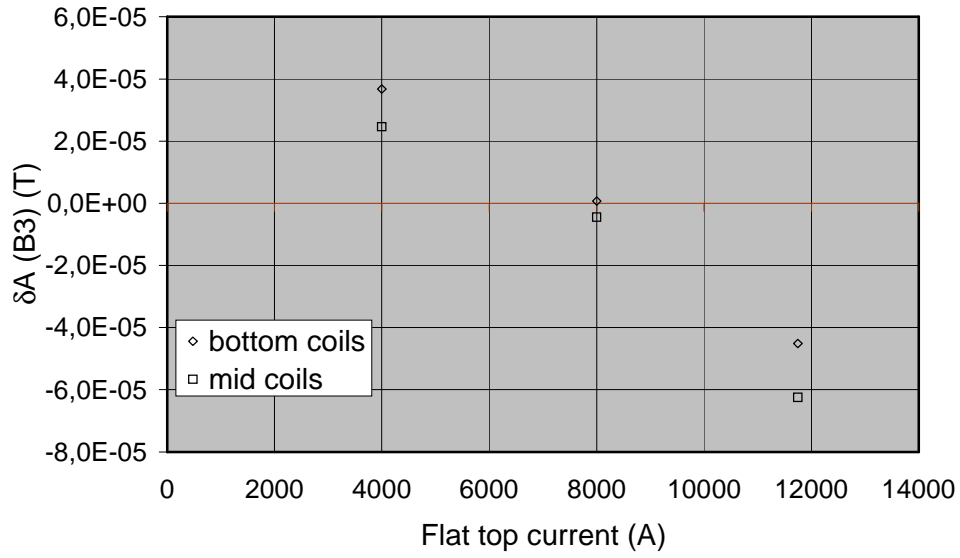


Fig. 5.28 Dependence of the amplitude variation of the normal sextupole pattern after 1000.s of constant current phase on pre-cycle flat top current.

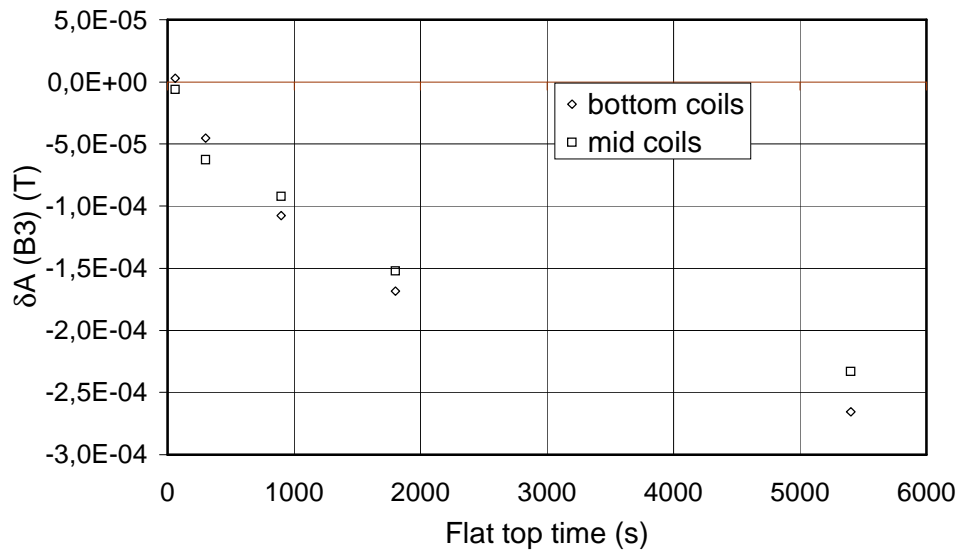


Fig. 5.29 Dependence of the amplitude variation of the normal sextupole pattern after 1000.s of constant current phase on pre-cycle flat top time.

The results show that there is a clear correlation between $\delta A(B_3)$ and both the flat top current and the flat top time. The change of sextupole pattern scales approximately linearly with the flat top current reached in the pre-cycle (see Fig. 5.28).

The scaling with the flat top time (see Fig. 5.29) in the pre-cycle can be well approximated by the following exponential function

$$\delta A = K + B \cdot \left(1 - e^{-\frac{t_{FT}}{\tau}} \right) \quad (5.12)$$

where K , B , and τ are fitting parameters and t_{FT} is the flat top time. The values of the fitting parameters are reported in Table 5.1 for different measurements.

Bottom coils	1.82	$-2.87 \cdot 10^{-4}$	$+6 \cdot 10^{-6}$
	B3	τ (* 10^3 s)	

Mid coils	1.95	$-2.36 \cdot 10^{-4}$	$-1.09 \cdot 10^{-5}$
-----------	------	-----------------------	-----------------------

Table 5.1 Fitting parameters for the dependence of the sextupole pattern amplitude variation after 1000 s from the beginning of the injection phase on the pre-cycle flat top time. The parameters are calculated by means of the fitting function (5.12).

As reported in [34], the decay of the average multipoles during injection follows the same scaling with the pre-cycle flat top time and flat top current.

Average value of the field harmonics

The normal sextupole always exhibits the same kind of variation in time, as shown in Fig. 5.30 for measurements after pre-cycles with different flat top times in the same cases reported in Fig. 5.27. At the end of the decay we observe the characteristic ‘snapback’ [34], and the following enhancement of the average value during the final ramp.

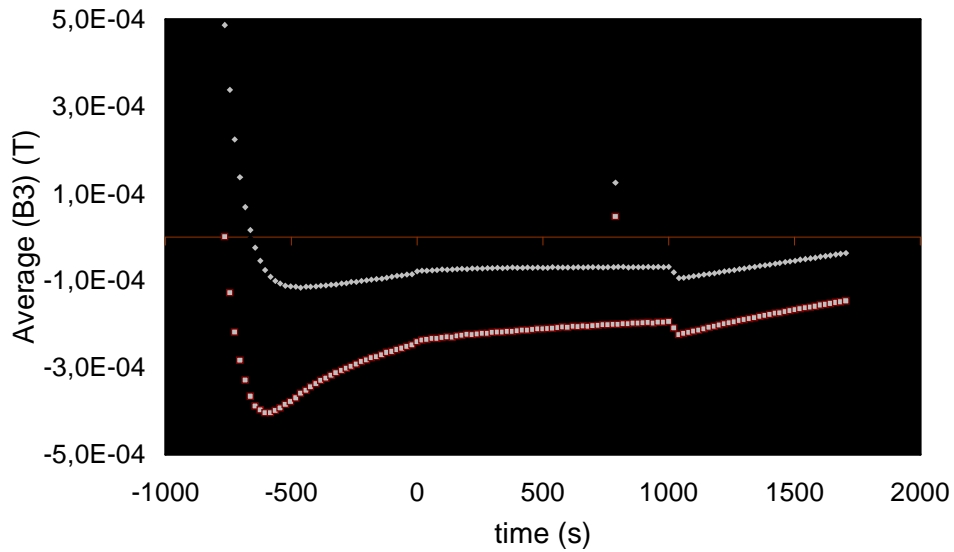


Fig 5.30 Variation in time of the average value of the normal sextupole pattern after pre-cycles with different flat top times. The time reference is set to zero at the beginning of the injection phase.

It is interesting to note that the variation of the average value of the sextupole with very short flat top times is not negligible.

This variation is not due to the relation of the current distribution with the superconductor magnetization because in this case the amplitude of the pattern is negligible. The variation may be due to the thermally activated “flux creep” occurring in the superconducting material of the cable, as already observed in [34, 68].

Phase of the modulation of the field harmonics

The variation of the initial phase of the field modulation during the operation cycle measurements is always very small. The phase variation during the injection phase of the longest measurement performed is reported in Fig. 5.31 in the bottom position of the magnet. The average translation velocity in this case is of about $9 \cdot 10^{-8}$ m/s, equivalent to 0.3 mm/h. The longitudinal displacement of the pattern is negligible.

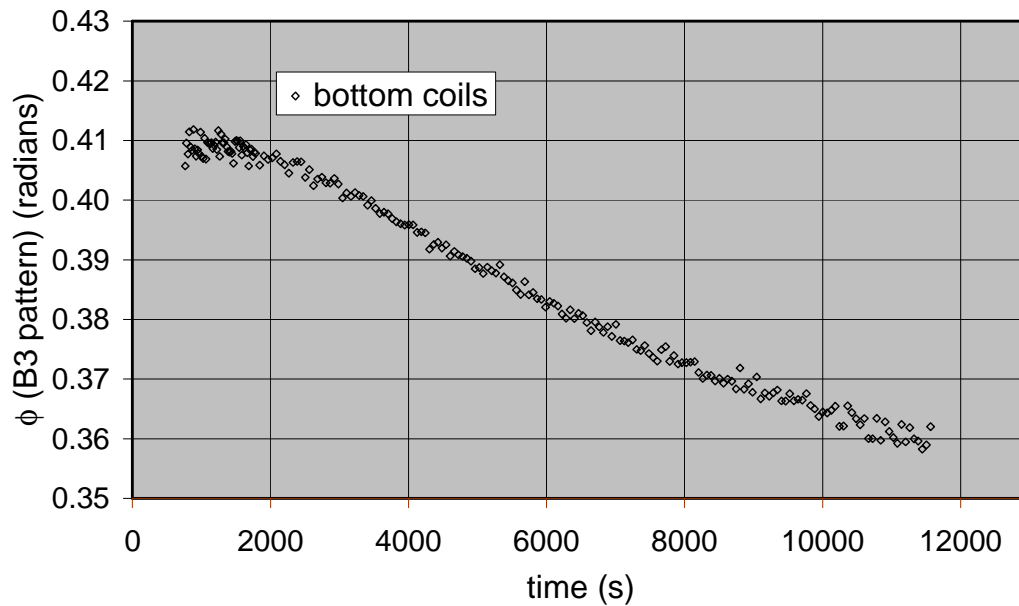


Fig 5.31 Initial phase of the sextupole pattern during the injection of the longest measurement performed (pre-cycle with $T_{FT} = 30$ min and $I_{FT} = 11750$ A).

Comparison between average and amplitude variations

The amplitude variation and the field drift exhibit a similar dependence on the pre-cycle flat top time at both positions of the magnet.

The variation of the average value is plotted in Fig. 5.32 as a function of the amplitude variation for every real operation cycle measurement.

The apparent correlation between the variation of the amplitude and the variation of the average in correspondence of the middle part of the magnet indicates that the two phenomena are indeed dependent on each other, as hypothesized in [28].

In the case of real operation cycles measurements we can exclude that the average value variation is only due to the effect of misalignment between the coil group and the sinusoidal oscillation explained in Section. 5.2.8 for the step response measurements. If that were the case, due to the linear dependence shown in eq. 5.5, we would expect the same kind of temporal evolution for the amplitude of the periodic pattern and the average value of the harmonic considered. Instead,

we note in Fig. 5.30 the characteristic snap-back of the average value, which has not any corresponding feature in the amplitude variation in the same measurements (see Fig. 5.27).

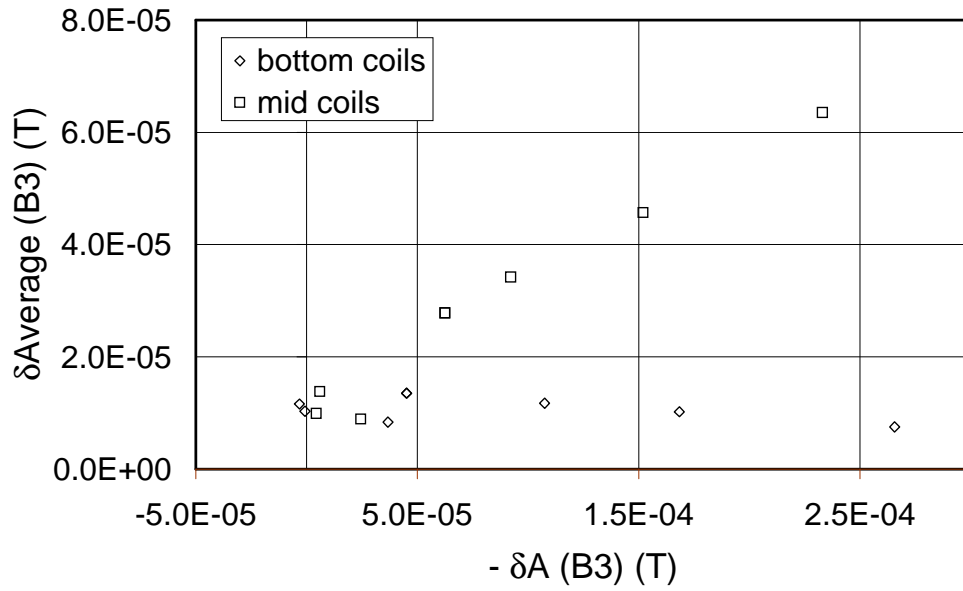


Fig. 5.32 Average delta variation versus amplitude variation (changed of sign) for all operation cycles measurements.

5.3 MODEL VALIDATION

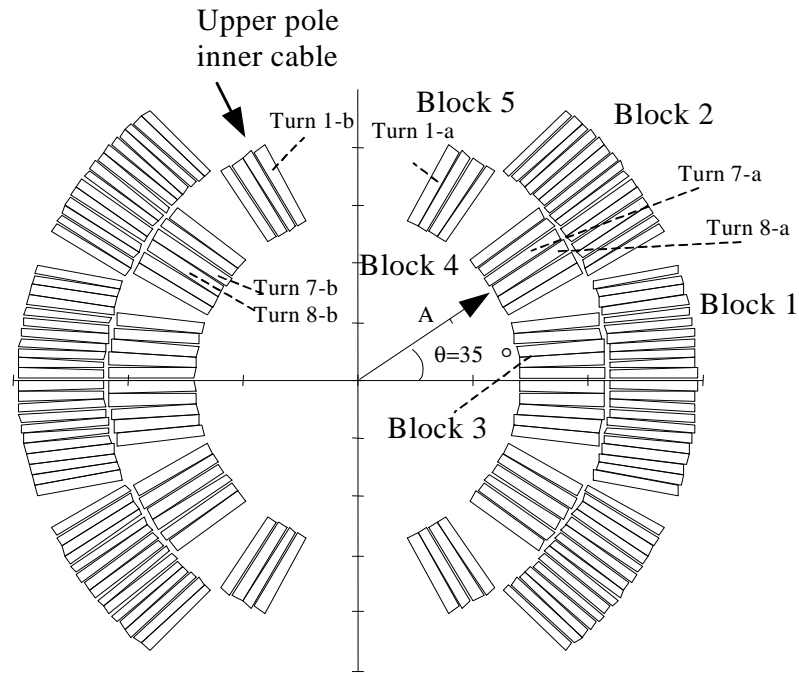


Fig. 5.33 Cross section of one aperture of the double aperture dipole model MBSMT1 used for the measurements of magnetic field pattern.

This section is dedicated to the analysis of the experimental findings described in Section 5.2. In this analysis we use both the network and the distributed parameters circuit model. The first one is based on a network approach which approximates the cable as a lumped parameters circuit. The network model (see Section 2.3.2) used in this study is that described in detail in [19].

The distributed parameters circuit model is described in Section 3.1.

5.3.1 Basic assumptions for the simulations

We postulate that the periodic magnetic field pattern is due to the long current loops circulating in the cable. In this study we consider a single cable subjected to both a current increase and, proportional to it, a non uniform time dependent magnetic field. The iron saturation at high magnetic fields is neglected. The strands of the cable are assumed to be identical, ideally transposed, and soldered to current leads via electrical resistances which are much lower than the

contact resistances of the cable. Finally, the latter are assumed to be equal, and uniform along the cable length.

Therefore, among the possible sources of non uniform current distribution listed in Section 2.1 the only source of long range current loops that we consider here is the field variation along the cable length.

A schematic view of the coil cross section of one aperture of the LHC dipole model MBSMT1 is shown in Fig. 5.33. The coil has two poles (upper and lower) assembled from an inner and an outer layer. The inner layer of a single pole is wound from 15 turns arranged into 3 blocks, while the outer layer has 26 turns arranged in 2 blocks corresponding to different angular positions. We have numbered turns and blocks as shown in Fig. 5.33.

The layers in a pole are wound individually, and the cable ends are either soldered together at the interconnection between layers and poles or connected through splices to the current leads. Because of the assumption of low splice resistance compared to the interstrand resistance in the cable, we can identify a cable unit length in a single layer (i.e. between two splices) as the shortest length to be used for analysis purposes.

In order to simulate the experimental results on the amplitude of the magnetic field pattern reported in Section 5.2, we assume that the longitudinal oscillations of the secondary field are only due to the current distribution in the inner cable of the magnet. This assumption is motivated by the fact that the periodicity of the measured oscillations of the secondary magnetic field is equal to the inner cable twist pitch.

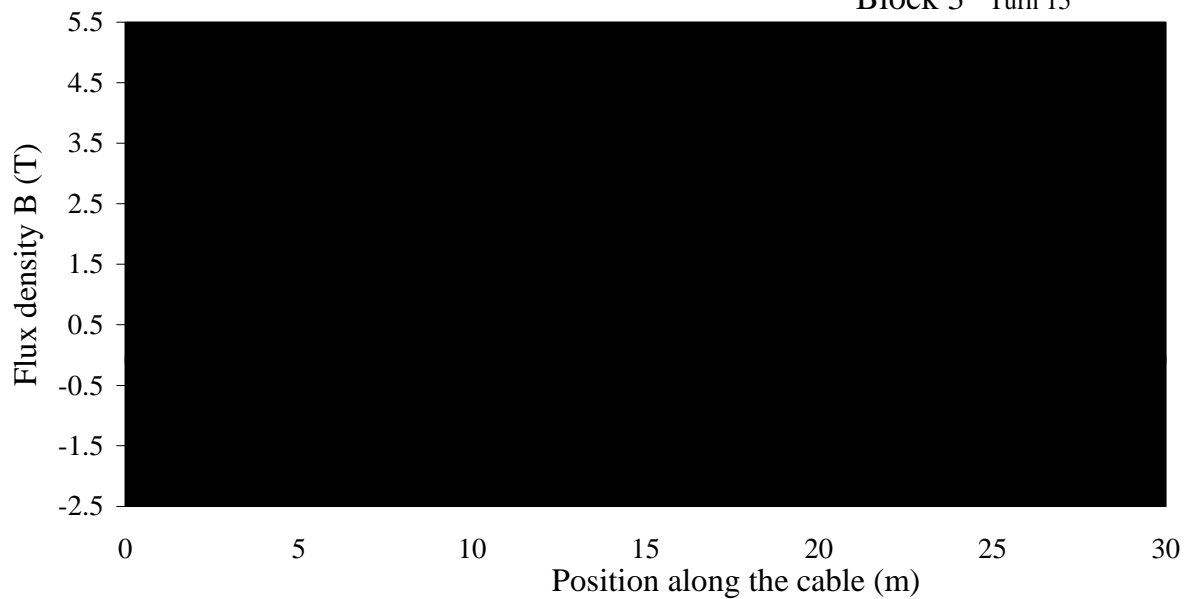


Fig. 5.34 *Magnetic flux density perpendicular to the broad face of the inner cable of the 1m long LHC dipole magnet MBSMT1. The reported field is the average field across the cable width calculated with ROXIE, at a total current of 11500 A.*

A unit length of the inner layer cable is made of 28 strands, with a total length L of 27.8 m, a twist pitch of 115 mm., and a thickness of 1.88 mm.

As we stated previously, we take spatial variations of the magnetic flux as the only source of long range current loops. The distribution of the magnetic flux density perpendicular to the broad face of the cable calculated with the computer program ROXIE [69] is shown in Fig. 5.34. We recognize two types of variations of the perpendicular field along the cable length.

Sharp, short range variations of the field are due to the cable bending over the magnet bore, while step changes in the value of the field along the straight part of the cable correspond to the transitions from block to block.

We have performed two sets of simulations using either the network or the continuum model, in order to imitate the cable excitation with current cycles made of a linear ramp up followed by a current plateau as were performed in the experiments reported in the previous section.

Simulations with the network model are aimed to look at the fine details of the origination of the short and long range eddy currents. The size of the network model grows quickly with the length of cable analyzed. For this reason we limited the simulations to a short length of cable to explore general features of the transient response of the long range current loops to field changes.

We have then performed simulations of the whole cable response to current steps with the distributed parameters model. This model does not reproduce accurately the details, but is suitable for the simulation of a full cable length in a magnet.

In both sets of simulations we have varied parametrically the flat top current and the ramp rate in order to study their influence on the current distribution.

5.3.2 *Network model*

The simulations using the network model have been focussed at an ideal cable close to the coil midplane. In order to minimize the computation time, a four strand cable has been considered. The cable length L is equal to approximately 23 twist pitches. We have assumed a symmetric magnetic field distribution along half of the cable length, shown in Fig. 5.35. The magnetic field is zero at the cable ends and at its center. In between, there are regions of uniform magnetic field. The magnetic field is twice as high at the inner edge of the cable as at the outer one.

This geometry imitates a complete turn in a dipole magnet, where the uniform field regions represent the straight length of the magnet included between the low field regions at the magnet ends.

Let us consider elemental current cycles made of a ramp up followed by a current plateau. Let also the plateau current be much less than the critical current. The results of simulations show that soon after the beginning of the cycle eddy currents associated with the local value of dB/dt appear.

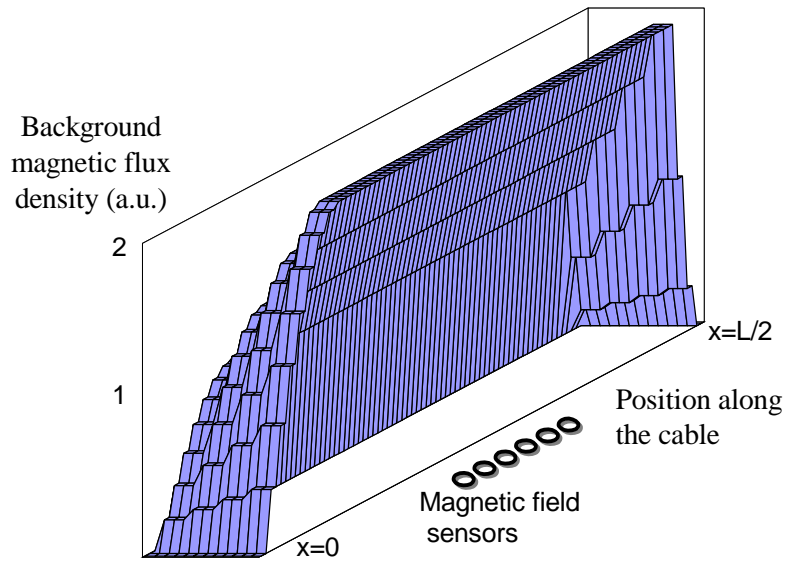


Fig 5.35 Magnetic flux density perpendicular to the broad face of the ideal cable considered for the simulations performed with the network model.

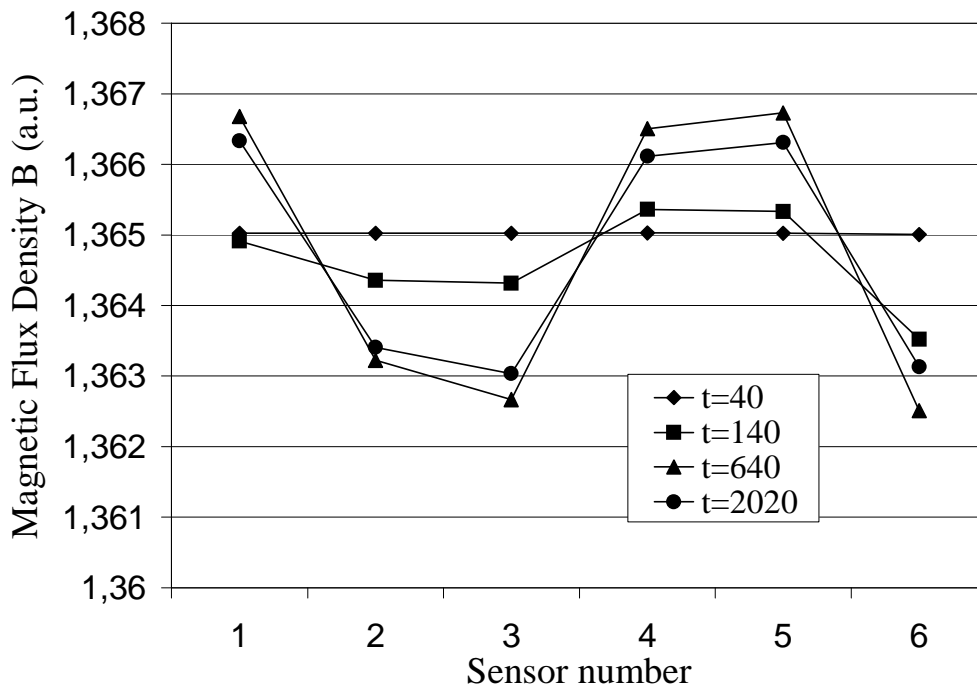


Fig. 5.36 Development of magnetic field pattern in the uniform field region

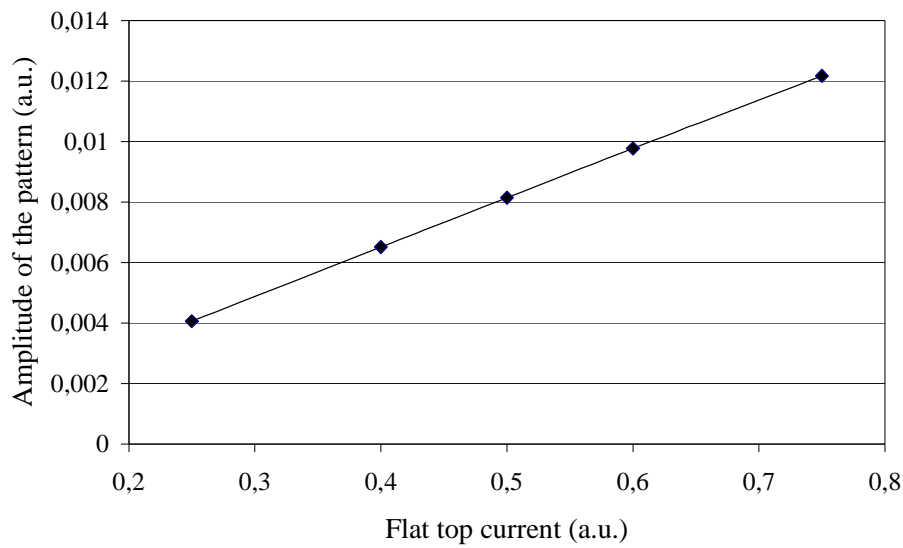


Fig. 5.37 Dependence of the amplitude of the magnetic field pattern on the flat top current at the end of the ramp.

These eddy currents produce a uniform field in the neighborhood of the cable, without any periodic oscillation. Gradually, however, the strand currents become different in the ends of the cable, where the magnetic field has a longitudinal gradient, thus originating current loops.

As time advances, the current in these loops diffuses from the cable end regions into the center. The time t_p needed to complete this process is much higher than the time of development of uniform, short range eddy currents.

The buildup and following decay of a periodic magnetic field pattern is shown in Fig. 5.36. The amplitude of the pattern increases at $t < t_p$ and decreases afterwards.

Calculations show that if the time of the ramp is short compared to t_p , the amplitude of the periodic magnetic field pattern on the plateau at a certain moment, $t > t_p$ does not depend on the ramp rate, while it is linearly dependent on the flat top current (see Fig. 5.37).

5.3.3 Distributed parameters model

We have performed calculations with the continuum model for a cable made of 28 strands, as in reality, and with a cable composed of 8 *equivalent* superstrands.

In accordance with measured value in the dipole model MBSMT1, we have taken a contact resistance between strands in the range 10 to 20 $\mu\Omega$ per contact.

We have used the magnetic field map shown in Fig. 5.34 as an input for the calculation, scaling the field proportionally to the current in the magnet. In the simulations performed with the continuum model we have neglected the field variations across the cable width. This, as demonstrated in the detailed analysis discussed in the previous section, is inessential for the development of long range current loops.

The results of simulations are reported in Fig. 5.38 for a current step with a ramp rate of 50 A/s and a final current of 2000 A. It can be noticed that soon after the beginning of the ramp sharp current spikes appear in these regions of high field gradient (Fig. 5.38a). At the end of the field ramp the correspondence between the field profile and the current pattern is less evident (Fig. 5.38b). After 1000 s from the beginning of the current flat top, we note a remarkable current difference between the strand currents, but the correspondence with the field profile is lost (Fig. 5.38c).

As we have postulated that the magnetic field pattern is due to long current loops circulating in the cable, it is reasonable to assume that its amplitude is proportional to the difference between the currents flowing in the strands. In particular we have taken the values of the maximum difference between the strand currents in the middle of the uniform field regions, ΔI_{max} , as the reference quantity for a qualitative comparison with the amplitude of the magnetic field pattern measured outside the cable and next to these positions.

As an example we compare in Fig. 5.39 the amplitude of the total magnetic field pattern at position A ($r = 17$ mm and $\theta = 35^\circ$) to the parameter ΔI_{max} calculated for turn 7-a which faces the point selected. The amplitude of the total field pattern has been reconstructed at point A from the

data presented in Section 5.2, obtained with the rotating coils placed in the middle of the straight length of the magnet. The comparison is shown for a step response measurement with $I_{FT} = 2000\text{A}$ and $RR = 50 \text{ A/s}$. We have performed the simulations with the complete 28 strands cable, for different values of the cross contact resistances (10 and 20 $\mu\Omega$).

The value of ΔI_{max} at the end of the ramp calculated in four consecutive straight parts of the cable (turns 7-8, see Fig. 5.33) is shown in Fig. 5.40 for the case of $RR = 450 \text{ A/s}$. These simulations have been performed with the equivalent, 8 superstrands cable for the whole set of ramp rates and flat top currents considered in the experiments, and the results confirm that the amplitude of ΔI_{max} at the end of the ramp is proportional to the flat top current and approximately independent on the ramp rate, as obtained in the experiments and with the network model.

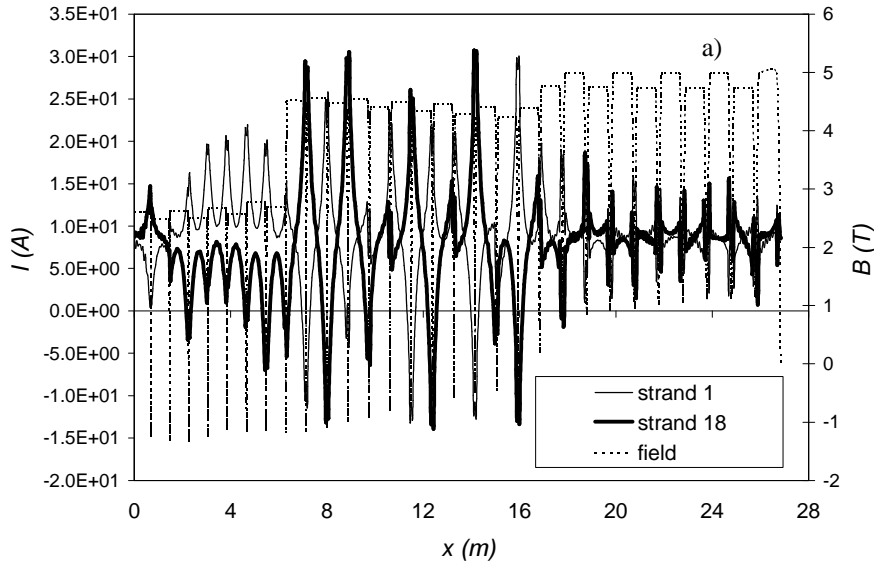
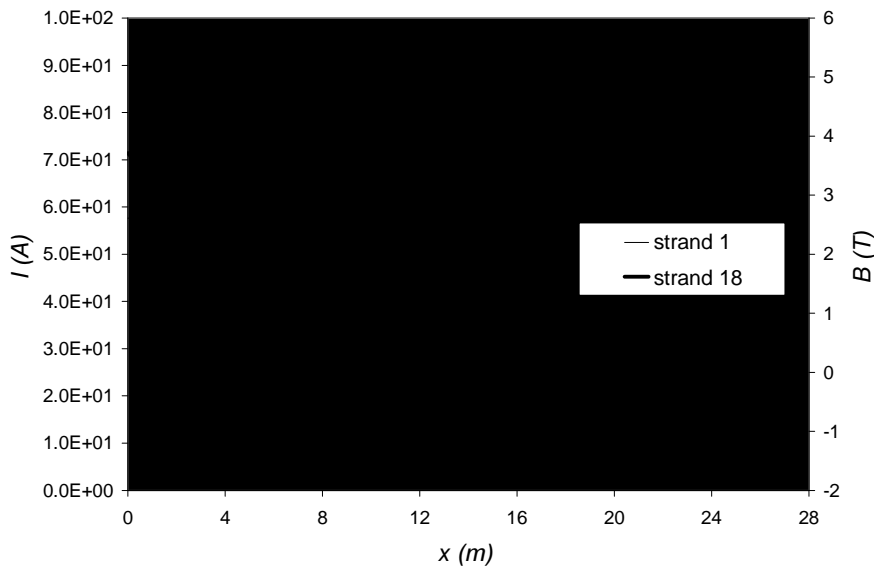
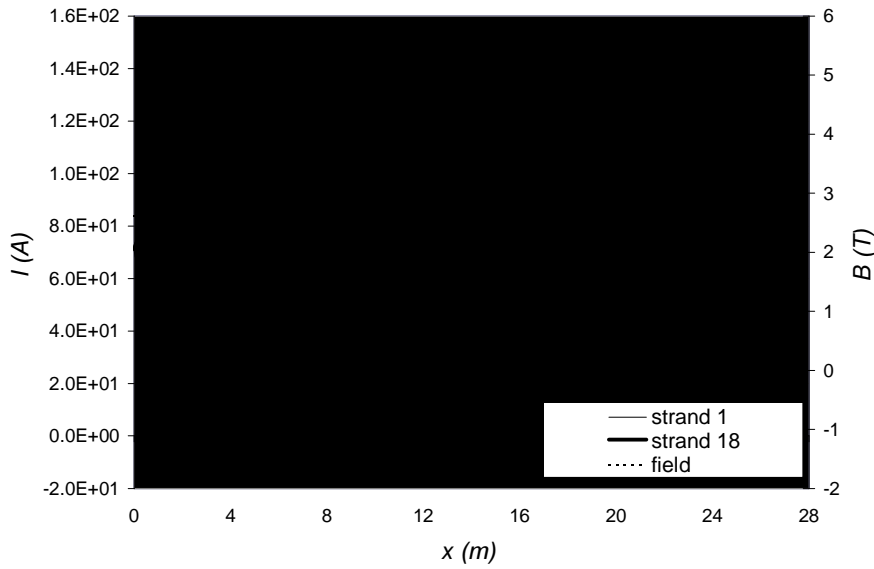


Fig. 5.38 Behaviour of the currents in two strands of the 28 strand cable along the cable length at different times. $RR = 50$ A/s $I_{FT} = 2000$ A a) $t = 3.85$ s (soon after ramp start) b) $t = 39$ s (end of the ramp) c) $t = 1039$ s (end of the plateau). The dotted line indicates the main background magnetic field perpendicular to the cable axis calculated at $i_{OP} = 11500$ A.



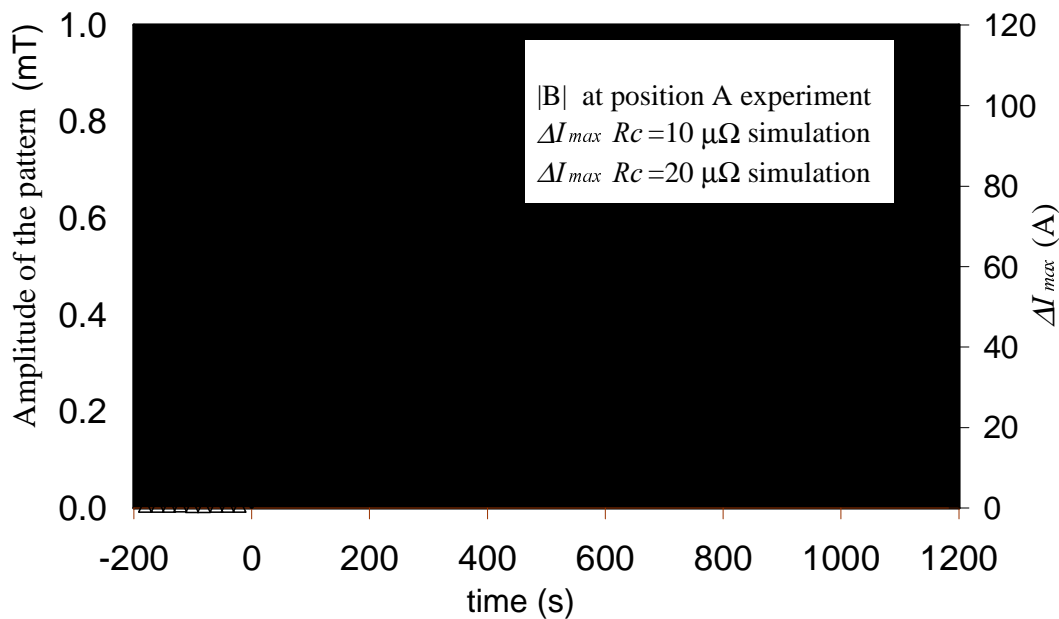
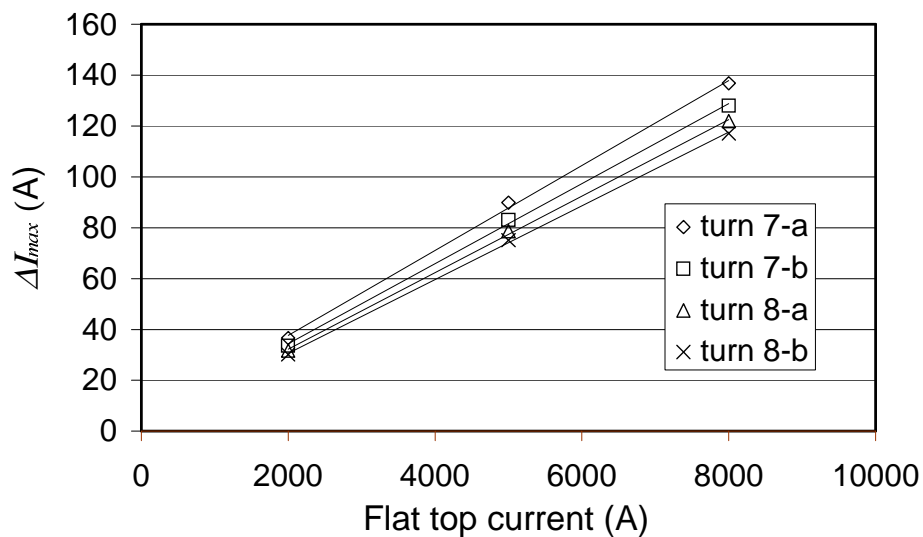


Fig. 5.39 Comparison between the time evolution of the amplitude of the periodic pattern in the middle of the uniform field region and that of parameter ΔI_{max} calculated at turn 7-a. Time t is set to zero at the beginning of the current step, made of a linear increase up to 2000 A with a ramp rate of 50 A/s and a flat top of 1000 s at the maximum current.

Fig 5.40 Dependence of parameter ΔI_{max} on the final flat top current in different cable turns (RR=450 A/s)



The temporal Average value of the field harmonics evolution of the average harmonics over the two coil groups mid and bottom [see definition (5.3)] is shown in Fig. 5.19 for the step response measurement with a 2000 A flat top current and a 450 A/s ramp rate and in Fig. 5.20 for the step response measurement with 8000 A flat top current and 450 A/s ramp rate. The variation in time is different for the two positions in the magnet, but each kind of pattern is repeated in different experiments.

The average in the mid coil measurements always decreases during the constant current phase, while in the bottom coil measurements it always increases. The variation of the average value after 1000 s from the beginning of the flat top phase has been taken as a parameter to compare different experiments. The plot of this parameter versus the flat top current and the ramp rate is shown in Figs. 5.21 and 5.22 respectively.

In the case of the mid coil measurements we can observe that the variation of the average is approximately linear with the final current, and constant with the ramp rate.

Phase of the modulation

The variation in time of the phase φ of the normal sextupole pattern is shown in Figs. 5.23 and 5.24 for the same measurements reported in Figs. 5.19 and 5.20. We have found the same kind of phase variation in every measurement. We observe that the maximum change of the phase of the sinusoidal fit of the measured data is approximately equal to 0.1 radians during a total time of 1000 s. The phase shift of the sinusoidal pattern is equivalent to a translational movement of the pattern along the magnet axis. The average linear velocity of this translation can be calculated as follows:

$$v_t = \frac{\Delta\varphi}{\Delta t} \cdot \frac{L_p}{2\pi} \quad (5.6)$$

where v_t is the translational velocity and $\Delta\varphi$ the total phase variation.

We obtain an average velocity of about $1.8 \cdot 10^{-6}$ m/s, equivalent to 6.6 mm/h. This value is negligible, also considering that in the final part of the decay the phase variation in time is slower than in the initial part.

Comparison between average and amplitude variations

Considering the measurements referred to the middle part of the magnet, we note that the same dependence on the final current and on the ramp rate is shown by the variation of the amplitude of the sextupole pattern after 1000 s of decay and by the variation of the average over the mid coil group in the same time interval. These variations are in fact linearly dependent on the final current and independent of the ramp rate. The variation of the average is in all cases in the range from 10 to 15% of the variation of the amplitude of the periodic pattern (see Fig. 5.25).

The variation of the average could be due to the mismatch between the total length covered by the measurement coils and the inner cable twist pitch. The integral of the sinusoidal variation over this region contributes to the determination of the average value and depends linearly on the value of the amplitude of the sinusoidal curve. The highest possible variation of the average value is found when one border of the region covered by the coils happens to be aligned with a zero of the sinusoidal variation. In this case the measured average (indicated as \bar{h}_{meas}) can be expressed by the following equation:

$$\bar{h}_{meas} = \bar{h}_{real} + \bar{h}_{err} \quad (5.7)$$

where \bar{h}_{real} is the real value of the average and \bar{h}_{err} is the error due to the misalignment. The error is given by the following expression:

$$\delta \bar{h}_{err} = \int_0^{L_{co}-L_p} A \sin\left(\frac{2\pi z}{L_p}\right) dz = A \left(1 - \cos\left(\frac{2\pi(L_{co}-L_p)}{L_p}\right)\right) \quad (5.8)$$

where L_{co} is the length of the region covered by the coils array. The variations in time of the measured values of the average are given by:

$$\delta \bar{h}_{ea} = \delta \bar{h}_{real} + \delta \bar{h}_{err} \quad (5.9)$$

In the case of the mid coils array the relation between the variations in time of the average and of the amplitude due to the quoted misalignment is given by:

$$\delta \bar{h}_{err} = 0.32 \delta A \quad (5.10)$$

The average delta is always lower than 30% of the amplitude delta, so that the measured drift could be due to this effect.

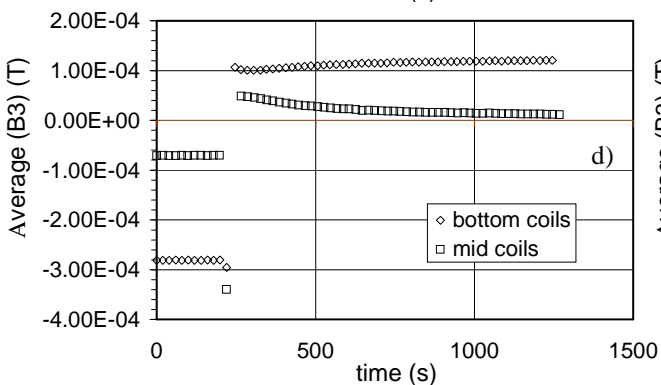
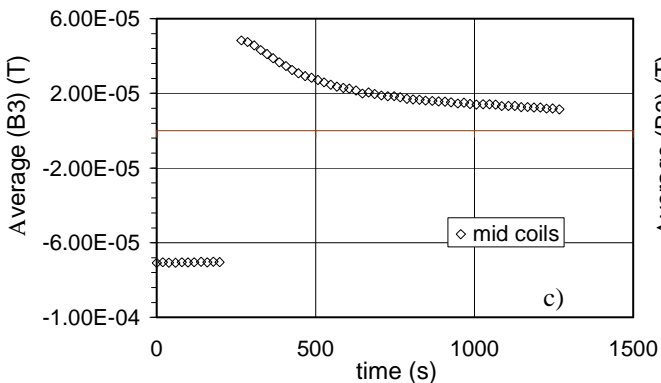
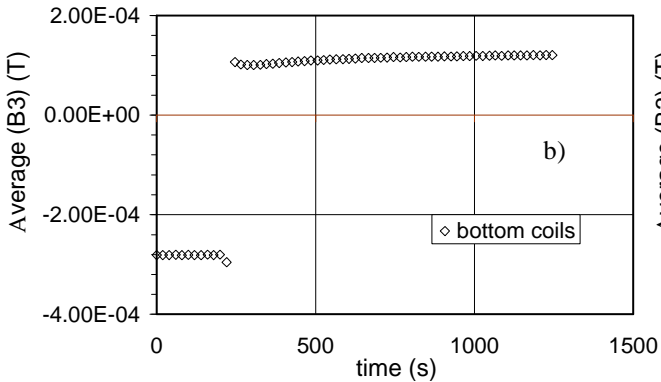
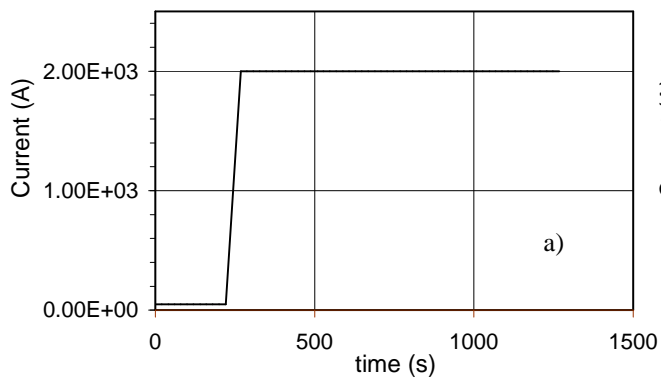


Fig. 5.19 Average variation in time (2000 A, 450 A/s). a) Current sweep. b) Bottom coil measurements. c) Mid coil measurements. d) Comparison between different positions.

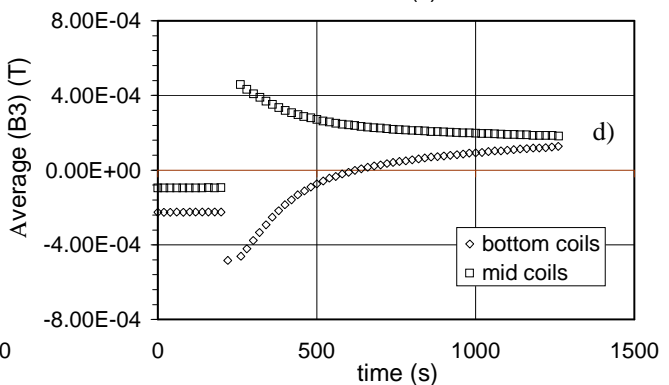
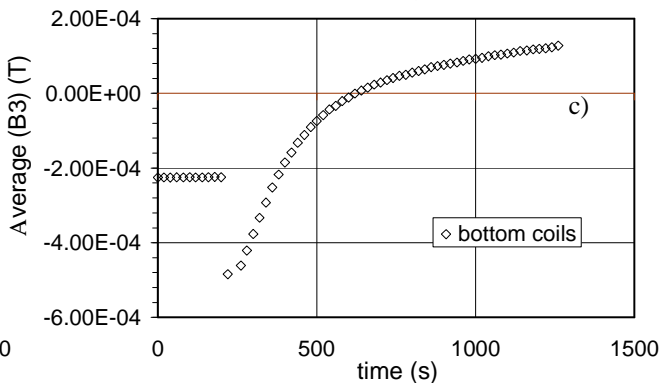
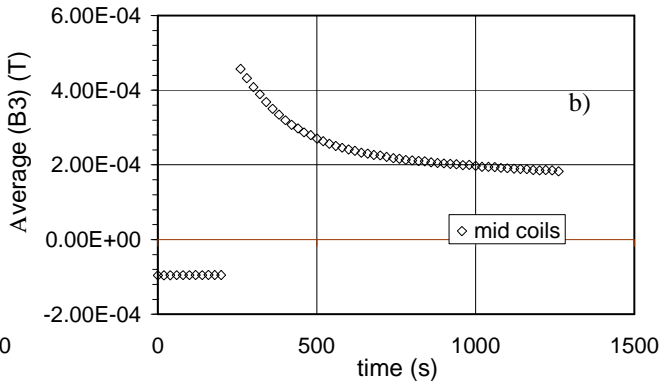
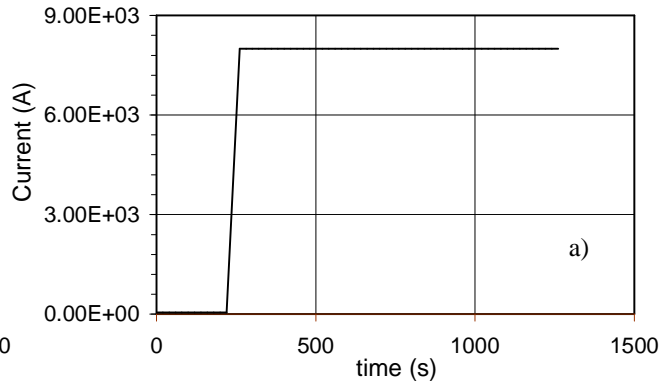


Fig. 5.20 Average variation in time (8000 A, 450 A/s). a) Current sweep. b) Bottom coil measurements. c) Mid coil measurements. d) Comparison between different positions.

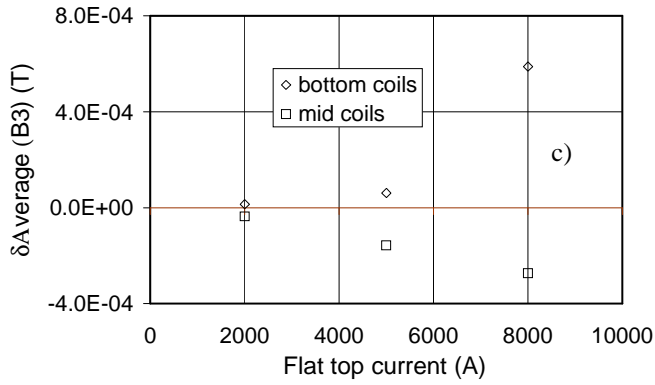
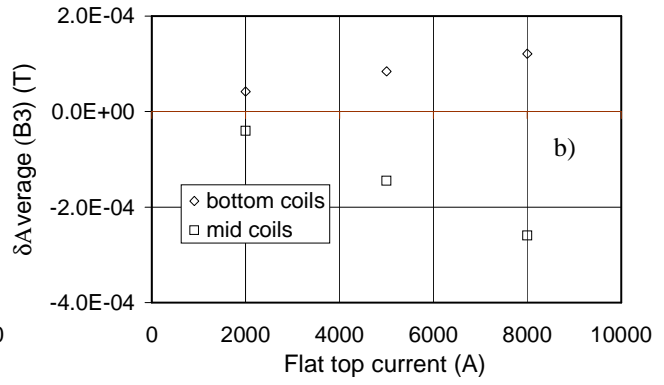
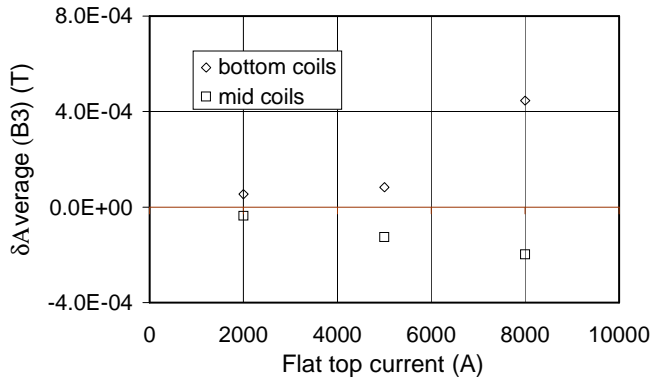


Fig. 5.21 Dependence of the average sextupole variation after 1000 s of decay on the flat top current for different ramp rates. a) 450 A/s. b) 200 A/s. c) 50 A/s.

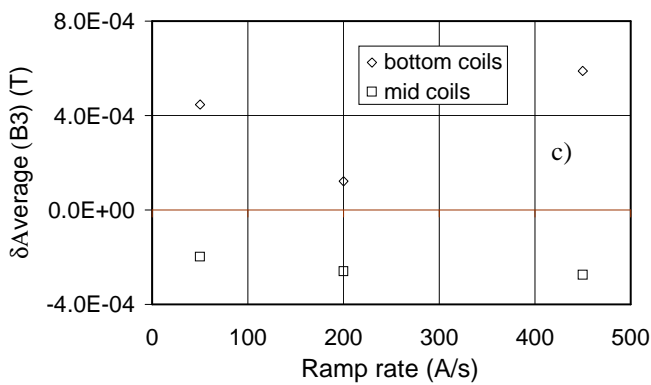
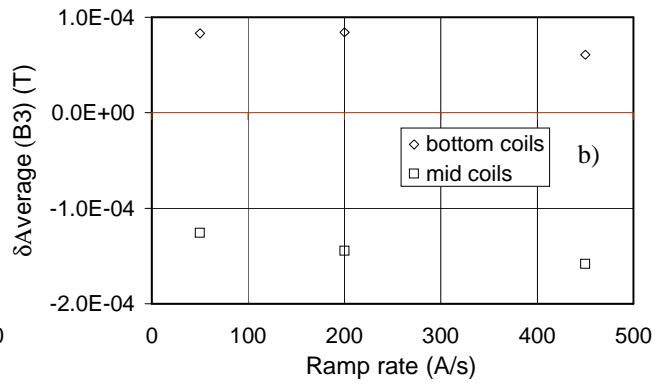
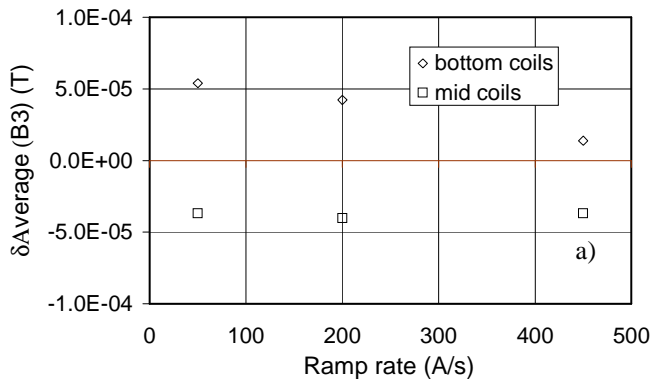


Fig. 5.22 Dependence of the average sextupole variation after 1000 s of decay on ramp rate for different flat top currents. a) 2000 A. b) 5000 A. c) 8000 A.

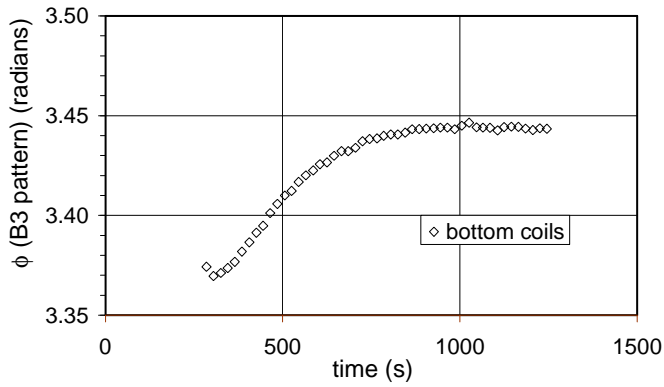


Fig. 5.23 Phase variation during flat top (2000 A, 450 A/s). a) Bottom coils. b) Mid coils.

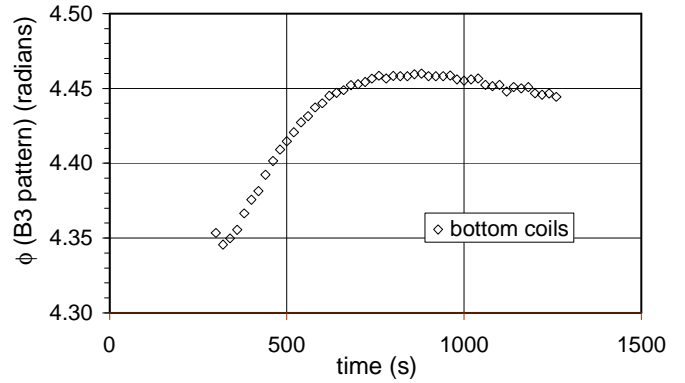
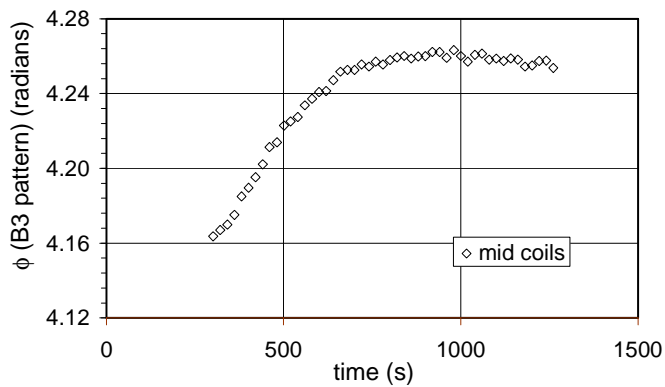


Fig. 5.24 Phase variation during flat top

(8000 A, 450 A/s). a) Bottom coils.

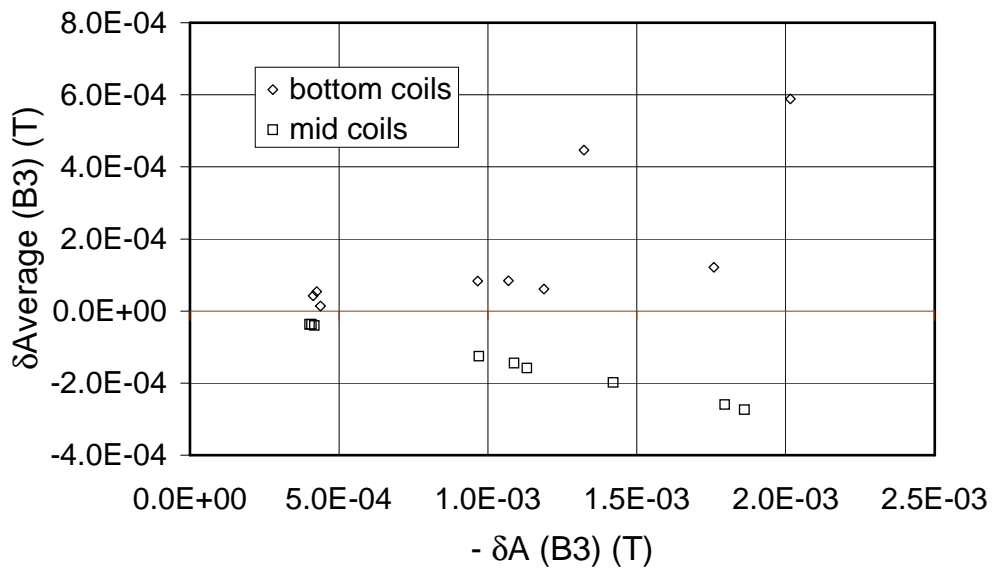
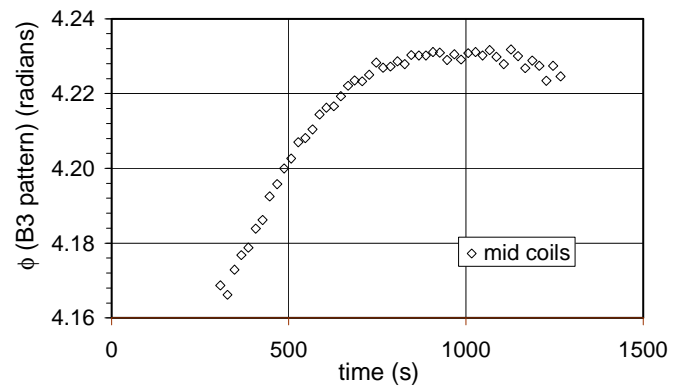


Fig. 5.25 Variation of the average normal sextupole vs variation of the amplitude (changed of sign) of the normal sextupole pattern in the first 1000 s of flat top for all the step response measurements performed.

In every real operation observe longitudinal variations the case of the step response bottom and middle part of the the sinusoidal shape of a

Amplitude of the magnetic field pattern

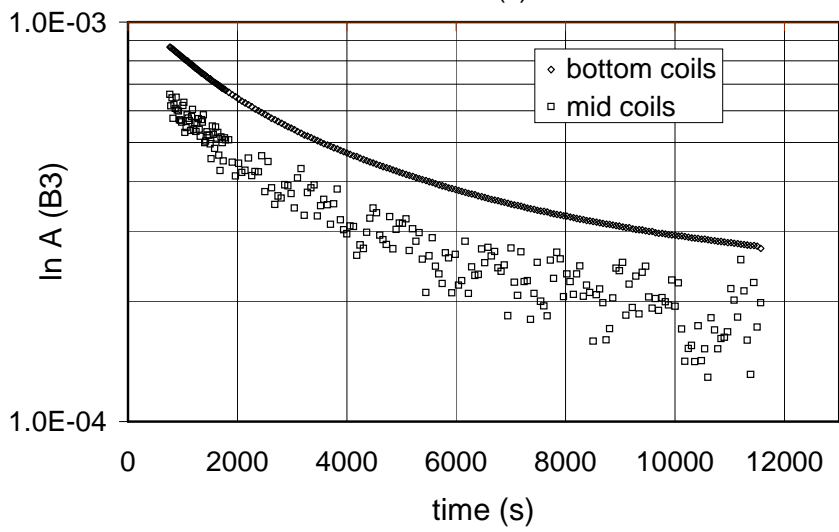
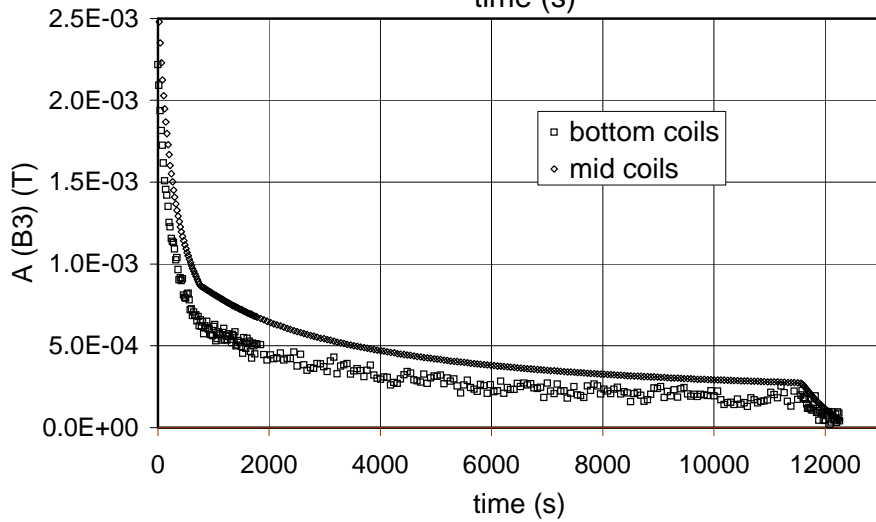
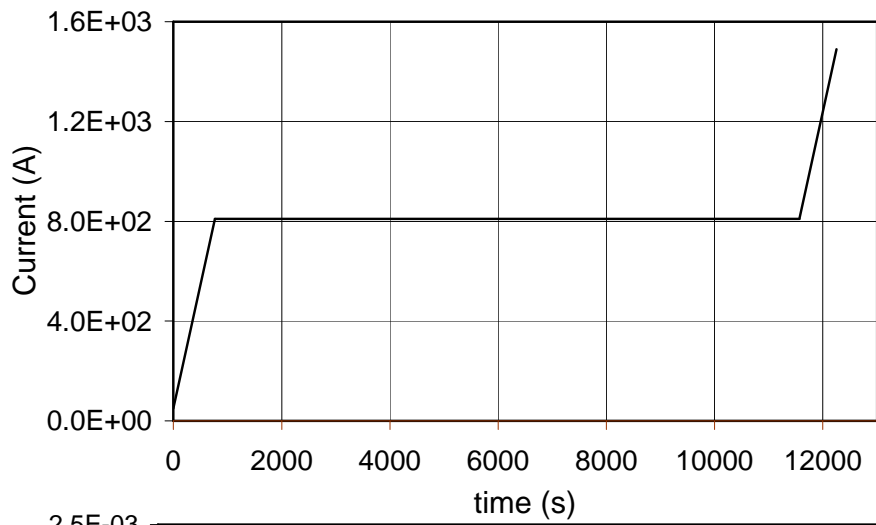
cycle measurement we of the field harmonics. As in measurements, only in the magnet these variations have periodic pattern.

The evolution in time of the sextupole pattern amplitude for the case of a flat top time $T_{FT} = 30$ min and a flat top current $I_{FT} = 11750$ A (nominal current of this dipole model) is shown in Fig. 5.26b for the bottom and middle part of the magnet. The pattern amplitude decreases during the initial ramp until the injection phase starts, in contrast to what observed during the step response runs.

As the injection phase starts, we observe a slope variation in the amplitude curve and the beginning of a slower decay of the pattern amplitude. Figure 5.26c reports a logarithmic plot of the decay phase for the longest measurement performed. This plot shows that the decay curve does not approach a straight line as in the case of the step response measurements. It seems that there is a superposition of different time constants and that the highest are so large that even with this very long measurement (12000 s of injection phase) it is not possible to reach a simple exponential regime. In shorter measurements (1000 s) the decay phase can be well fitted with an exponential curve. The time constants of these fitting curves range from 2000 to 5000 s. These time constants are larger than the measurement time and have to be considered only as characteristic times of the initial phase of the decay.

During the final ramping up, there are evident variations of the amplitude of the sextupole pattern. The variation in time of the pattern amplitude is shown in Fig. 5.27 for measurements with different pre-cycle flat top times.

Fig. 5.26 Amplitude variation in time after a pre-cycle with $T_{FT} = 30$ min, $I_{FT} = 11750$ A. a) Current sweep during measurement. b) Comparison between different positions. c) Logarithmic plot of the decay phase



The pattern amplitude behaves essentially in the same way in the two locations at the bottom and center of the magnet, and *is strongly dependent on the current cycle*.

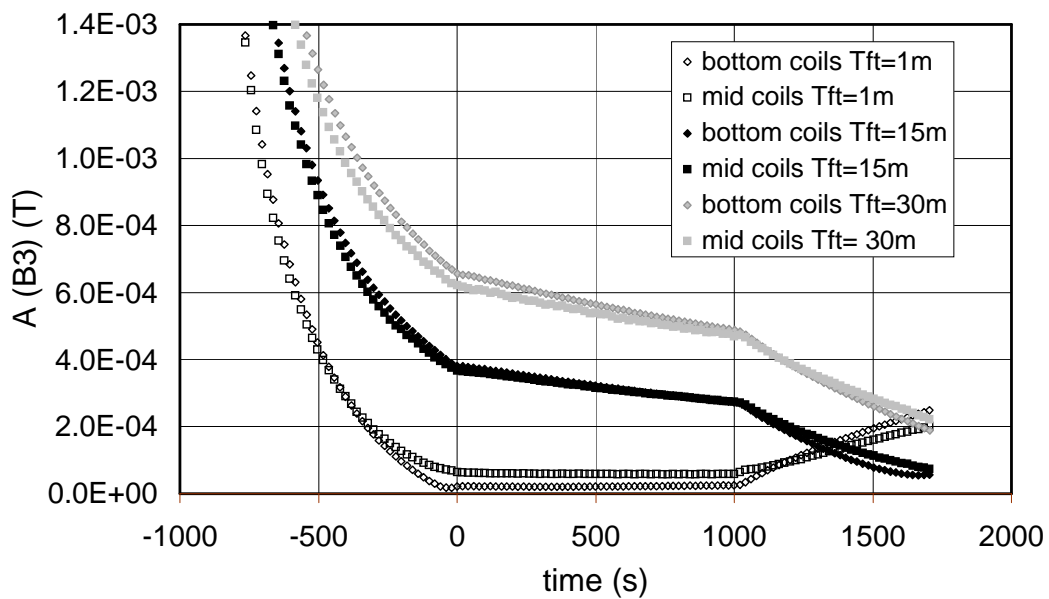
With very short flat top times the pattern has a decreasing amplitude during the initial ramp, until it disappears during the injection phase (see the curves for a 1 minute flat top time in Fig. 5.27). The periodic pattern restores during the final ramp.

In analogy to the study of the step response measurements we have estimated the pattern amplitude decay during the injection phase measured with different pre-cycles, considering the pattern amplitude variation after 1000 s from the beginning of the decay:

$$\delta A = A(t_2 + 1000 \text{ s}) - A(t_2) \tag{5.11}$$

where t_2 is the time at which injection begins.

Fig 5.27 Variation in time of the amplitude of the normal sextupole pattern after pre-cycles with different flat top times.



The time reference is set to zero at the beginning of the injection phase.

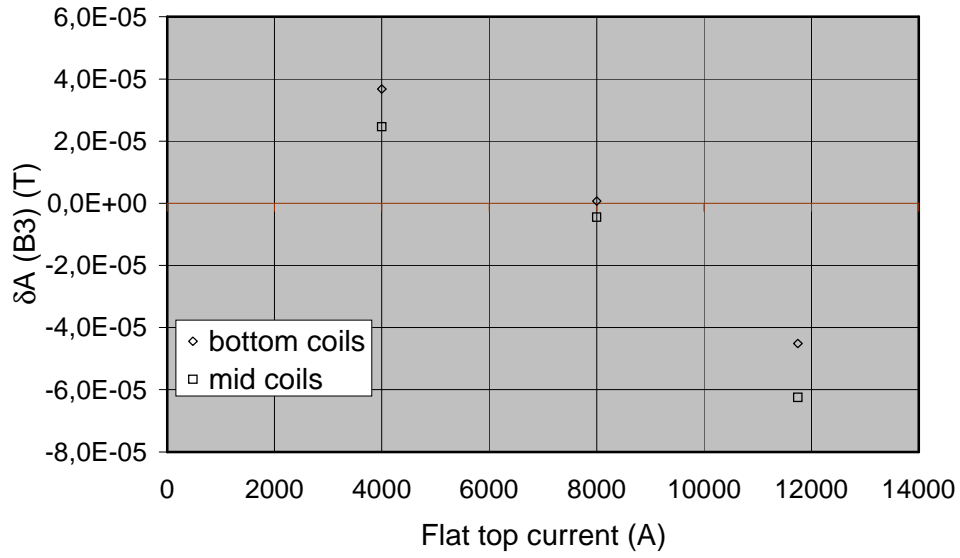


Fig. 5.28 Dependence of the amplitude variation of the normal sextupole pattern after 1000.s of constant current phase on pre-cycle flat top current.

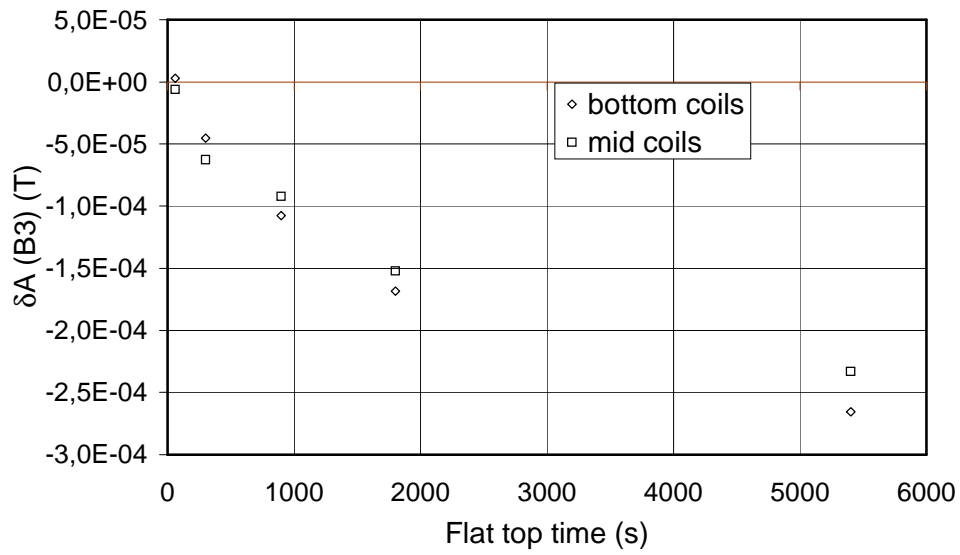


Fig. 5.29 Dependence of the amplitude variation of the normal sextupole pattern after 1000.s of constant current phase on pre-cycle flat top time.

The results show that there is a clear correlation between $\delta A(B_3)$ and both the flat top current and the flat top time. The change of sextupole pattern scales approximately linearly with the flat top current reached in the pre-cycle (see Fig. 5.28).

The scaling with the flat top time (see Fig. 5.29) in the pre-cycle can be well approximated by the following exponential function

$$\delta A = K + B \cdot \left(1 - e^{-\frac{t_{FT}}{\tau}} \right) \quad (5.12)$$

where K , B , and τ are fitting parameters and t_{FT} is the flat top time. The values of the fitting parameters are reported in Table 5.1 for different measurements.

Bottom coils	1.82	$-2.87 \cdot 10^{-4}$	$+6 \cdot 10^{-6}$
	B3	τ (* 10^3 s)	

Mid coils	1.95	$-2.36 \cdot 10^{-4}$	$-1.09 \cdot 10^{-5}$
-----------	------	-----------------------	-----------------------

Table 5.1 Fitting parameters for the dependence of the sextupole pattern amplitude variation after 1000 s from the beginning of the injection phase on the pre-cycle flat top time. The parameters are calculated by means of the fitting function (5.12).

As reported in [34], the decay of the average multipoles during injection follows the same scaling with the pre-cycle flat top time and flat top current.

Average value of the field harmonics

The normal sextupole always exhibits the same kind of variation in time, as shown in Fig. 5.30 for measurements after pre-cycles with different flat top times in the same cases reported in Fig. 5.27. At the end of the decay we observe the characteristic ‘snapback’ [34], and the following enhancement of the average value during the final ramp.

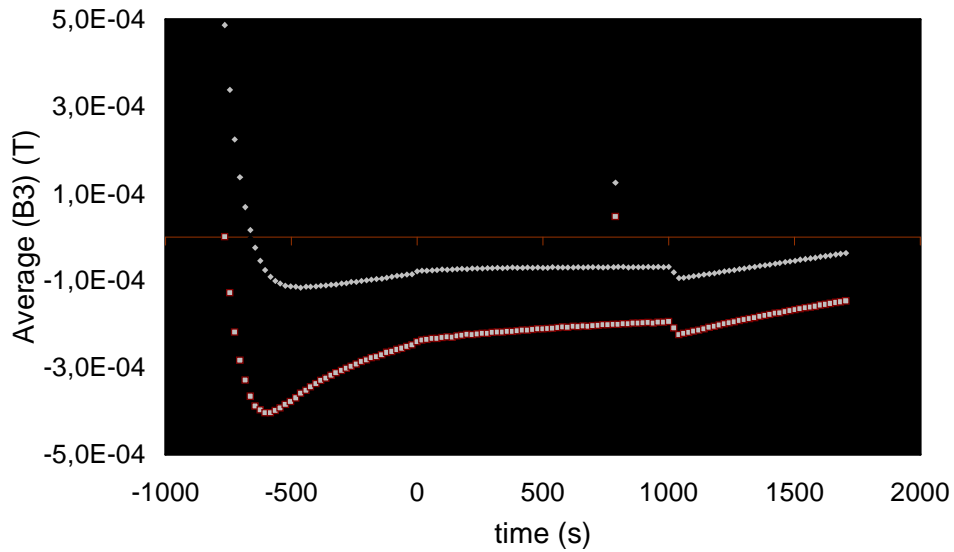


Fig 5.30 Variation in time of the average value of the normal sextupole pattern after pre-cycles with different flat top times. The time reference is set to zero at the beginning of the injection phase.

It is interesting to note that the variation of the average value of the sextupole with very short flat top times is not negligible.

This variation is not due to the relation of the current distribution with the superconductor magnetization because in this case the amplitude of the pattern is negligible. The variation may be due to the thermally activated “flux creep” occurring in the superconducting material of the cable, as already observed in [34, 68].

Phase of the modulation of the field harmonics

The variation of the initial phase of the field modulation during the operation cycle measurements is always very small. The phase variation during the injection phase of the longest measurement performed is reported in Fig. 5.31 in the bottom position of the magnet. The average translation velocity in this case is of about $9 \cdot 10^{-8}$ m/s, equivalent to 0.3 mm/h. The longitudinal displacement of the pattern is negligible.

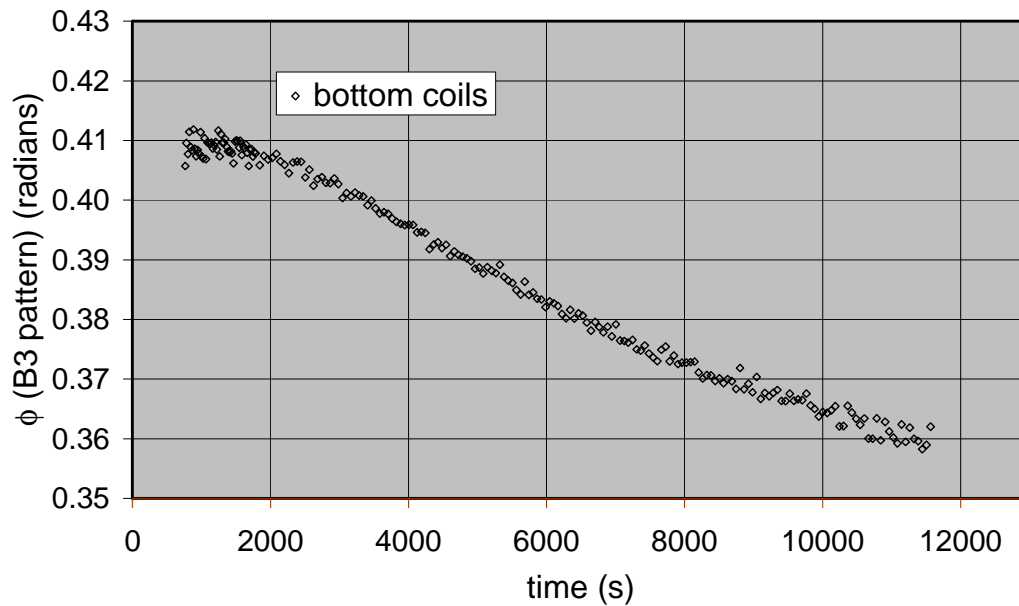


Fig 5.31 Initial phase of the sextupole pattern during the injection of the longest measurement performed (pre-cycle with $T_{FT} = 30$ min and $I_{FT} = 11750$ A).

Comparison between average and amplitude variations

The amplitude variation and the field drift exhibit a similar dependence on the pre-cycle flat top time at both positions of the magnet.

The variation of the average value is plotted in Fig. 5.32 as a function of the amplitude variation for every real operation cycle measurement.

The apparent correlation between the variation of the amplitude and the variation of the average in correspondence of the middle part of the magnet indicates that the two phenomena are indeed dependent on each other, as hypothesized in [28].

In the case of real operation cycles measurements we can exclude that the average value variation is only due to the effect of misalignment between the coil group and the sinusoidal oscillation explained in Section. 5.2.8 for the step response measurements. If that were the case, due to the linear dependence shown in eq. 5.5, we would expect the same kind of temporal evolution for the amplitude of the periodic pattern and the average value of the harmonic considered. Instead,

we note in Fig. 5.30 the characteristic snap-back of the average value, which has not any corresponding feature in the amplitude variation in the same measurements (see Fig. 5.27).

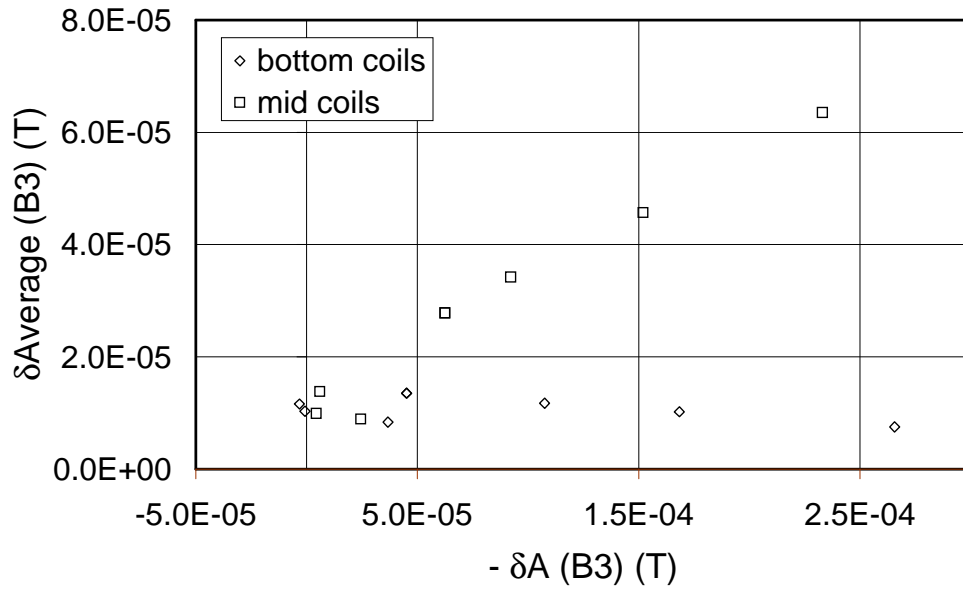


Fig. 5.32 Average delta variation versus amplitude variation (changed of sign) for all operation cycles measurements.